Leaky Waves for Near and Far Field Antenna Beam Shaping

Darwin Blanco
Department of Signal Theory
Universidad Carlos III de Madrid

Advisors
Eva Rajo Iglesias
Nuria Llombart Juan

This dissertation is submitted for the degree of
Doctor of Philosophy (PhD), Multimedia and Communications

Madrid, 2014

A todo lo que ha permanecido detenido mientras se cumplía este sueño.

Foreword

This thesis has been done in collaboration between the Universidad Carlos III de Madrid (UC3M) and the Universidad Complutense de Madrid (UCM) both in Madrid, Spain. The work was guided by Eva Rajo Iglesias from UC3M and Nuria Llombart Juan from the UCM (currently at the Technical University of Delft, The Netherlands). All the thesis costs have been supported by two grants (UC3M) and two projects (UCM). The initial period of the thesis has been funded by the research project: "Estudio de mecanismos avanzados para el acoplamiento de la radiación del infrarrojo lejano a detectores, superconductores para el instrumento", from the Spanish Ministry of Science and Innovation (SAFARI/SPICA, 2011-2012). Afterwards the financial support for the final period of the thesis came mainly from the project: "Diseño de Agrupaciones de Antenas con Filtros Angulares Realizados Mediante Estructuras Periódicas Selectivas en Frecuencia", (EADS CASA ESPACIO (ECE), 2012-2013). Both projects were supervised by Nuria Llombart.

Abstract

The main purpose of this thesis is to present innovative beam shaping antennas, based on leaky wave antennas LWAs, which can meet fundamental requirements like: low cost, low profile and high gain. Important fields of application switch on from near-field (holographic concept) to far-field (low and high satellite applications). For the near-field application, the objective has been the use of periodic LWAs to synthesize a near-field pattern focusing at a specific point and with also a predetermined polarization. The impact of the circular or radial polarization on the shape of the focal region in these periodic LWAs has been investigated. Also the ability of these antennas to do frequency steering of the focus is studied for all the designs.

For the far-field application, we consider two main scenarios: in the first one, we study solutions for Geostationary Satellite (GEO) where thinned arrays are required to scanning at a few degrees. In the second one, we point to LEO satellites, where dense arrays are more suitable for large scanning angles. In these applications, uniform LWAs are more appropriate, since they allow the possibility for overlapping areas between the different array elements.

All results are carefully corroborated with commercial software and home-made code as well as with the measurement of the fabricated prototypes.

Contents

Contents ix

List of Figures xiii

List of Tables xxiii

I Introduction 1

II Holographic Focused LWAs for Near-Field Imaging 11

II.1 Introduction 13

II.2 Modulating Cylindrical Leaky Waves 17
- II.2.1 Design of Radially-Modulated Slot 22
- II.2.2 Analysis of Focused Fields 27

II.3 Circularly Polarized Slot LWA 29
- II.3.1 Optimized Design 30
- II.3.2 Prototype and Experimental Results 37
- II.3.3 Frequency Steering of the Focus 40

II.4 Radially Polarized Slot LWA 51
- II.4.1 Near-field focusing with radial and transverse polarizations 52
- II.4.2 Prototype and Experimental Results 55

II.5 Concluding Remarks 59

III LW Phased Arrays for Telecommunication Applications 61

III.1 Introduction 63

III.2 On a rigourous comparison between dielectric and MTS based LWAs 67
III.2.1 On the Equivalence between LWAs 70
III.2.2 LWA Designs for Array Applications 78
III.2.3 Experimental Verification 82

III.3 Mutual coupling impact on leaky wave thinned phased arrays 89
III.3.1 Array Element Geometry 89
III.3.2 Mutual Coupling Impact and Compensation 91

III.4 Leaky Wave Thinned Phased Array in PCB Technology 101
III.4.1 Array Element Optimization 101
III.4.2 Phased array performances 106

III.5 Leaky Wave Phased Arrays for Isoflux Applications 115
III.5.1 Isoflux Applications 115
III.5.2 Design of an Isoflux LWA 118
III.5.3 Performance evaluation of isoflux LW phased arrays 128

III.6 Concluding Remarks 135

IV Conclusions and Future Lines 137

Appendix A Holographic Antenna Synthesis 143
A.1 Geometry Synthesis Algorithm 143

Appendix B Green's Function of Planar Stratified Dielectric Media 147
B.1 Spectral Green's Function 147
B.2 Solutions of the equivalent transmission line 149
  B.2.1 N-Dielectric Layers 149
  B.2.2 MTS 151

Appendix C Calculation of the Radiated Far and Near-Fields 155
C.1 Far-Field Calculation 156
C.2 Near Field Calculation 157

References **159**

List of Related Publications **171**

List of Figures

1 (a). A rectangular dielectric rod on which is placed a periodic array of metal strips as a classical example of the periodic LWA and (b). a rectangular waveguide with a continuous slit cut along one of its sides as a classical example of the uniform LWA. 3

II.2.1 Scheme of holographic lens in modulated printed-slot technology. 20
II.2.2 Modulation of LW aperture-field along the radial distance ρ to design a leaky lens with $R = 3\lambda_0$, $R_0 = \lambda_0/4$, $F = 6\lambda_0$, $\eta_{RAD} = 85\%$, $\eta_{TAP} = 75\%$ at $10GHz$. 21
II.2.3 Effect of aperture distribution and radiation efficiency in the tapering of the cylindrical leaky-wave leakage-rate with $\eta_{RAD} = 85\%$. 22
II.2.4 Frequency dispersion of Bloch wave and n=-1 SH in the double slit grounded dielectric slab. 23
II.2.5 Two-dimensional dispersion chart at $10GHz$ showing constant θ_{RAD} and constant α/k_0 contour curves as the slots width W and period P are simultaneously varied (the rest of dimensions are summarized in Figure II.2.4). 25
II.2.6 Radial modulation and sampling of printed-slots width W and period P as a function of azimuthal coordinate ϕ to design the aperture of Figure II.2.2. . . 25

II.3.1 Amplitude of aperture fields for the tapered cylindrical LW antenna designed in Figure II.2.2. (a). Continuous aperture fields (b). Discrete aperture fields over slots. The intensity of the field is linearly normalized and λ_0=30mm at 10GHz. 30
II.3.2 Theoretical near-fields in the zy plane ($\phi = 90deg$). The intensity of the field is linearly normalized and $\lambda_0 = 30mm$. 31
II.3.3 Theoretical (a). amplitude and (b). phase near-field patterns along the axial cut (z-axis) of the designed holographic lens. 32

II.3.4 Theoretical near-fields in the *xy* plane at $z = I = 4.5\lambda_0$. The intensity of the field is in decibels and $\lambda_0 = 30mm$. 33

II.3.5 Theoretical near-field patterns along the principal transverse cuts for $z = I = 4.5\lambda_0$. Amplitude in (a). *x*-axis (b). *y*-axis, (c). phase in *x*-axis. 34

II.3.6 Validation of axial near-field focusing patterns comparing CST simulations of the designed holographic lens and tapered LW aperture theory. 36

II.3.7 Validation of transverse near-field focusing patterns comparing CST simulations of the designed holographic lens and tapered LW aperture theory. . . . 36

II.3.8 Photograph of fabricated holographic leaky-wave lens (LWL) in printed-slot technology. 37

II.3.9 (a). Feeding coaxial probe, illustrating the main dimensions and (b). comparison between simulated and experimental input matching of the fabricated holographic leaky-wave lens. 38

II.3.10 Designed experimental setup. 39

II.3.11 Comparison between simulated and measured near-field focusing patterns of the fabricated holographic leaky-wave lens at 10GHz (a). axial cut along z-axis (x=y=0) (b). transverse cut along x-axis (z=139mm). 39

II.3.12 Dispersion with frequency of the tapered cylindrical leaky wave along the radial distance of the designed holographic lens. (a). pointing angle and (b). leakage rate as a function of the frequency. 42

II.3.13 Scheme illustrating the dispersion of the focal region with frequency. 42

II.3.14 Dispersion with frequency of the aperture fields along the radial distance for $\phi = 0deg$, in the designed holographic lens. 43

II.3.15 Theoretical near-field intensity at zy-plane as a function of frequency. 44

II.3.16 Theoretical near-field intensity at xy-plane as a function of frequency and for the corresponding focal heights. 45

II.3.17 Intensity of the theoretical near-field along *x*-axis for the corresponding focal heights as a function of the frequency. (a). amplitude and (b). phase patterns. 46

II.3.18 Frequency dispersion of E_x field intensity at the axial cut. 47

II.3.19 Frequency dispersion of field intensity along *x*-axis for *z*=139mm. 47

II.3.20 (a). Variation of focal length, depth and width with frequency and (b). variation of focusing and radiation efficiencies with frequency. 49

II.4.1 Near-field focused aperture with (a). transverse and (b). radial polarization. . 52

II.4.2 Near-field focused aperture with (a). radial polarization and (b). transverse polarization: half power beamwidth HPBW for the focal depth Δz and relative focal width $\Delta\rho/\Delta z$ as a function of Fresnel number N when $2 <= N <= 10$ for different focal heights Zm. 54

II.4.3 Theoretical 3D focused spot for (a). radially and (b). transversally-polarized lens. 55

II.4.4 Radiated fields as a function of the ratio Zm/N for both (a). radial and (b). transverse polarization. 56

II.4.5 Fabricated annular-slot holographic antenna with radial polarization. 56

II.4.6 Reflection coefficient. 57

II.4.7 Designed annular slot position and widths. 57

II.4.8 (a). Experimental validation of near-field focusing of radially polarized fields at 10GHz for N=4. (b). measured and theoretical transverse distribution of near-field at 10GHz. 57

III.2.1 LW waveguide antenna using (a). a dielectric superstrate with permittivity ε_r, (b). an inductive strip grid based MTS and (c). a capacitive slot grid based MTS. The periodicity of the MTS is d, whereas w indicates the strip width. We refer to capacitive MTS when the strips are aligned to the H-plane and to inductive MTS when the strips are aligned to the E-plane. 68

III.2.2 Equivalent transmission line for (a). dielectric super-layer and (b). equivalent MTS. 71

III.2.3 TE_1 mode solution of the dispersion equation with $\varepsilon_r = 4$ (continuous lines) and $\varepsilon_r = 10$ (dashed lines) for three equivalent cases: dielectric superstrate (blue), inductive strip grid based MTS (red) and capacitive slot grid based MTS (black). 73

III.2.4 TM_1 mode solution of the dispersion equation with $\varepsilon_r = 4$ (continuous lines) and $\varepsilon_r = 10$ (dashed lines) for three equivalent cases: dielectric superstrate (blue), inductive strip grid based MTS (red) and capacitive slot grid based MTS (black). 73

III.2.5 TM_0 mode of the numerical (continuous lines) and approximate (dashed lines) solution of the dispersion equation with $\varepsilon_r = 4$ for three equivalent cases: dielectric superstrate (blue), inductive strip grid based MTS (red) and capacitive slot grid based MTS (black). 76

III.2.6 TM$_0$ mode of the numerical (continuous lines) and approximate (dashed lines) solution of the dispersion equation with ε_r =10 for three equivalent cases: dielectric superstrate (blue), inductive strip grid based MTS (red) and capacitive slot grid based MTS (black). 77

III.2.7 E-plane Comparison of theoretical radiation patterns for the equivalent structures described in Figure III.2.1 at $f = f_0$. 77

III.2.8 H-plane Comparison of theoretical radiation patterns for the equivalent structures described in Figure III.2.1 at $f = f_0$. 78

III.2.9 Directivity as a function of the frequency for the equivalent LWA starting from ε_r=10. The dielectric LWA bandwidth is BW=3.8%, whilst the bandwidth for the inductive and capacitive-based LWAs is 3.7% and 5.7%, respectively. 78

III.2.10 Description of the basic antenna and iris used to feed the cavity. The parameters of the slots in the iris are $a = 14.6mm$, $w = 0.5mm$, $\rho_{TM_0} = 10.79mm$ and $\alpha = 79deg$. The squared waveguide has a length of $wg = 0.7\lambda_0$ by side. 81

III.2.11 Directivity as a function of the frequency for the equivalent structures described in Figure III.2.1. The waveguide dimension is $w_g = 0.7\lambda_0$ and the width of the iris has been fixed to w=0.51mm whilst the diameter of the iris has been fixed to $\lambda_{TM_0}/2$ of each case (10.73mm, 10.43mm and 10.66mm for dielectric, inductive strip grid and capacitive slot grid based MTS respectively). The 1dB directivity BW is 3.86% for dielectric, 3.51% for the inductive and 3.3% for the capacitive case respectively. 82

III.2.12 E-plane Comparison of CST simulated radiation patterns for the equivalent structures described in Figure III.2.11 at the frequency with highest directivity. 82

III.2.13 H-plane Comparison of CST simulated radiation patterns for the equivalent structures described in Figure III.2.11 at the frequency with highest directivity. 83

III.2.14 Description of the iris and transition used to feed the cavity. The parameters of the feeder are for the transition $x = 6.48mm$, $y = 12.95mm$, $p = 45.22mm$, $h_p = 0.5mm$ and the slots in the iris $a = 14.6mm$, $w = 0.5mm$, $\rho_{TM_0} = 10.79mm$, $\alpha = 79deg$. The same basic antenna will be used in both dielectric and inductive strip grid based MTS. 84

III.2.15 Practical realization of the inductive strip grid based MTS LWA. 84

III.2.16 Simulated radiation pattern for the two prototypes. The directivity of the dielectric super-layer and inductive strip grid based MTS antenna are 17.2dB and 18.8dB respectively at *f*=14.25GHz. Both antennas are fed with the iris shown in Figure III.2.14. 85

III.2.17 Simulated directivity in dB for the dielectric and equivalent inductive antennas. The BW is respectively 4.23% and 3.45% for the dielectric and inductive strip grid based MTS prototype with iris and transition. 85

III.2.18 Prototype photos for (a). MTS (b). waveguide transition (c). measurement set-up 86

III.2.19 Measured gain for the dielectric and equivalent inductive LWAs. The BW is 2.52% for both prototypes. 87

III.2.20 Measured radiation pattern for the two prototypes. The measured gain of the dielectric super-layer and inductive strip grid based MTS antennas are 16.6dB and 19.6dB respectively at *f*=13.9GHz. Both antennas are fed with the iris shown in Figure III.2.14. 87

III.2.21 Measured S_{11} for the dielectric and equivalent inductive antennas. Simulated results are also included for comparison purposes. The BW of the reflection coefficients S_{11} are 3.62% and 3.90% for the measured dielectric and MTS prototypes respectively. 88

III.3.1 Antenna geometry. Upper: 5x5 array with dielectric superlayer at top, h_1 is the cavity height and h_2 is the dielectric thickness. h_p is the ground and iris thickness. Each element is composed of a squared waveguide feed and a double slot iris. Lower center: structure of waveguides used to match the active impedance. Center right: parameters of the iris for each element. . . . 90

III.3.2 Reflection coefficient S_{11} and mutual coupling S_{21} at $1.5\lambda_0$ for different dielectric superlayers. The iris dimensions are $w_s = 0.028\lambda_0, 0.024\lambda_0, 0.024\lambda_0$ and $\rho = 0.526\lambda_0, 0.516\lambda_0, 0.5\lambda_0$ for each dielectric constant respectively. . 91

III.3.3 Comparison between the 5x5 embedded and the element pattern in the E-Plane for each dielectric superlayer (ε_r=4,8,12) at central frequency. 92

III.3.4 Active reflection coefficient for all elements of the 11x11 array. The active reflection coefficient simulated with the developed in house code for the active impedance is also shown in a black-solid line (upper figures). 95

III.3.5 Embedded and the 11x11 array radiation patterns for the dielectric superlayer antenna with ε_r=4, 8 and 12 at several scanning angles. 96

III.3.6 Farfield components in a polar coordinate system of the 11x11 phased arrays with ε_r=4,8,12. 97
III.3.7 Horn array geometry. Center: 11x11 array of conical horns spaced $1.5\lambda_0$. Upper detail: dimensions in order to maximize the directivity, A=$1.4\lambda_0$, a=$0.86\lambda_0$, R=$0.653\lambda_0$, $\theta = tan^{-1}(A/R)$. 97
III.3.8 (a). H-plane and (b). E-plane 11x11 array radiation patterns for the horn antenna array at scan $\phi = 0deg$ and $\theta = 8.6deg$. 98
III.3.9 Dependence on frequency of the main parameters of the leaky-wave array antenna for ε_r = 4, 8, 12 and conical horn cases at broadside, at one scan angle of $8.6deg$ in the H-plane and E-plane respectively. 99

III.4.1 (a). Leaky wave thinned phased array: h_{MTS} is the cavity height, w_{MTS} and d_{MTS} are the MTS periodicity and strip width respectively. The array has a periodicity of $2\lambda_0$. (b). thinned phased array composed by 2x2 sub-arrays. The array element spacing is λ_0, but the phase shifting is applied at the subarray level (i.e. corresponding to a periodicity of $2\lambda_0$). 102
III.4.2 Antenna geometry of the single element: top and side views of the printed antenna microstrip element: slot (l_s, w_s) in a via-hole based circular cavity (ρ_s) coupled to a dipole (l_p, w_p) and excited via microstrip (l_m, w_m). (a). top view and (b). side view. 103
III.4.3 Simulated radiation patterns of the array element designed in PCB. 103
III.4.4 Reflection coefficient S_{11} and directivity for MTS leaky wave element (solid lines) compared to the basic printed antenna element of the benchmark reference (dashed lines). The reflection coefficient is shown in the left axis whilst the directivity is represented in the right one. 104
III.4.5 2D representation of the benchmark array element radiation pattern: (a). co-polarized and (b). cross-polarized fields in the upper medium, (c). co-polarized and (d). cross-polarized fields in the lower medium. 105
III.4.6 2D representation of the MTS array element radiation pattern: (a). co-polarized and (b). cross-polarized fields in the upper medium (c). co-polarized and (d). cross-polarized fields in the lower medium. 106
III.4.7 H-Plane radiation pattern of the benchmark and MTS based array elements at the central frequencies (including embedded pattern of a 5x5 array for the MTS case). 106
III.4.8 Active reflection coefficient calculated with CST for all of the 49 elements of the MTS and benchmark phased arrays at different scanning angles. . . . 108

III.4.9 Farfield in the upper (a)-(b) and lower (c)-(d) medium in a polar coordinate system of the 7x7 MTS (a)-(c) and benchmark (b)-(d) arrays radiating at broadside. 109

III.4.10 Farfield in the upper (a)-(b) and lower (c)-(d) medium in a polar coordinate system of the 7x7 MTS (a)-(c) and benchmark (b)-(d) arrays radiating at the scanning angle $\theta = 8.6deg$ in E-plane. 109

III.4.11 Farfield in the upper (a)-(b) and lower (c)-(d) medium in a polar coordinate system of the 7x7 MTS (a)-(c) and benchmark (b)-(d) arrays radiating at the scanning angle $\theta = 8.6deg$ in H-plane. 110

III.4.12 H-plane radiation pattern for the 7x7 phased array (MTS case) at broadside (dark solid line) and at scanning angle of $\theta = 8.6deg$ (gray solid line) including also the 5x5 embedded pattern (dark dashed line). 110

III.4.13 H-plane radiation pattern for the 7x7 benchmark array at broadside (dark solid line) and at scanning angle of $\theta = 8.6deg$ (gray solid line) including also the element pattern (dark dashed line). 111

III.4.14 Frequency analysis for the main parameters: directivity (D), gain (G), grating lobe (GL) and front to back ratio (FB). D and G must be read on in the left side axis whilst GL and FB are represented on the right axis. 112

III.4.15 Beam efficiency as a function of the frequency (at broadside and at the maximum scanning angle of θ=8.6deg in the H and E-planes). In dark-lines is represented the MTS array design and in gray-lines the reference benchmark array antenna. The solid-line represents the beam efficiency at broadside whilst square-line is the scan in the H-plane and the circle-line is the scan in the E-plane. 113

III.4.16 Front to Back efficiency as a function of the frequency (at broadside and at the maximum scanning angle of θ=8.6deg in the H and E-planes). In dark-lines is represented the MTS array design and in gray-lines the reference benchmark array antenna. The solid-line represents the front to back efficiency at broadside whilst square-line is the scan in the H-plane and the circle-line is the scan in the E-plane. 114

III.5.1 Geometrical description of a LEO satellite communication scenario. 117

III.5.2 Geometry of the super-layer design. 118

III.5.3 Objective function for a satellite ranging from 160km to 320km. The red line shows the mask. θ_e represents the maximum scanning angle. 120

III.5.4 $Isoflux_1$ design shows a flattered shape at broadside, a $9dB$ of compensating losses at $50deg$, a very good roll-off at angles greater than $50deg$ and symmetric H and E-planes. 121

III.5.5 TM_0 modes of the dispersion equation as a function of the normalized leaky wave wavevector. 121

III.5.6 Dispersion equation values of the $isoflux_1$ design. A notable difference can be appreciated between the TE and TM attenuation constant. 122

III.5.7 $Isoflux_2$ shows a flattered shape at broadside, a $5dB$ of compensating losses at $50deg$, good roll-off at angles greater than $50deg$ and symmetric H and E-planes. 123

III.5.8 TM_0 modes of the dispersion equation as a function of the normalized leaky wave wavevector. 123

III.5.9 Dispersion equation values of the $isoflux_2$ design. A notable difference can be appreciated between the TE and TM attenuation constant. 124

III.5.10 Parameters of the single antenna element: f_0 =8.2GHz. The diameter of the aperture is fixed to $0.6\lambda_0$ and it is limited by vias. The diameter distance between the slots is set to $d = 2\rho = \lambda_{TM_0}/2$ for each design. 125

III.5.11 Aperture fields inside the first cavity at $z = h_1/2$ for the $isoflux_1$ design with absorber. 125

III.5.12 Radiated fields of the dielectric iris structure with absorber for $isoflux_1$ design. The distance between slots is $\frac{\lambda_{TM_0}}{2} = 0.83\lambda_0$ at $f_0 = 8.2GHz$. 126

III.5.13 Radiated fields in the main planes for $isoflux_1$ theoretical versus simulated in CST. 126

III.5.14 Aperture fields inside the first cavity $z = h1/2$ for the $isoflux_1$ design without absorber. 126

III.5.15 Reflection coefficient and radiated fields in the main planes for the $isoflux_1$ design without absorber. 127

III.5.16 Frequency behavior of the radiated fields in the main (a). H- and (b). E-planes for the $isoflux_1$ design without absorber. Here we show a band of 1GHz (7.7GHz-8.7GHz). 127

III.5.17 Reflection coefficient and radiated field in the main planes for the $isoflux_2$ design without absorber. 128

III.5.18 Embedded pattern in the main E and H-planes for the $isoflux_1$ and $isoflux_2$ designs without absorber for a 5x5 phased array. 129

III.5.19 Main parameters of the basic reference antenna in a periodic scenario to calculate the active impedance. (a). periodic cell. (b). triangular lattice. (c). lateral view of layered structure. The length and the width of the dipole is $l_d = 10.56mm$ and $w_d = 0.68mm$ and for the slot $l_s = 13.07mm$ and $w_d = 0.75mm$ respectively. The permitivity of the susbtrates for the basic antenna (without taking into account the stratified media) is $\varepsilon_{rsubs} = 1.5$. The height of the susbtrate layer between the dipole and slot is $h_m = 3mm$ whilst the height of the substrate between the slot and the ground plane is $h_s = 1mm$. In the middle of the this last layer there is a stripline feeding the slot. 130
III.5.20 Scan blindness for $isoflux_1$ design. 131
III.5.21 Grating lobe for $isoflux_1$ design. 131
III.5.22 Scan blindness for $isoflux_2$ design. 131
III.5.23 Grating lobe for $isoflux_2$ design. 131
III.5.24 Mutual coupling level for an 11x11 phased array and active reflection coefficients at broadside. 132
III.5.25 Active reflection coefficients for an 11x11 phased array, in four different scanning angles at the two main planes. 133
III.5.26 Embedded pattern and array radiation pattern at the different scanning angles for an 11x11 array. 134

A.1 Spiral generated as a function of ρ and ϕ 145

B.1 An electric source placed at the dielectric-air interface and a magnetic source at the ground plane of a grounded slab. 148
B.2 Equivalent transmission line to be solved for the case of a single stratification of height h above a ground plane: magnetic source. 149
B.3 Equivalent transmission line to be solved for the case of a single stratification of height h above a ground plane: electric source. 149
B.4 (a). Geometry and (b). equivalent transmission line model of the dielectric stratified media. 150
B.5 Equivalent transmission line model for a practical MTS stratified media. . . 152

C.1 Superficial current density over a planar antenna. To calculate the far-fields, we consider $\vec{R} \gg \vec{r}'$ 156
C.2 Radiated near-field by a superficial electric current density. 158

List of Tables

III.2.1 Comparison of the propagation constants obtained for the equivalent MTSs and $\varepsilon_r = 10$ dielectric LWAs at central frequency. 74

III.2.2 Directivities for the equivalent MTS and dielectric geometries with ε_r=10 at central frequency and maximum value in the band. 81

III.2.3 Original and optimized inductive strip grid based MTS design. 83

III.4.1 Specifications for the application scenario. 102

III.4.2 Main parameters of the 7x7 phased array compared to the reference benchmark for the three scanning angles at central frequency. 111

III.5.1 Summary of the desired requirements. 116

III.5.2 Main parameters of the $isoflux_1$ design. 120

III.5.3 Leaky wave wavevector at central frequency for $isoflux_1$ design. 121

III.5.4 Main parameters of the $isoflux_2$ design. 122

III.5.5 Leaky wave wavevector at central frequency for the $isoflux_2$ design. 123

Part I

Introduction

IN recent times the leaky-wave antennas (LWAs) have won significant attention by the scientific community after that Hansen reported the slitted waveguide in 1940 [1]. In that first work, it was shown that because of the periodic loading of a waveguide with the slits, the waveguide mode is characterized by a complex propagation constant $k_z = \beta - j\alpha$ with $|\beta| \leq k_0$ (k_0 is the free space propagation constant) . This waveguide mode travels in the guiding structure faster than the speed of the light (fast waves) and at the same time it leaks energy into free space and therefore it has an attenuation constant α. In a lossless case, this energy is totally radiated by the structure (if the length of the aperture is large enough) and then the LW couples the guided power into free space [2].

LWAs can be classified in mainly two types depending on the physical principle for radiation: periodic or uniform [3].

Periodic LWAs support a slow wave with $|\beta| > k_0$ and the structure is periodically modulated in the transverse direction (see Figure 1.a). This modulation creates a guided wave composed of infinite harmonics [2] of Floquet modes. For the n-th Floquet mode, the wavenumber is given by $k_{zn} = k_{z0} + 2\pi n/p$, where p is the period and $k_{z0} = \beta - j\alpha$ is the wavenumber of the fundamental Floquet wave. The n=0 mode is a slow wave (surface wave) but with a proper design we can obtain a fast wave (LW), typically using n=-1 and thus a radiating wave. This type of LWA will be exploited in this thesis to achieve near field focusing.

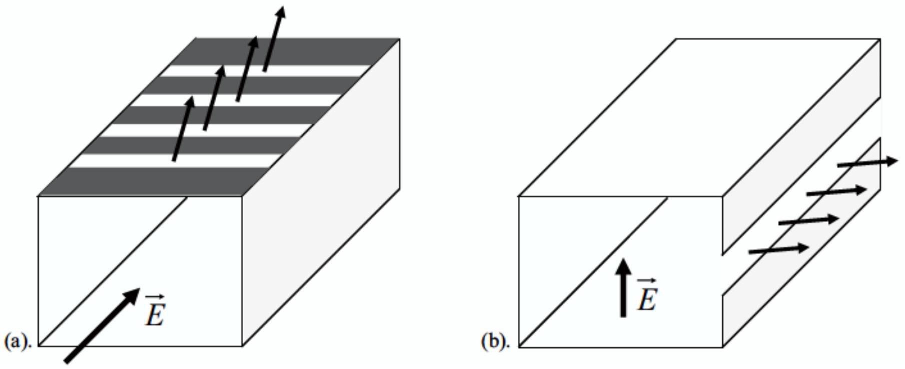

Fig. 1 (a). A rectangular dielectric rod on which is placed a periodic array of metal strips as a classical example of the periodic LWA and (b). a rectangular waveguide with a continuous slit cut along one of its sides as a classical example of the uniform LWA.

Uniform LWAs use a different mechanism to leak the energy in the entire aperture of the antenna since there is not a significant periodicity in the transverse direction as in [1] (see Figure 1.b). For the case of the uniform LWA, first discovered by [4], there is a certain longitudinal stratification that supports a radiative fast wave. This stratification can be seen as a partially reflecting structure (PRS) as introduced by Trentini in 1956 [5]. Then this PRS must be located on top of a ground plane to create a LWA and enhance the directivity of small antennas [5–15]. Although some PRSs are built by periodic structures (i.e. metasurfaces), their period is small enough ($\leq \lambda_0/4$) to be considered as uniform LWA (they do not use the Floquet-modes to radiate the energy).

The shape of the radiated fields is primarily determined by the used stratification and only to a minor degree by the type of source. The physical phenomenon exploited in this kind of antennas, to achieve high directivity from a point source, is the excitation of one or more nearly degenerated TE/TM leaky wave modes. These modes propagate in the resonant region by means of subcritical multiple reflections, while partially leaking energy in free space. The amount of energy radiated at each reflection is related to the LW attenuation constant and can be controlled by the PRS transmission coefficient. The maximum directivity at broadside is achieved at the resonant condition [6]. Under this condition, the couple of TE/TM leaky wave modes can propagate with the same phase velocity, creating a nearly uniform phase distribution in the aperture. It has been seen that the generated aperture field is also very well polarized, due to a compensation effect between the TE and TM modal tangential field components [16]. Other important characteristic in uniform LWAs is that for a detuned structure at frequency above the resonant frequency, the far-field radiation pattern exhibits conical shape which eventually degenerates in a pencil beam at the frequency where the real part and imaginary part of the complex leaky wave wavenumber are equal. These properties of the uniform LWAs will be used in this thesis to design beam shaping phased array antennas.

Spectral Analysis of LWA

The transverse propagating modes (surface waves or leaky waves) associated to a certain geometry are associated to the pole singularities of the associated spectral Green's function. Then the spectral Green's function (SGF) $\underline{G}^{em}(k_y,k_y,z,z') = \frac{N(k_\rho)}{D(k_\rho)}$ has to be derived, analytically or numerically, in order to extract the propagation constant of these propagating modes. The pole singularities, k_ρ, are directly associated to the transverse propagation constant of these modes. The SGF depends on the properties of the stratified medium and it has two main types of singularities, branch points, related to radiation towards an open medium and poles associated to the modes propagating inside the structure [17]. The spectral location of the pole singularities defines the type of propagating modes. For free space open structures, poles with propagation constants larger than k_0 are associated to trapped surface waves (slow waves). Instead, poles located in the bottom Riemann sheet having a complex propagation constant with $Re(k_\rho) < k_0$ and $Im(k_\rho) > 0$ are associated to radiating leaky waves (fast waves).

When the LWA is a uniform Fabry-Perot like structure, the leaky wave modes are directly supported by the stratification and not due to a periodicity. For this case, the SGF can be easily calculated using a transmission line formalism [17]. Finding the zeros of the denominator of this SGF is typically referred as solving the dispersion equation of the LWA. The methodology to solve the SGF for an n-layered structure is presented in Appendix B.

In the case of periodic LWA, a SGF that includes the effect of the periodic loading is necessary to find the dispersion properties of the leaky modes. This SGF can be obtained by integration of the responses of the periodic structure to both types of plane waves, homogeneous and inhomogeneous, emanating from a non periodic and elementary source, as it is detailed in [18]. The constitutive problem is to find the actual currents $j(x,y)$ or $m(x,y)$ for the dipole or slot model respectively. These can be derived by imposing an integral equation (IE) and solving this equation with a Method of Moments (MoM) [19]. The MoM solves the IE by segmentation of the electric or magnetic currents using small domain basis functions. In order to reduce the complexity of the periodic LWA problem, the MoM uses the periodic boundary conditions, reducing the analysis to a single unit cell [18]. Periodic LWAs can also be used to locally modulate the LW vector and will be used in this dissertation to create near-field LWA.

State of the Art

Because of their low profile, low cost, easiness and compactness of fabrication and the improvement in the gain with respect to the elementary radiator, there is an increasing attention towards LWAs.

Uniform LWAs have been widely used to obtain directive beams [20, 21], these reported works all have in common that they improve the directivity at broadside of small and low directive antennas considering the resonant condition derived in [6]. This type of antennas are typically referred as Leaky Wave Antennas (LWAs) [6–9], Electromagnetic Band-Gap (EBG) antennas [11], Fabry-Perot Antennas (FPA) [12] and even resonant cavity antennas [15]. Some publications have also reported the high gain enhancement of uniform LWA using periodic partially reflective screens over a ground plane [22], using dielectric superstrate layers [23]. Recently, uniform LWAs have gained interest for future Ka-band telecommunication satellites due to their potential to create overlapping radiating areas in focal plane arrays with a single feed per beam [24, 25]. Telecommunication space industry is currently interested in developing future thinned arrays with limited scanning ranges for the Ku-band. Besides other possible approaches based on sub-arrays, there is the interest to investigate the potential of LWAs for this application, since they would lead to directive array elements even if the array periodicity is large [26]. In [26], it is shown that the effective area of a four element array is equivalent to a single radiator under PRS. In that work, a 2x2 phased array with inter-element spacing of $2\lambda_0$ is manufactured. They verify experimentally that the bandwidth (BW) is inversely proportional to the gain for several multilayer designs. On the other hand, in [27] an interesting study of the impact of mutual coupling between neighboring radiators in a focal plane array is presented. There it is shown that the directivity of the embedded element pattern is reduced by a high level of mutual coupling.

On the other hand, periodic LWAs are advisable to do beam steering because they modify the phase by changing the frequency thus exhibiting frequency controllable radiation. This steerable capability is described in [28, 29] together with its enormous interest for many applications as sensing. There has been also interest in designing LWAs for near-field beam-shaping. In the near-field the LWAs can be interpreted as holographic antennas [30, 31] with importance in biomedical sensors, concealed explosive detection, radar tracking, etc. Due to the tapering of the LW vector over the aperture of the antenna to focus the radiated power in the near-field, the local periodic LWA can be seen as a quasi-periodic LWA. Archimedean spirals and concentric rings are the most common geometries for near-field focusing with quasi-periodic LWAs as seen for the radial line slot antennas (RLSA) introduced by [32].

In the farfield the applications can make use of directive or isoflux radiation patterns depending on the required application. If we want to cover large angles with a low Earth orbit (LEO) satellite, an isoflux diagram is more suitable whilst for high Earth orbit (HEO) a high directive beam is more convenient. Moreover the feasibility of achieving narrow-beam patterns (obtained without needing a feeding network) and pencil beams (at broadside) or conical beams (at a specified scan angle) increases the range of applications. Currently it is possible to find interesting applications with reconfigurability properties [33–35], dual band operation [36, 37], for imaging [38], satellite [39], base stations (LTE, 4G, mobiles) [40], spatial filters [41], reflector antennas [42, 43] and millimeter wave antennas [44, 45] among others.

Thesis Objetives

The main two goals of the present PhD dissertation is to investigate the potential of LWAs for performing beam forming in the near-field, a recent application of LWAs, as well as the potential of LWAs for improving the performances of thinned phased arrays. This second goal is motivated by requirements of future telecommunication technologies and it has been supervised by EADS/CASA[1], that provided us with the technical requirements of the project.

Overall of the thesis, the LWAs are rigorously analyzed and optimized by investigating their physical insights using a spectral Green's function approach. Moreover all theoretical designs are validated with commercial full-wave simulators as well as with the manufacturing and measurement of prototypes.

For the near-field application, the objective has been the use of periodic LWAs to synthesize a near-field pattern focusing at a specific point and with also a predetermined polarization. To this aim, the TM_0 mode of a parallel plate waveguide (PPW) is modulated in amplitude and in phase in two dimensions in order to maximize the radiation and focusing efficiencies. We investigate how the circular or radial polarization impact on the shape of the focal region in these periodic LWAs. Moreover the frequency response of this kind of antennas is also analyzed in order to study their suitability for doing frequency steering of the focus.

For phased array application, we consider two main scenarios: in the first one we study solutions for Geostationary Satellite (GEO) where thinned arrays are required to operate with spacing of $2\lambda_0$ and a relative frequency bandwidth of 1.7% at Ku-band (14.25-14.5GHz) with a maximum scanning angle of $8.6deg$. In the second one we point to LEO satellites, where dense arrays are more suitable with spacing less than λ_0 at similar frequency specifications but for a maximum scanning angle of $60deg$. In these applications, uniform LWAs are more appropriate, since they allow the possibility for overlapping areas between the different array elements.

In this part of the thesis, we first investigate which partially reflecting surface, (dielectric superstrate or different MTSs) is the most appropriate for these two scenarios. As for array applications, it is important to maximize the directivity of the LWA at the largest possible bandwidth; we also investigate how to keep the mutual coupling levels low in order to reduce their impact on the embedded pattern.

In this PhD dissertation we also perform a rigorous study of frequency behavior of the designed antennas and compare them to classical references.

---

[1] "Diseño de Agrupaciones de Antenas con Filtros Angulares Realizados Mediante Estructuras Periódicas Selectivas en Frecuencia", EADS CASA ESPACIO (ECE), 2012-2013

Organization of the Thesis

To present a consistent description of the different studies carried out in the framework of this thesis, we have organized the current report into two main parts. Part I is dedicated to the use of LWAs as holographic antennas to synthesize the near-field focused patterns. This part is composed by the following chapters.

Chapter II.1. A novel concept of planar printed-circuit microwave lens, based on the transformation of a cylindrical surface wave into a modulated leaky wave, is introduced in this Chapter.

Chapter II.2. Inspired on holographic concepts, the TM_0 cylindrical leaky wave is properly tapered across a two-dimensional surface. This chapter describes the general analysis and synthesis methodology to obtain planar holographic lenses with high radiation and focusing efficiency.

Chapter II.3. Considering first the circular polarization, this Chapter presents a proposed holographic lens that uses a continuous spiral to focus in the near-field with circular polarization. The interesting effect of frequency steering of the focal lenght is also demonstrated in this kind of antennas. This allows the electronical adjustment of the focus position in a region by simply changing the frequency of the input signal.

Chapter II.4. The last Chapter included in this Part I, reports a technique to improve the overall spot symmetry and resolution of these near field focusing antennas based on the use of axially-polarized focused fields. Moreover we investigate the focus symmetry to establish a limit in terms of the Fresnel number N. This interesting feature for axially against transversally-polarized focused fields has been previously studied in optics, whereby selecting a radially polarized input results in a rotationally symmetric focused field as shown in [46].

Part II is dedicated to leaky wave phased array for telecommunication applications and it is divided in the following chapters.

Chapter III.1. An introduction to the phased array applications as well as the necessity of new antenna designs with improved performances is presented in this Chapter. We also show the state of art of this kind of technology.

Chapter III.2. Firstly we start considering the design of the LWAs with different types of super-layers, demonstrating that the inductive strip based MTS has an improved gain with respect to the other super-layers thanks to the intrinsic suppression of the spurious

TM_0 leaky mode.

Chapter III.3. This chapter shows how the mutual coupling impacts on the active impedance and the roll-off of the embedded patterns necessary to achieve the grating lobe angular filtering in this type of arrays.

Chapter III.4. All the theory of these previous Chapters (III.1-III.3) is then used to design a thinned LW phased array in PCB technology for angular filtering using an inductive strip grid based MTS as PRS. A full study of the higher performance for the proposed solution in the frequency band of interest is presented and compared to a classical solution composed of subarrays.

Chapter III.5. This Chapter is targeted to show a preliminary study of how to design LW isoflux patterns. Several designs using dielectric super-layers to obtain the desired radiated isoflux field are investigated.

Part II

Holographic Focused LWAs for Near-Field Imaging

Chapter II.1

Introduction

HOLOGRAPHIC antennas create an objective radiation diagram from a known reference field and a holographic scatterer, the response of the latter being proportional to the interference pattern between the desired objective function and the conjugated input wave [47]. This has been extended from optical frequencies [48] to microwaves [47] by means of holographic surfaces [49, 50]. They are modulated artificial impedance surfaces (also known as high-impedance surfaces [51] or metasurfaces [52, 53]) able to synthesize the requested interference functions for their effective surface reactance (or namely the effective refractive index), by properly engineering its geometrical dimensions. The first artificial impedance surfaces on thin dielectric substrates were made of conductive pins [54, 55] or holes [54, 56], but increased interest is being given nowadays to printed-circuit technology due to easier fabrication and tuning [49]-[53],[57]-[31]. This surface-impedance driven approach to tailor the behavior of fields has been recently designated as “metasurfing” [52, 53], and it can be considered a particularization of Metamaterial Engineering and Transformation Optics [58] volumetric concepts to the scope of guided or surface waves (SW). No matter the used perspective, the aim of all these theories is to control the local wavevector by properly engineering the artificial circuits, so that the SW fields can be flexibly tailored.

The design of holographic antennas can be interpreted as a transformation of the SW propagating in the hosting planar substrate (which acts as reference signal), into a leaky wave (LW) which radiates to free space at a specified scanning angle [49]-[53],[59]-[31]. Sinusoidally modulated reactance surfaces (SMRS) have been used as holographic transformers which generate a LW, as described by Oliner and Hessel in 1959 [60]. However, all the printed holographic antennas reported until date [47],[49]-[53],[59]-[31] are designed to focus the radiated energy in the far field. This is mainly due to the fact that simple SMRS profiles produce uniform (non-tapered) LWs, which present constant pointing angle and thus radiate in the form of a plane wave focused at infinity at a certain angle.

Microwave lenses were first proposed in $1960's$ to focus the electromagnetic energy in the near-field (Fresnel) region [61], and their properties were studied in detail in the $1980's$ [62]-[63]. The first designs were based on dielectric lenses and metallic reflectors, which are externally illuminated by a spatial plane-wave which is focused at the desired focal point due to the three-dimensional shape of the focusing body (normally parabolic or hyperbolic geometries) by virtue of Geometric Optics [64]. Phased arrays of horns [65],[66], patches [67]-[68], and printed dipole antennas [69], have also been proposed in order to focus the electromagnetic fields in the near-field zone. In these cases, the array feeding network is responsible to excite each element of the array with the requested quadratic-phase and amplitude illumination to synthesize the desired focusing pattern. Similarly, an externally-fed printed reflectarray has been recently proposed to focus in the near-field [70]. In any case, printed-circuit array configurations [67]-[70] offer lightweight, compact, low-profile, cheap solutions when compared to bulky three-dimensional shaped bodies used for dielectric and metallic microwave lenses.

One step forward in the design of electrically-large printed-circuit near-field microwave lenses is the elimination of the complicated feeding network associated to phased arrays with multiple radiating elements [67]-[69], and keeping an integrated feeding mechanism (in opposition to reflectarrays which are externally fed [70]). In this sense, leaky-wave antennas (LWAs) offer an integrated and simple mechanism to illuminate large radiating areas by exciting a leaky mode [71]. Ohtera was the first one to propose the use of a curved one-dimensional ($1D$) LWA to obtain focused near-fields [72], and Burghignoli et al. theoretically demonstrated in [73] that a leaky wave propagating along a $1D$ rectilinear structure can be properly modulated (tapered) to focus the radiated fields, avoiding the complicated bending of the radiator. The first practical designs of rectilinear modulated $1D$ leaky-wave lenses (LWL) were presented in [74] using a dielectric waveguide loaded with a tapered slot. In [75], a parallel-plate waveguide loaded with an inductive sheet formed by microstrip lines was controlled with FETs in order to electronically steer the focal region.

Nevertheless, all the aforementioned LWL designs [75]-[72] are limited to $1D$ leaky lines, which are able to focus only in their longitudinal plane, thus providing $2D$ focusing patterns which are sharp in the longitudinal plane and wide in the transverse direction. However, $3D$ focusing patterns are requested in most practical applications for medicine [66], industry [67], and imaging/sensing [76]-[70]. Recently, cylindrical leaky waves have been proposed to generate 3*D* focused Bessel beams [77],[78]. However, those results did not make use of tapered leaky modes because the emphasis was not on near-field focusing efficiency. This first part of the thesis shows in the following chapters, how to design 3D holographic antennas based on LWAs.

Chapter II.2

Modulating Cylindrical Leaky Waves

One of the most difficult steps when using the holographic or metasurfing approach [52, 53] to design focusing antennas, is to find the relation between the modulated surface impedance and the radiated fields. This relation is not direct, but it depends on the involved Green's functions which relate the reference (input) field, the holographic scatterer, and the output fields [31, 50]. One efficient tool to solve this problem is the Oliner-Hessel method [60] which allows to obtain the propagation constant of a SW and associated LW which propagates thorough a sinusoidally modulated reactance surface (SMRS) with a given mean reactance, modulation index, and modulation period [31, 49, 50, 79]. The second difficult step is the implementation of the requested SMRS in a practical technology whose geometry modulation must be finally obtained.

These two difficult steps (relation of holographic impedance with radiated LW fields, and relation of reactance values with modulated geometry), are systematically solved with the synthesis technique applied in this chapter. To this end, we use the desired LW field aperture distribution as starting point and the dispersion which relates the geometry with the complex LW wavenumber. This avoids the need of intermediate surface impedances and the subsequent transformation of impedances into geometry. Also it is important to highlight that this design technique is not limited to sinusoidally modulated holographic surfaces, but it can be applied to arbitrary modulation functions, and thus to synthesize any complex aperture LW field distribution. This is of key importance to successfully synthesize a near-field focused aperture with high focusing efficiency, as demonstrated in this part of the thesis.

Aperture Fields and Cylindrical Leaky Waves

Since it is accepted that the principle of holographic synthesis can be directly related to the existence of LWs [49, 50],[59]-[31], here we propose a direct synthesis of the aperture fields created by a tapered (modulated) leaky mode. It is assumed that this aperture field directly depends on the leaky-mode propagation constant of a periodic array [74]. This is true for a dominant leaky wave which determines the radiation amplitude and phase of the closely-spaced slots [80], as will be demonstrated in next subsection. We start by imposing a desired complex aperture field (at $z=0$ in Figure II.2.1), which does not take into account the reactive fields (since they do not contribute to the visible spectrum), and which is then expressed by amplitude and phase distributions terms, $A(\rho,\phi)$, $\Psi(\rho,\phi)$:

$$E_{RAD}^{APERT}(z=0,\rho,\phi)=A(\rho,\phi)\cdot e^{+j\Psi(\rho,\phi)} \tag{II.2.1}$$

Note that this represents a scalar field. In reality, the field over the aperture has radial direction because of the TEM wave excitation of the slots, which are orthogonal to ρ and much smaller than the wavelength. Therefore no cross-polarized components in the slots currents are expected. At this point, one only needs to synthesize the amplitude and phase distribution of this radial field. In Chapter II.3, the actual vectorial behavior of the field will be taken into account to calculate the circularly polarized near-fields whilst Chapter II.4 shows the design process to radially polarized near-fields. In the case of near-field focused apertures, a rotationally symmetric quadratic phase distribution of the following form [61] is requested to obtain a focal point at a height F from the planar lens interface (see Figure II.2.1):

$$\Psi(\rho)=k_0\sqrt{\rho^2+F^2} \tag{II.2.2}$$

where k_0 is the free-space wavenumber. On the other hand, the amplitude distribution determines the aperture taper efficiency η_{TAP}, which can be computed using standard theory of radiating apertures [61], and it is also considered rotationally symmetric:

$$\eta_{TAP}=\frac{1}{\pi R^2}\frac{|\iint A(\rho,\phi)\cdot\rho d\phi\cdot d\rho|^2}{\iint A^2(\rho,\phi)\cdot\rho d\phi\cdot d\rho}=\frac{2}{R^2}\frac{\left|\int_0^R A(\rho)\cdot\rho d\rho\right|^2}{\int_0^R A^2(\rho)\cdot\rho d\rho} \tag{II.2.3}$$

The aperture distribution will determine the half-power spot width $\Delta\rho$ for a given aperture diameter $D=2R$. Uniform aperture distributions provide maximum aperture efficiency and thus minimum spot width $\Delta\rho$ for a given focal ratio F/D, which is given by $\Delta\rho \approx \lambda_0 F/D$ [61]. Non uniform apertures will increase the focal width from this optimum value. We can thus express the focusing efficiency η_{FOC} as:

$$\eta_{FOC} = \frac{\Delta\rho \min}{\Delta\rho} \approx \frac{\lambda_0}{\Delta\rho}\frac{F}{D} \tag{II.2.4}$$

To synthesize a given complex aperture distribution from a cylindrical LW, the following synthesis expressions can be used to obtain the requested tapering of the LW, phase β and leakage α factors as a function of the radial distance:

$$\beta(\rho) = -\frac{d\Psi(\rho)}{d\rho} = k_0 \sin\theta_{RAD}(\rho) \tag{II.2.5}$$

$$\alpha(\rho) = \frac{1}{2}\frac{\rho\cdot|A(\rho)|^2}{\frac{1}{\eta_{RAD}}\int\limits_{R_0}^{R+R_0}\rho\cdot|A(\rho)|^2 d\rho - \int\limits_{R_0}^{\rho}\rho\cdot|A(\rho)|^2 d\rho} \tag{II.2.6}$$

where η_{RAD} is the radiation efficiency (the ratio between the input power and the total radiated power [71]), and R_0 stands for the radial position of the first radiating section of the 2D leaky lens. As it can be seen in Figure II.2.1 and Figure II.2.2.a, this is a central non-radiative section needed for matching purposes. Note that eq II.2.6 for the tapering of the leakage-rate differs from the standard 1D expression [71, 74] because it takes into account the cylindrical spreading of the TM_0 surface wave [81]. The tapering of the equivalent leaky pointing angle $\theta_{RAD}(\rho)$ (illustrated in Figure II.2.2.a) can be thus easily determined for a given focal length F by introducing eq II.2.2 in eq II.2.5, obtaining:

$$\sin\theta_{RAD}(\rho) = \frac{\beta(\rho)}{k_0} = -\frac{1}{k_0}\frac{d\Psi(\rho)}{d\rho} = -\frac{\rho}{\sqrt{\rho^2+F^2}} \tag{II.2.7}$$

At this point it is necessary to clarify that each slot does not create a leaky wave with a given pointing angle $\theta_{RAD}(\rho)$, as it could be misunderstood from the ray-optics picture in Figure II.2.2.a. Each portion of the double slit radiates a spherical wave that has a specific amplitude and phase given by the tapered leaky wave [82]. We assume that the *total* field radiated by the interference of the *entire* non-uniform array of modulated slots can be expressed as a *single* tapered leaky wave, which exhibits an equivalent far-field pointing angle distribution $\theta_{RAD}(\rho)$ as shown in Figure II.2.2.a. It is therefore the interaction between all adjacent slots which creates this local modulation of the total field. In this sense, the equivalent pointing angle has physical meaning only when a sufficiently large number of slots contribute to radiation and the observation distance from the slot is sufficiently large (so that the spectral representation of the radiated fields by a single modulated leaky-wave is dominant). Since the design of the proposed structure is based on this assumption (dominant leaky-wave fields), this point needs to be checked later. Nevertheless, it must be noticed that similar ray-optics perspectives have been recently used for the design of LW antennas which locally modulate the pointing angle [73, 83, 84], and also to interpret holographic surfaces [49],[59]-[31].

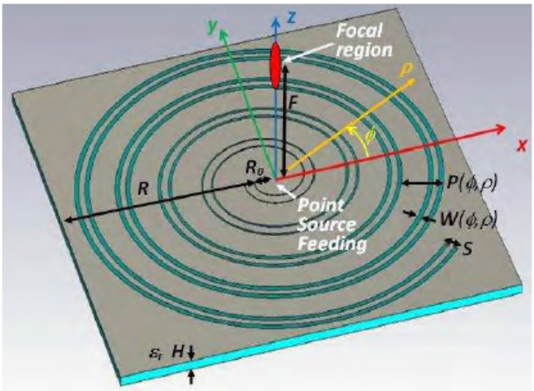

Fig. II.2.1 Scheme of holographic lens in modulated printed-slot technology.

Only radial dependence exists in eq II.2.2-II.2.7 since at this stage it is assumed a perfect rotationally symmetry of the lens layout. As an example, Figure II.2.2.b shows the results for a radially-tapered LW in order to synthesize at 10GHz a focused aperture with radius $R=3\lambda_0$ and focal distance $F=6\lambda_0$. In black dashed lines it is represented the requested complex aperture field $A(\rho)$, $\Psi(\rho)$ of eq II.2.1, which is normalized at the lens origin (unit amplitude and zero phase). In red lines the curves obtained with eq II.2.6-II.2.7 for the radial modulation of the tapered LW pointing angle $\theta_{RAD}(\rho)$ and its normalized leakage rate $\alpha(\rho)/k_0$ are shown. The backward LW must change its equivalent far-field scanning angle from $\theta_{RAD} = 0deg$ at the center to $\theta_{RAD} = -30deg$ at the edges, so that it is obtained the specified quadratic phase distribution $\Psi(\rho)$ for convergence at a height $F=6\lambda_0$ with $R=3\lambda_0$.

Regarding eq II.2.7, low leakage rate conditions ($\alpha << \beta$) have been applied to extend the well-known leakage tapering equation of plane (1D) LWs [71, 85] to the case of cylindrical (2D) tapered LWs [81], following the same procedure used in [86] for uniformly illuminated RLSA. It must be noticed that the center of the lens requires radiation at broadside [87] (see $\theta_{RAD} = 0deg$) for ρ=0 in Figure II.2.2.a. By using R_0 equal to $\lambda_0/4$ a good

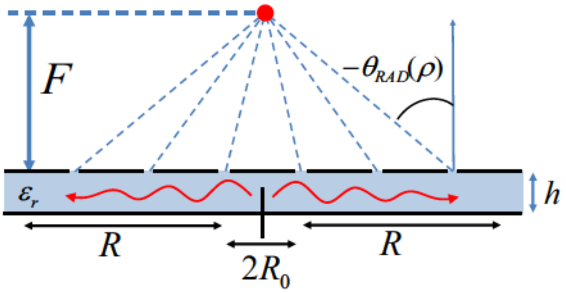

(a) Geometrical parameters of the LWA

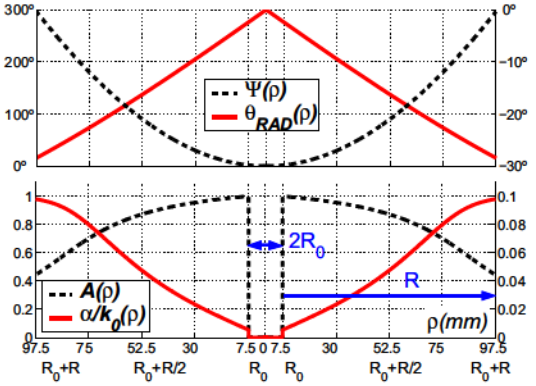

(b) Modulation of LW aperture-field along the radial distance ρ

Fig. II.2.2 Modulation of LW aperture-field along the radial distance ρ to design a leaky lens with $R = 3\lambda_0$, $R_0 = \lambda_0/4$, $F = 6\lambda_0$, $\eta_{RAD} = 85\%$, $\eta_{TAP} = 75\%$ at $10GHz$.

matching of the antenna is achieved. Finally, the radiation efficiency η_{RAD} is normally kept below 90% to avoid divergence of α at the edges (ρ=R+R_0) of the tapered aperture [71]. In the numerical example of Figure II.2.2, we have chosen η_{RAD} =85%, and aperture amplitude function $A(\rho)=cos(\pi\rho/(3.5*R))^2$ which provides quasi-uniform illumination and high tapering efficiency η_{TAP}=75% according to eq II.2.3. Introducing these specifications of R_0, η_{RAD} and $A(\rho)$ in eq II.2.6, it is shown in Figure II.2.2 that the leakage rate must be exponentially increased as the LW moves far from the source, reaching a maximum leakage level α/k_0=0.1 at the lens edge. Increased requested levels of radiation efficiency η_{RAD} would result in too large values of α/k_0 for this lens radius R=$3\lambda_0$, which might be impracticable to synthesize.

Figure II.2.3 illustrates the effect of the amplitude distribution $A(\rho)$ in the tapering of the leakage rate, and the differences between the case of a tapered cylindrical (2D) LW

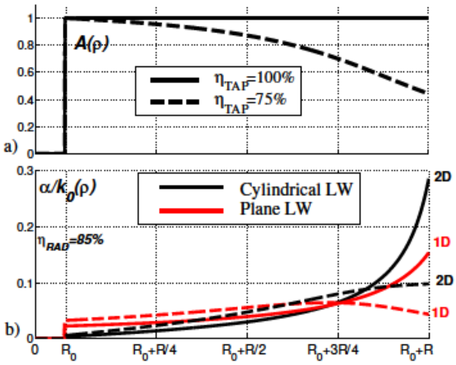

Fig. II.2.3 Effect of aperture distribution and radiation efficiency in the tapering of the cylindrical leaky-wave leakage-rate with $\eta_{RAD} = 85\%$.

and a tapered plane (1D) LW. If perfect uniform distribution with η_{TAP}*=100%* is chosen, maximum α/k_0*=0.15* is requested when tapering a 1D LW to keep the same amplitude of the radiated fields at the lens center and at the edge [74]. This value increases to α/k_0*=0.3* for our case of a cylindrical LW, since the tapered 2D LW must correct not only the amplitude drop due to radiation leakage, but also the cylindrical spreading of the cylindrical wave [81, 86], as expressed by eq II.2.6. To obtain practical lower values of α/k_0, a quasi-uniform function with half amplitude at the edges with respect to the lens center is imposed, as shown with a dashed line in Figure II.2.3.a. This less demanding distribution results in permissible maximum α/k_0*=0.1* for the tapered 2D LW, while keeping a good level of tapering and radiation efficiencies (η_{TAP}*=75%* and η_{RAD}*=85%*).

II.2.1 Design of Radially-Modulated Slot

Once it has been chosen the requested tapering of the 2D LW in terms of the radial modulation of its effective leaky angle $\theta_{RAD}(\rho)$ and its normalized leakage rate $\alpha/k_0(\rho)$, it is needed to find an appropriate planar structure able to support and modulate such tapered 2D LW. The following aspects are indispensable to success in our objective: 1). the structure must be planar and support a cylindrical *backward* LW which is easily fed from a simple central point source. 2). The structure must be able to flexibly and simultaneously control the LW pointing angle and the leakage rate along the radial direction with azimuthal symmetry. 3) Moreover, it would be desirable that the structure could be fabricated and modulated using standard printed-circuit techniques. The aforementioned demands are satisfied by using a dielectric-filled parallel-plate waveguide loaded with printed, circular, periodic double slits placed at $\lambda_{SW}/4$, as shown in Figure II.2.1. This type of structure can be analyzed, for simplicity, as a PPW loaded with slots infinitely extended in one dimension as demonstrated in [88, 89]. Due to the periodicity *P* along the local radial direction, the Floquet theorem gives the space-harmonics (SH) wavenumbers as:

$$k_\rho(\rho) = \beta_n(\rho) - j\alpha(\rho) \tag{II.2.8}$$

$$\beta_n(\rho) = \beta_0(\rho) - n\frac{2\pi}{P(\rho)} \tag{II.2.9}$$

where *n* is the SH index and β_0 is the Bloch wavenumber, which in our case is the one of the TM_0 SW of the dielectric-filled slotted parallel-plate waveguide. In the absence of printed slots, the PPW supports a TEM mode with a dispersion-less normalized phase constant $\beta_{SW}/k_0 = \sqrt{\varepsilon_r}$. This TEM mode is perturbed due to the addition of a pair of transverse slots of width *W*, separated at a distance *d*, and repeated with a period *P*, as sketched in the inset of Figure II.2.4, transforming into a TM_0 SW and the corresponding set of SH. Depending on the value of this unit-cell period *P*, the *n=-1* SH might fall in the visible part of the spectrum if [90]:

$$\left|\frac{\beta_{-1}(\rho)}{k_0}\right| = \left|\frac{\beta_{SW}(\rho)}{k_0} - \frac{\lambda_0}{P(\rho)}\right| = \left|\frac{\lambda_0}{\lambda_{SW}(\rho)} - \frac{\lambda_0}{P(\rho)}\right| < 1 \tag{II.2.10}$$

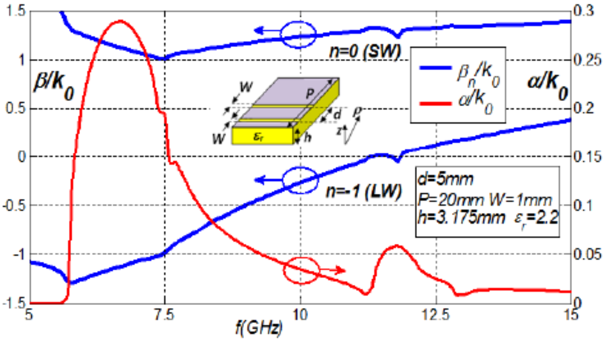

Fig. II.2.4 Frequency dispersion of Bloch wave and n=-1 SH in the double slit grounded dielectric slab.

As an example, the aforementioned unit cell with $h = 3.175mm$, $\varepsilon_r = 2.2$, $d = 5mm$, $P = 20mm$, $W = 1mm$ is analyzed using a home-made MoM code [88]. Figure II.2.4 shows the frequency dispersion of the *SW* Bloch wave ($n = 0$, with $\sqrt{\varepsilon_r} = 1.48$) and associated

$n=-1$ *SH* from $5GHz$ to $15GHz$. With the described dimensions, the studied periodic structure supports a TM_0 Bloch *SW* which is bounded to the dielectric ($\beta_{SW}/k_0 \approx \sqrt{\varepsilon_r} > 1$), while its $n=-1$ *SH* is a fast backward *LW* with $\beta_{-1}/k_0 = -0.25 < 1$ at $10GHz$, and leakage rate $\alpha/k_0 \approx 0.04$. The maximum of radiation can be directly related to the phase constant of the $n=-1$ *SH* by:

$$\sin\theta_{RAD}(\rho) = \frac{\beta_{-1}(\rho)}{k_0} = \frac{\beta_{SW}(\rho)}{k_0} - \frac{\lambda_0}{P(\rho)} \tag{II.2.11}$$

The key aspect of the design is that the periodic printed-circuit must be able to simultaneously modulate the LW pointing direction and leakage rate along its radial direction [74, 85, 91]. For this purpose, two independent geometric variables are requested: in our case these are the period P and the slot width W. From eq II.2.11, it is straightforward to see that varying P one can control the pointing angle of the resulting LW: smaller values of P provide more negative pointing angles (ultimately entering the invisible spectrum with no radiation for $P < \lambda_{SW}/2$), and as P is increased to λ_{SW}, θ_{RAD} tends to broadside. On the other hand, the slot width W will predominantly modify the leakage rate, providing higher leakage for wider slots. Also, the slot width slightly affects the SW phase constant β_{SW}/k_0 in eq II.2.11. Therefore, the simultaneous effect of W and P must be considered when calculating the solution of the dispersion equation, as shown in Figure II.2.4.

Using the tapering design technique proposed in [74, 85], we can simultaneously vary P and W at the fixed design frequency of 10GHz, obtaining the two-dimensional isolevel curves for θ_{RAD} and α/k_0 in the (W,P) plane represented in Figure II.2.5. As shown, θ_{RAD} can be scanned from -45deg to -1deg as P is varied from *15mm* to *23mm*, while α/k_0 can be swept from null radiation when *W=0mm* to maximum α/k_0*=0.15* as W is increased up to *3.5mm*. These geometry-dispersion results are used as a look-up table which allows to find the dimensions P and W that provide the requested tapering of θ_{RAD} and α/k_0 for each radial position ρ.

The result of this search-and-find process is plotted in Figure II.2.5 with a blue line, obtaining the simultaneous modulation of P and W as a function of ρ represented in Figure II.2.6. As it can be seen, the period P must be decreased as we move from the center towards the edge of the lens, from *P=21.5mm* to *P=18.5mm*. This result is coherent with the fact that more negative angles are needed at the edges of the leaky lens. On the other side, the slots width W must be increased from *W=0.25mm* to *W=2.25mm*, since higher leakage rates (up to α/k_0*=0.1* with θ_{RAD}*=-30deg*, according to Figure II.2.2.b) are needed far from the

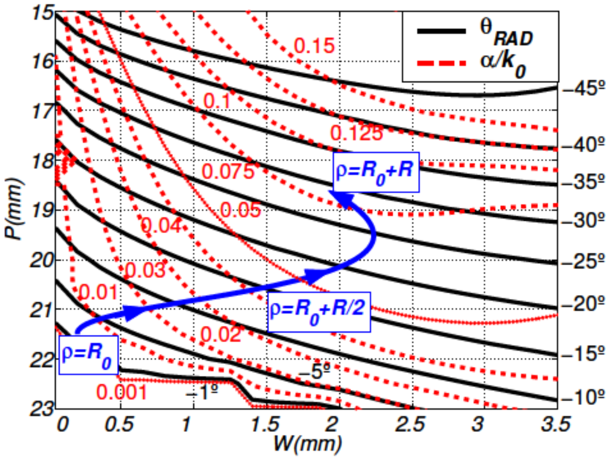

Fig. II.2.5 Two-dimensional dispersion chart at $10GHz$ showing constant θ_{RAD} and constant α/k_0 contour curves as the slots width W and period P are simultaneously varied (the rest of dimensions are summarized in Figure II.2.4).

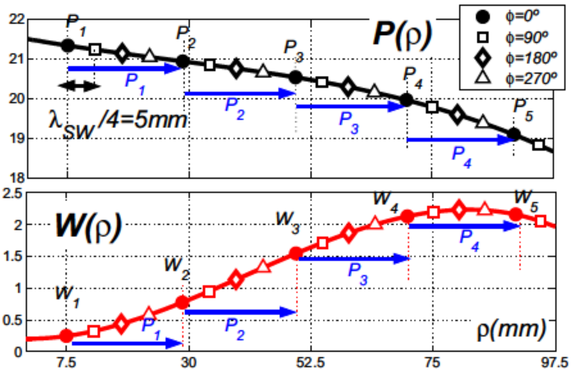

Fig. II.2.6 Radial modulation and sampling of printed-slots width W and period P as a function of azimuthal coordinate ϕ to design the aperture of Figure II.2.2.

feeding point to synthesize the requested quasi-uniform focusing aperture.

The presented methodology is based on the calculation of the full dispersion matrix as a function of P and W. This is the only computational cost in the design process and it is independent of the antenna diameter and aperture field that we would like to synthesize. Even if the presented design has a relatively small aperture diameter, constrained by the maximum possible fabrication size in our university facilities, we will see in the following sections that this methodology leads to a very satisfactory near-field antenna design.

Analysis of the Polarization of the Focusing Pattern

The obtained continuous functions $P(\rho)$ and $W(\rho)$ must be sampled to obtain the radial position and the slot width of each unit cell, for each azimuthal angle ϕ, as illustrated in Figure II.2.6. For $\phi=0deg$, the first values W_1 and P_1 are obtained at $\rho_1=R_0$, which is the location of the first radiating unit-cell (see Figs.II.2.1 and II.2.2). Then, using this value of P_1 we can sample the second values of W_2 and P_2, which are obtained at $\rho_2=\rho_1+P_1$. By repeating this iterative procedure, the dimensions of the five unit cells that comprise the tapered slots for this azimuthal coordinate $\phi=0deg$ are obtained, as represented in Figure II.2.6 with black circles. For other azimuthal angles ϕ, the position of the first slot $\rho_1(\phi)$ is obtained by imposing linear phase-shifting of the radiated leaky fields (or null phase-shifting to radially polarization (RP)), so that circular polarization (CP) at the focus is created as described in [30, 31] (as well named transverse polarization). Then, the same steps are followed to obtain the slots radial positions $\rho_n(\phi)$, widths $W_n(\phi)$, and the distance to the next unit cell $P_n(\phi)$, for any azimuthal angle. This iterative procedure is described by the following expressions where n is the sampling index:

$$\rho_1(\phi) = R_0 + \frac{\phi}{\beta_{SW}} = R_0 + \lambda_{SW}\frac{\phi}{2\pi} \tag{II.2.12}$$

$$\rho_n(\phi) = \rho_1(\phi) + \sum_{j=1}^{n-1} P_j(\phi) \tag{II.2.13}$$

$$P_n(\phi) = P(\rho_n, \phi) = P\{\rho = \rho_n(\phi)\} \tag{II.2.14}$$

$$W_n(\phi) = W(\rho_n, \phi) = P\{\rho = \rho_n(\phi)\} \tag{II.2.15}$$

Figure II.2.6 illustrates the sampling of the continuous modulation curves $P(\rho)$ and $W(\rho)$ for the azimuthal angles $\phi=0deg,90deg,180deg,270deg$, which are respectively represented with circles, squares, diamonds and triangles. Notice that according to eq II.2.12 there is a spatial shift equal to $\Delta\rho=\lambda_{SW}/4$ between the position of slots separated an angle $\Delta\phi=90deg$ in the azimuthal coordinate for circular polarization. As a result, an Archimedean-spiral-shaped double-slot printed-circuit with modulated width and period as a function of the polar coordinates: $W(\phi,\rho)$ and $P(\phi,\rho)$, is obtained. This layout is sketched in Figure II.2.1. Similar Archimedean spiral shapes were reported in the design of CP holographic antennas [30, 31] and RLSA [92]-[93] for far-field radiation. On the other hand, if we do not use a spatial shift ($\Delta\rho = 0$) a concentric ring geometry will be obtained and the sampling in

Figure II.2.6 will only take into account the black circles.

The use of a continuous double slot separated at $\lambda_{SW}/4$ is proposed here. This geometry reduces reflections and therefore the excitation of higher azimuthal modes. These modes will have affected the quality of the synthesized fields reducing the applicability of this methodology.

II.2.2 Analysis of Focused Fields

Once the modulated printed-slot has been designed, the fields can be efficiently analyzed. The following analytical expressions allow the computation of the complex continuous aperture distribution created by a cylindrical LW with a given radially-tapered longitudinal complex propagation wavenumber $k_\rho(\rho)$ as given by eq II.2.8. Besides, the phase shift introduced by the first radiating position as a function of the azimuthal coordinate in $\rho_1(\phi)$ eq II.2.12 is taken into account:

$$k_\rho(\rho) = \beta(\rho) - j\alpha(\rho) = k_0 \sin\theta_{RAD}(\rho) - j\alpha(\rho) \tag{II.2.16}$$

$$\Phi(\phi) = \beta_{SW} \cdot \rho_1(\phi) = 2\pi \frac{R_0}{\lambda_{SW}} + \phi \tag{II.2.17}$$

$$E_{LW}^{AP}(\rho,\phi) = \sqrt{\frac{\alpha(\rho)}{\rho}} e^{-\int_{\rho_1(\phi)}^{\rho} \alpha(\rho) d\rho} e^{-j\int_{\rho_1(\phi)}^{\rho} \beta(\rho) d\rho} e^{+j\Phi(\phi)} \tag{II.2.18}$$

$$\vec{E}_{LW}^{AP}(\rho,\phi) = E_{LW}^{AP}(\rho,\phi) \cdot \vec{\rho} \tag{II.2.19}$$

It must be noticed that at this stage, the continuous-aperture field obtained with eq II.2.19 is identical to the reference aperture field from eq II.2.1 with the exception that the azimuthal dependence of the phase and vectorial behavior have been introduced in eq II.2.19. The actual aperture field created by the discrete slots can be retrieved by radially sampling (eq II.2.19), to obtain the equivalent magnetic currents at the discrete slots:

$$\vec{E}_{LW}^{AP,SAMPLE}(\rho_n,\phi) = \left\{ \vec{E}_{LW}^{AP}(\rho,\phi) \quad \rho = \rho_n(\phi) \right. \tag{II.2.20}$$

Once the methodology to design a near-field focusing leaky wave antenna in printed technology is established, an example of design is presented in the next Chapter.

Chapter II.3

Circularly Polarized Slot LWA

In this chapter we apply holographic concepts to design a leaky-wave lens, which focuses the radiated fields in the Fresnel region with circular polarization. For this purpose, the complex LW wavevector must be locally modulated across the radiating aperture, creating a non uniform LW which converges with optimum aperture taper and focusing efficiencies at the desired focal distance, as theoretically demonstrated in [73, 74].

Introduction

Near-field focusing by LWs has been recently proposed in [77]-[90] with application to generation of Bessel beams. However, in this application the LW was not modulated to obtain optimum focusing. Convergence of SW propagating in planar substrates has been reported for the design of planar Luneberg lenses [52]-[94], which focus the electromagnetic fields inside the hosting medium by properly modulating the effective refractive index. However here it is shown that cylindrical LWs [81] can also be tailored to synthesize three-dimensional focused near-field regions in free-space. We also report full-wave simulations of the designed holographic lens obtained with commercial software [95], validating the proposed synthesis and analysis technique. As explained in Chapter II.2, it is necessary to confirm our initial assumption of a single dominant tapered leaky mode which can efficiently represent the radiated fields of this structure.

II.3.1 Optimized Design

Figure II.3.1 represents the magnitude of the aperture fields for the designed tapered cylindrical LW, by using the continuous and the discrete aperture expressions. The designed quasi-uniform amplitude tapering of the aperture fields can be observed, with a decay to half amplitude at the lens edge with radius $R=3\lambda_0$, and with a central region of radius $R_0=\lambda_0/4$ which is not illuminated. Also, the Archimedean double-slot shape becomes evident in Figure II.3.1.b for the discrete aperture field which is sampled over the slots. Then, using the Green's function in free space for magnetic currents, being $\vec{m}(\rho',\phi')=-\vec{z}$, one can compute the near-fields radiated by the complex aperture distribution induced by the tapered cylindrical LW.

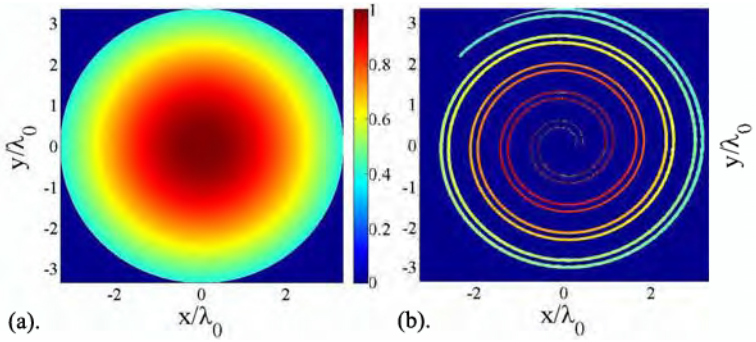

(a). (b).

Fig. II.3.1 Amplitude of aperture fields for the tapered cylindrical LW antenna designed in Figure II.2.2. (a). Continuous aperture fields (b). Discrete aperture fields over slots. The intensity of the field is linearly normalized and λ_0=30mm at 10GHz.

Figure II.3.2 illustrates the components of the electric near-field in the zy plane ($\phi = 90deg$), predicted by the proposed cylindrical tapered LW aperture theory. Transverse field components (E_x and E_y) with focused region located around $y=0, z=6\lambda_0$ are obtained. The typical ellipsoidal shape focal region, with a focal width in the transverse y-direction which is narrower than the focal depth in the axial z-direction [61, 74] is observed. On the other hand, the vertical E_z component vanishes at the lens axial direction, and two symmetrical focused regions with lower intensity than the transverse components appear.

The computed near-fields along the z-axis are plotted in Figure II.3.3, showing the differences between the use of continuous (eq II.2.19) or discrete (eq II.2.20) aperture fields in the axial cut. As it can be seen, both techniques provide similar results due to two reasons:

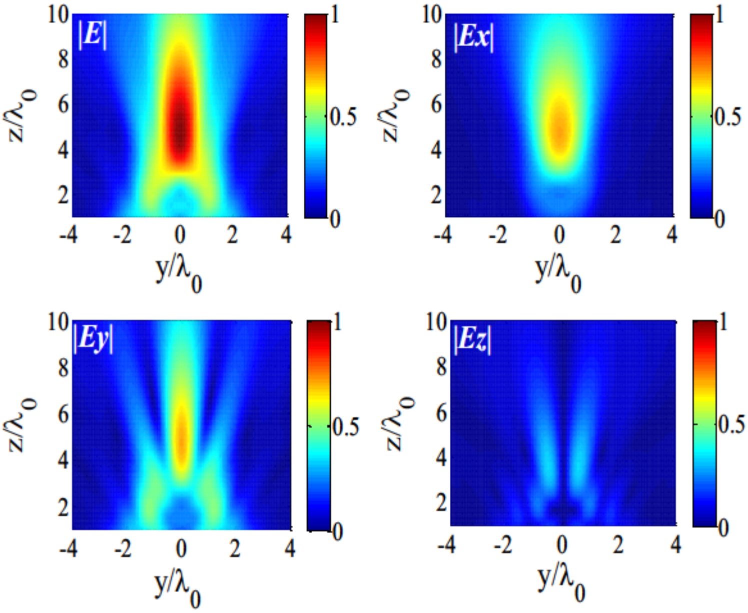

Fig. II.3.2 Theoretical near-fields in the *zy* plane ($\phi = 90deg$). The intensity of the field is linearly normalized and $\lambda_0 = 30mm$.

1-The modulated leaky mode is dominant and provides the actual amplitudes and phases for the radiation of each slot of the non-uniform array [82].

2-The slots are in close proximity (in the order of $0.6\lambda_0$, as shown in the values of P around *20mm* obtained from Figure II.2.6), satisfying the Schelkunoff sampling criterion [80].

As a result, the reference continuous aperture field from eq II.2.1 used to obtain the tapered leaky-wave functions of eq II.2.5-II.2.7, is a good approximation to the actual aperture field on the discrete slots, validating the initial assumption of a dominant modulated leaky field. The main effect of the discretization is the decrease in the forelobe level from -10 to -20 dB. Nevertheless, the position and shape of the focal region are almost unaffected by the discretization of the slots. In any case, no *z*-component theoretically exists at the focal axis, while *x* and *y* components are amplitude-balanced (Figure II.3.3.a) and phase shifted 90*deg* (Figure II.3.3.b) due to the designed Archimedean-spiral topology. The tapered LW aperture theory predicts a 3dB focal depth $\Delta_z = 5\lambda_0$ with a maximum intensity point at $I = 4.5\lambda_0$, which is closer to the aperture than the designed geometrical focus $F = 6\lambda_0$ due to the well-known focal shift phenomenon [61].

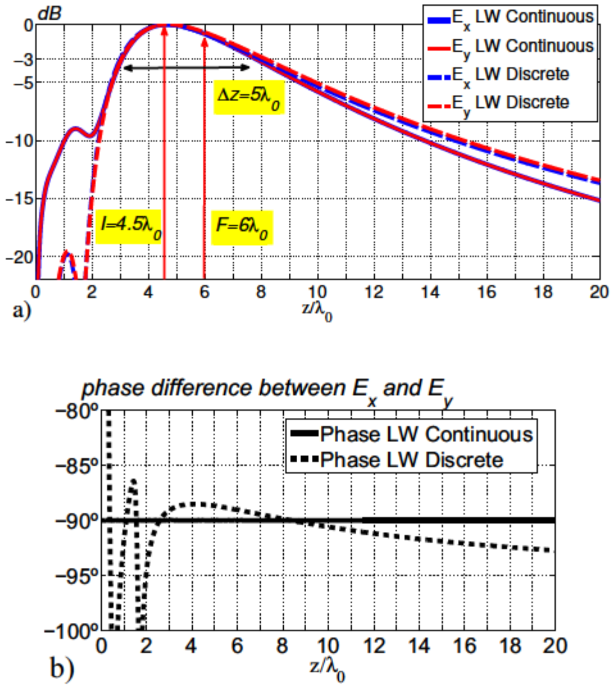

Fig. II.3.3 Theoretical (a). amplitude and (b). phase near-field patterns along the axial cut (z-axis) of the designed holographic lens.

The fields in the transverse xy plane at a height $z = I = 4.5\lambda_0$, are plotted in Figure II.3.4 in logarithmic scale. The right-handed circularly polarized (RHCP) near-fields are obtained as:

$$E_{RHCP} = \frac{E_x - jE_y}{\sqrt{2}} \tag{II.3.1}$$

As it can be seen in Figure II.3.4, the focusing pattern is almost symmetrical with respect to the azimuthal coordinate. Pure RHCP fields are obtained at the focal axis ($x = y = 0$), with null E_z and LHCP fields which increase out from the lens center and reach a maximum at a radial distance of one wavelength surrounding the focal center.

Transverse cuts in the principal planes (x-axis $\phi = 0deg$, and y-axis $\phi = 90deg$ for $z = I = 4.5\lambda_0$) are represented in Figure II.3.5. The theoretical RHCP focus presents similar 3dB focal widths in both planes, $\Delta_x = \Delta_y = \lambda_0$. According to eq II.2.4, and considering the focusing distance $4.5\lambda_0$, this focal width corresponds to a focusing efficiency of η_{FOC}=75%.

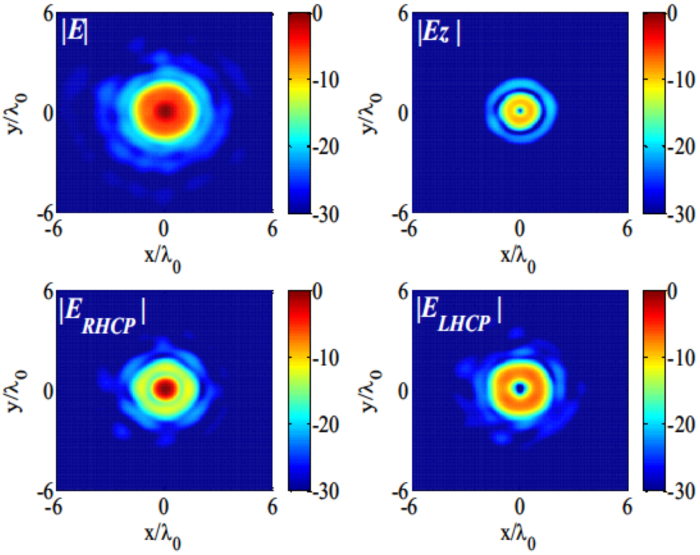

Fig. II.3.4 Theoretical near-fields in the xy plane at $z = I = 4.5\lambda_0$. The intensity of the field is in decibels and $\lambda_0 = 30mm$.

This result theoretically demonstrates the success to obtain high aperture taper efficiency η_{TAP}=75% in the designed lens.

The RHCP sidelobe level is below -10dB, and LHCP fields increase up to 8dB below the main RHCP beam. This high cross-polarization is inherent to the way the circularly polarized fields are obtained with the progressive phase-shift created by the variation of the initial radius. This makes that the x and y components of the aperture fields do not have a phase shift of 90*deg* over the whole radial distance, as it can be seen in Figure II.3.5.c for the x-axis (similar results are obtained in the y-axis). Particularly, it can be observed at the aforementioned distance of one wavelength from the center, a change in the phase difference from -90*deg* to almost 90*deg*, maximizing the generation of LHCP fields. Compared to the annular slot antenna [96] or the RLSA [92]-[93], our design does not allow the arbitrary control of the polarization because of the use of a continuous slit instead of several discrete perpendicular slots, and as a result the circular polarization is rigorously obtained only on the antenna axis. Similarly in Figure II.3.5.a and II.3.5.b, the axial z-component vanishes at x=y=0, but presents a level of -8dB at this radial distance of one wavelength surrounding the focal center, as it was also illustrated in Figure II.3.2 and Figure II.3.4.

The effect of the discretization observed in Figure II.3.5 is an increase in the sidelobe

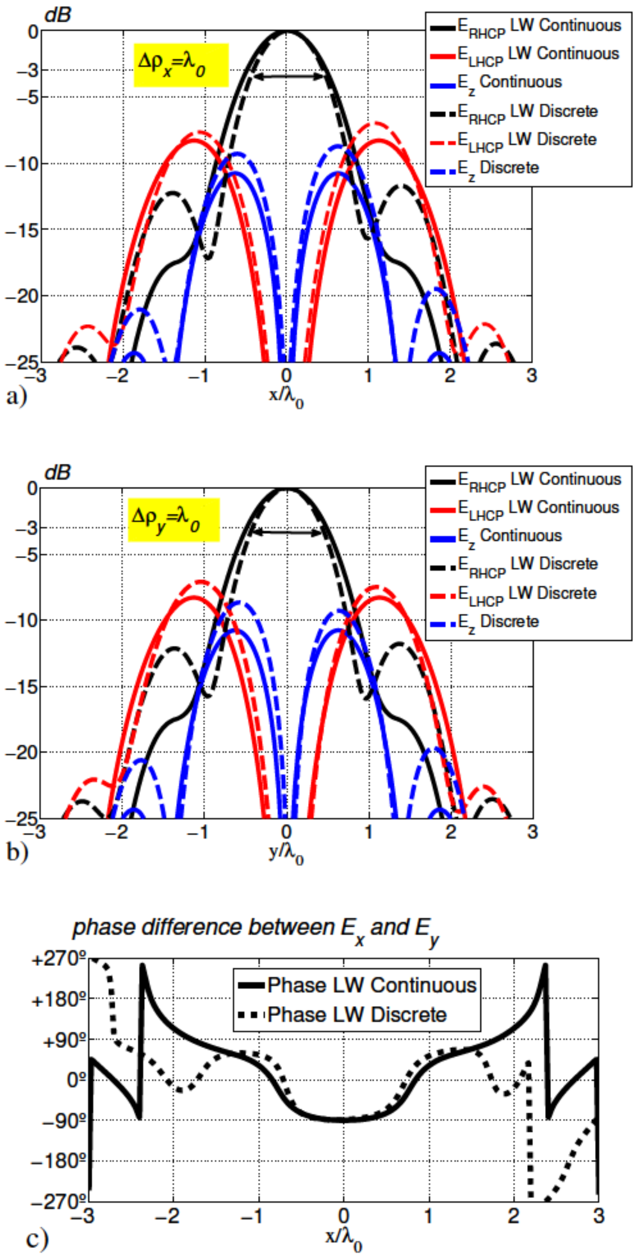

Fig. II.3.5 Theoretical near-field patterns along the principal transverse cuts for $z = l = 4.5\lambda_0$. Amplitude in (a). x-axis (b). y-axis, (c). phase in x-axis.

level for all the components. Also, it can be seen that the loss of azimuthal symmetry is more evident for the case of the discrete aperture, observing higher discrepancies between the x- and the y-cuts, as a result of the unevenness of the sampled spiral slot circuit. Nevertheless, as commented for the axial cut results in Figure II.3.3, there is a tight correspondence between the reference continuous-aperture fields and the actual discrete-aperture fields.

Validation with Full-Wave Commercial Solver

The 3D CAD model of the designed lens shown in Figure II.2.1 has been simulated using commercial CST solver [95]. The near-field patterns obtained from CST are compared with the theoretical results for tapered cylindrical LWs using the discrete aperture expressions. Figure II.3.6.a shows the amplitude of the electric field components in the axial cut. The axial component obtained from CST is below -20dB, while the balanced transverse components follow the theoretically predicted axial focusing pattern. This confirms the synthesis of the focal region at the designed focal distance and with the expected depth of focus. Also, the theoretical quadrature phase shift along the axial direction is validated with CST results, as plotted in Figure II.3.6.b. The transverse cuts obtained from CST are also in good agreement with theoretical results, for all field components (RHCP, LHCP and axial E_z) as shown in Figure II.3.7. The RHCP focal widths predicted by CST are consistent with theory, thus confirming the high synthesized focusing efficiency over 70%. On the other hand, the radiation efficiency given by CST is 82%.

Minor discrepancies are observed for the sidelobes and cross-polarization level, and stronger asymmetry between both principal planes is predicted by CST. This is probably due to the limitations on the proposed leaky-wave analysis method which: 1). Considers a periodic 1D geometry to calculate the local leaky-wave propagation constant (in order to minimize this possible effect a smooth variation of the period is imposed in the synthesis method). 2). Does not include reflections at the end of the spiral (these are assumed to be small as a consequence of the high radiation efficiency). 3). Ignores possible space-wave contributions on the slot currents. Nevertheless, the agreement between full-wave results and the tapered cylindrical LW theory is sufficient to validate the developed analysis and synthesis methodology (which is based on the assumption of a dominant modulated leaky-wave field), and to theoretically confirm the proposed new idea to design planar microwave lenses.

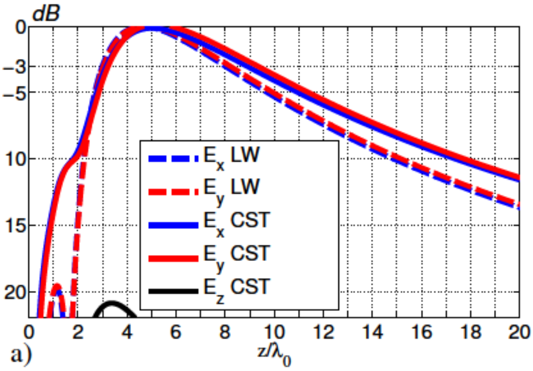

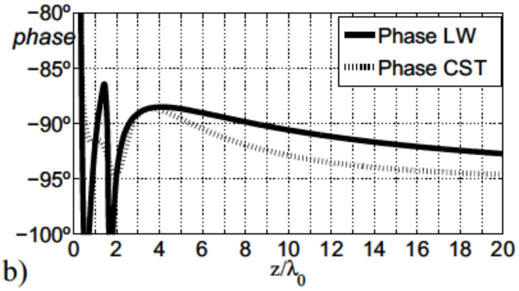

Fig. II.3.6 Validation of axial near-field focusing patterns comparing CST simulations of the designed holographic lens and tapered LW aperture theory.

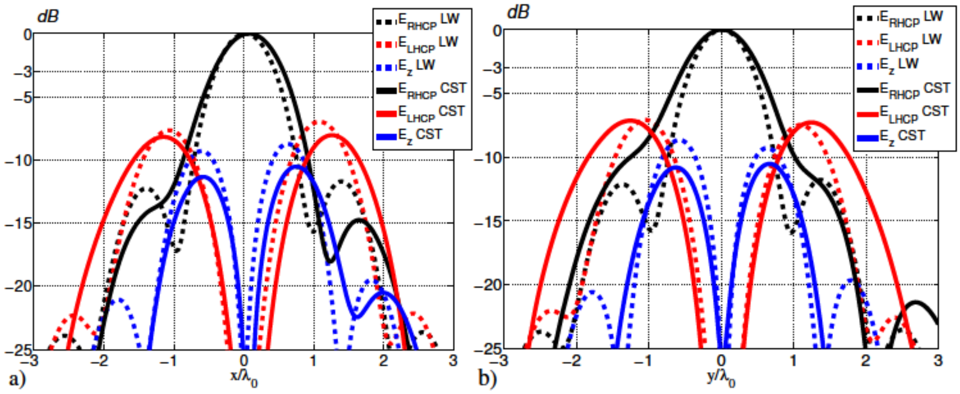

Fig. II.3.7 Validation of transverse near-field focusing patterns comparing CST simulations of the designed holographic lens and tapered LW aperture theory.

Description of Frequency Steering of Focal Length

This subsection reports experimental results which demonstrate the possibility to synthesize focused near-fields from a planar printed circuit which is fed with a simple coaxial probe. A prototype operating at $10GHz$ has been manufactured and tested. As predicted by the theory described before in this chapter, high 75% focusing efficiency of circularly polarized fields is obtained as a result of the proper modulation of the dimensions of the Archimedean-shaped printed slot. The designed coaxial feeding provides good matching (below $-10dB$) in the entire frequency band. Finally, the scanning of the focal length as a function of the frequency is described in next section, showing measured results and accurate theoretical explanation based on the frequency dispersion of the tapered leaky mode. This phenomenon is general for this type of 2D leaky-wave lenses, and might find many applications in imaging, sensing and heating.

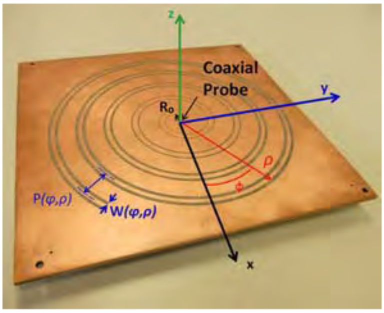

Fig. II.3.8 Photograph of fabricated holographic leaky-wave lens (LWL) in printed-slot technology.

II.3.2 Prototype and Experimental Results

Figure II.3.8 shows a picture of the fabricated prototype. The modulated dimensions (position P and width W) of the printed slots were designed in the previous Chapter (see Figures II.2.5 and II.2.6) and further details can be seen in Appendix A. Rogers Duroid 5880 substrate with thickness $h = 3.175mm$, $\varepsilon_r = 2.2$, and $tan\delta = 0.002$, and with a total size of $20cm$ x $20cm$ ($6.67\lambda_0$ x $6.67\lambda_0$ at $10GHz$) has been used.

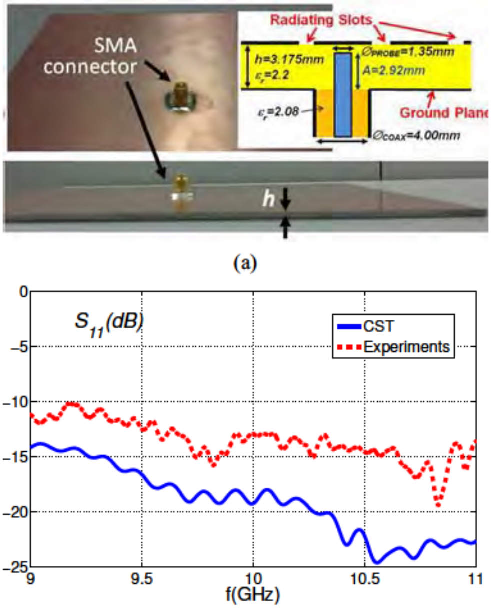

(a)

(b)

Fig. II.3.9 (a). Feeding coaxial probe, illustrating the main dimensions and (b). comparison between simulated and experimental input matching of the fabricated holographic leaky-wave lens.

Design of Integrated Coaxial Feeding

A key feature of the novel planar lens is that it affords a simple single-source integrated in the supporting substrate, in opposition to more complicated feeding networks used in phased-array printed lenses [67]-[69], or external spherical-wave feeders needed in reflectarrays [70]. The scheme of the vertical coaxial feeding, depicted in the inset of Figure II.3.9 together with its main dimensions, is typical of radial-line slot antennas (*RLSA*) [92]-[32], commonly used to create low-cost large directive antennas. This circuit is located at the lens center, and a SMA connector at the bottom ground plane provides the interface to RF cables as shown in the pictures of Figure II.3.9. The probe penetration A has been tuned to optimize the input matching, obtaining $S_{11} < -10dB$ in $9GHz - 11GHz$ bandwidth as shown by CST simulations and measurements in Figure II.3.9. The discrepancies are due to tolerances and errors in the adjustment of the aforementioned probe depth A.

A near-field measurement set-up has been prepared using foam substrate to support a field probe as shown in Figure II.3.10. The orientation of this probe is varied to measure the different components of the electric field along the main axes of the lens. Several probe

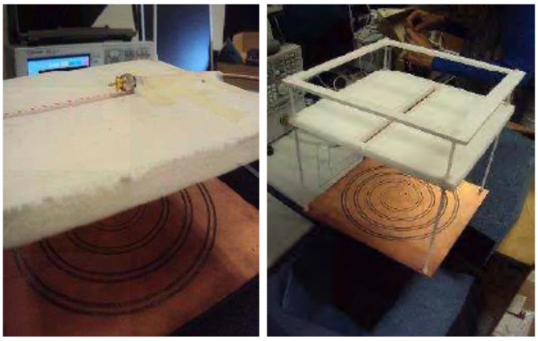

Fig. II.3.10 Designed experimental setup.

dimensions have been studied in order to minimize its impact on the measured field. It has been found out that the most critical parameter is the length of the probe which has to be minimized. The optimized probe length is 6*mm* and the coaxial diameter 5*mm*, both small in terms of the wavelength. Therefore a small perturbation of the antenna near-field is expected. The scanning range is around $7\lambda_0 = 21cm$ in both axial and transverse planes. The scanning step, 5*mm*, is chosen to be similar to the probe length.

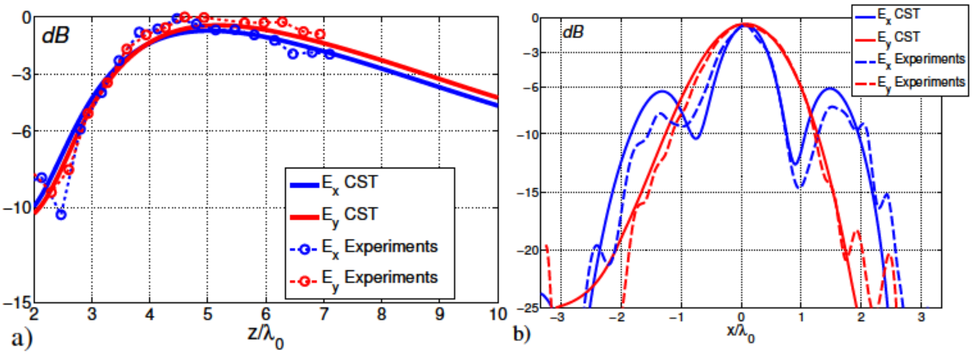

Fig. II.3.11 Comparison between simulated and measured near-field focusing patterns of the fabricated holographic leaky-wave lens at 10GHz (a). axial cut along z-axis (x=y=0) (b). transverse cut along x-axis (z=139mm).

Figure II.3.11 compares the measured and simulated *x*- and *y*-near-fields at the design frequency of 10*GHz*. The axial cut is represented in Figure II.3.11.a, showing that the measured focal depth and position of the focus perfectly match the theoretical results, and that both components are well balanced. The transverse cut in the x-axis ($\phi = 0deg$) at the focal height $z = 139mm$ ($4.63\lambda_0$) is plotted in Figure II.3.11.b. Very good agreement between measured and theoretical near-fields is shown for the focal widths and sidelobe levels. Thus, these results experimentally confirm the high focusing efficiency of the designed prototype. Note that it is not possible to measure the relative phase difference between different field components necessary to plot the fields in circular polarization, due to the fact that we need to manually rotate the probe.

II.3.3 Frequency Steering of the Focus

Leaky-wave antennas are known to be strongly frequency dispersive: this behavior has been classically used in $1D$ leaky lines to scan a fan beam in the far-field [97]. Recently, it was theoretically demonstrated in [74] that a $1D$ leaky lens has the equivalent property in the near-field, resulting in the shifting of the position of the focus as the frequency is varied. However, the case of $1D$ leaky-line sources is quite different to the scenario studied here of $2D$ leaky apertures. $2D$ leaky-wave antennas are normally operated at the frequency which satisfies the splitting-condition to radiate a pencil beam at broadside [97]-[31]. For lower frequencies the gain at broadside drops as a consequence of the cutoff regime of the leaky wave, while for higher frequencies the pencil beam transforms into a conical beam [97],[14]. In this section we study the behavior with frequency for a focused $2D$ leaky aperture, showing that the focal length can be steered up to a limit as the frequency of the signal is shifted. Theoretical results based on the dispersion of the modulated cylindrical leaky-wave accurately predict the performance of the holographic lens with frequency, which is validated with experiments.

Frequency Response of Focused Cylindrical Leaky Wave

In [98], it was demonstrated that a single modulated leaky wave can be used to represent the field radiated by the holographic lens antenna. Therefore, by studying the variation of the cylindrical leaky-wave complex wavenumber along the lens radial distance versus frequency, we can characterize the frequency steering of the focal length. The designed modulated dimensions of the printed-slot $W(\rho)$, $P(\rho)$ are used as fixed parameters in a modal solver [88], which provides the phase and attenuation terms of the leaky wave as a function of frequency, and for each radial position of the slot unit-cell:

$$k_\rho(\rho, f) = \beta(\rho, f) - j\alpha(\rho, f) \qquad \text{(II.3.2)}$$

Particularly, the modulated leakage angle θ_{RAD}, has a strong dependence with the modulated distance between slots $P(\rho)$ and with frequency, which can be expressed as:

$$\sin\theta_{RAD}(\rho,f) = \frac{\beta(\rho,f)}{k_0} = \frac{\beta_{SW}(\rho,f)}{k_0} - \frac{c_0/f}{P(\rho)} \tag{II.3.3}$$

The term $c_0/(fP(\rho))$ in eq II.3.3 (where c_0 is the speed of light in vacuum) describes a variation in the resulting scanning angle from backward-endfire to broadside as frequency is increased, as it customarily happens in frequency-scanning antennas [97]. This can be seen in Figure II.3.12 , where the dispersion of the modulated cylindrical leaky wave as a function of the radial distance of the designed lens is represented for five different frequencies in the $9-11GHz$ band. At the design frequency of $10GHz$, it is shown in Figure II.3.12.a that $\theta_{RAD}(\rho)$ follows the specified variation from $\theta_{RAD} = -5deg$ at $\rho = R_0 = 7.5mm$ to $\theta_{RAD} = -30deg$ at the lens edge position $\rho = 97.5mm$. For lower frequencies, the modulated $\theta_{RAD}(\rho)$ is shifted to more negative values, reaching a variation from $-15deg$ to $-50deg$ at $9GHz$. On the contrary, higher frequencies tilt the local scanning angles towards broadside, as can be seen at $11GHz$ with a variation of θ_{RAD} from $0deg$ to $-15deg$. Actually, the central region of the lens is in the stopband regime at this frequency of $11GHz$, and therefore this central zone does not contribute to radiation. This stopband regime is characterized by null values of θ_{RAD} and a sudden rise in α/k_0 [97],[87], as it can be observed in Figure II.3.12 at $11GHz$ in the section contained between $\rho = 0mm$ and $\rho = 40mm$.

Nevertheless, the dispersion with frequency suffered by the locally-modulated radiating angle is shown in Figure II.3.12.a, translates in a displacement of the focal length as qualitatively illustrated in Figure II.3.13. For higher frequencies the emerging rays tend to broadside, thus converging at a higher distance. Besides, it is expected that the focal depth noticeably increases for higher frequencies as a result of the increased focal height [61]-[63], as also illustrated in Figure II.3.13 .

To accurately compute the near-fields created by the designed lens at any frequency, one can modify the analysis theory presented in [98], obtaining the following complex aperture fields as a function of frequency:

$$\vec{E}^{AP}_{LW}(\rho,\phi,f) = A(\rho,\phi,f)\cdot e^{+j\Psi(\rho,\phi,f)}\cdot e^{+j\Phi(\phi,f)}\cdot\vec{\rho} \tag{II.3.4}$$

$$A(\rho,\phi,f) = \sqrt{\frac{\alpha(\rho,f)}{\rho}}e^{-\int_{\rho_1(\phi)}^{\rho}\alpha(\rho,f)d\rho} \tag{II.3.5}$$

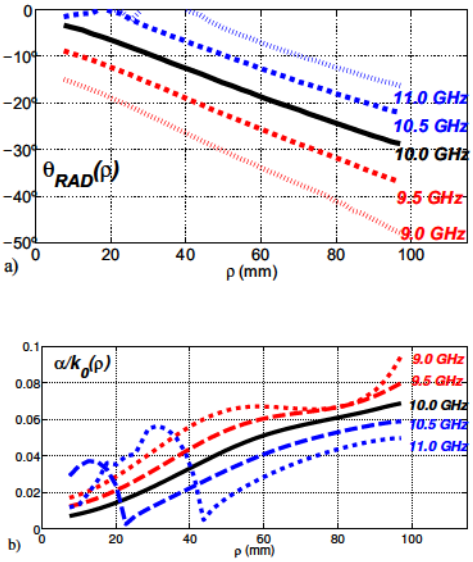

Fig. II.3.12 Dispersion with frequency of the tapered cylindrical leaky wave along the radial distance of the designed holographic lens. (a). pointing angle and (b). leakage rate as a function of the frequency.

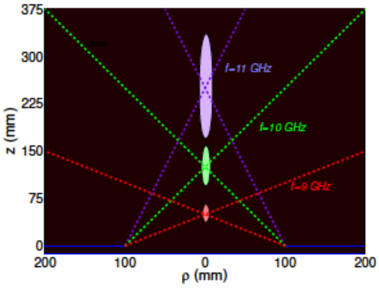
375
300
225
150
75
0
z (mm)
f=11 GHz
f=10 GHz
f=9 GHz
200
100
0
100
200
ρ (mm)

Fig. II.3.13 Scheme illustrating the dispersion of the focal region with frequency.

$$\Psi(\rho,\phi,f) = -\int_{\rho_1(\phi)}^{\rho} \beta(\rho,f)d\rho \tag{II.3.6}$$

$$\Phi(\phi,f) = \beta_{SW}(f)\cdot\rho_1(\phi) = 2\pi\frac{R_0}{\lambda_{SW}(f)} + \frac{\lambda_{SW}(f_0)}{\lambda_{SW}(f)}\phi \tag{II.3.7}$$

Where the term A describes the amplitude modulation of the aperture (due to the tapering of the leaky-phase constant), Ψ stands for the phase modulation due to the tapering of the leakage rate, and the term Φ describes the azimuthal phase-shift variation created by the spiral shape. As an example, Figure II.3.14 shows the variation with frequency of the amplitude and phase terms A and Ψ for $\phi = 0deg$ (x-axis), when introducing in eq(II.3.5) and eq(II.3.6) the tapered leaky-mode dispersion behavior shown in Figure II.3.12 for the five studied frequencies.

Already by looking to the frequency variation of these terms, one can study the impact of the frequency on the near-fields. This theory is particularly suited to analyze large antennas as a function of the frequencies, where direct full-wave simulations become prohibitive. As shown in Figure II.3.14.a, the aperture phase Ψ has a quadratic-type parabolic response whose eccentricity decreases for higher frequencies (which will result in a higher focal point). The amplitude of the aperture fields in Figure II.3.14.b also changes as frequency is varied, observing at higher frequencies the non-illuminated central region due to the aforementioned stopband.

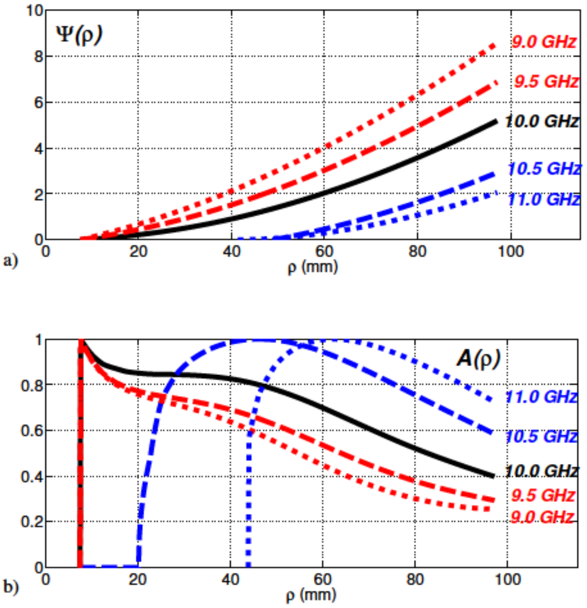

Fig. II.3.14 Dispersion with frequency of the aperture fields along the radial distance for $\phi = 0deg$, in the designed holographic lens.

The theoretical near-fields created by the focused aperture at any frequency can be computed using a Green's function formalism. Figure II.3.15 shows the intensity of the fields at the *zy* plane, and for four different frequencies. The focused region shifts to higher heights as frequency moves from $9GHz$ to $11GHz$, and it is also observed an evident enlargement of the $3dB$ focal depth in the z-axis. On the other hand, the $3dB$ focal width along the y-axis does not change as intensely as frequency is varied. For $12GHz$, the focusing pattern strongly varies, and the focal region is no more located at the lens vertical z-axis. The single focus located at $y = 0$ splits into several hot spots. This phenomenon is similar to the splitting condition in $2D$ leaky-wave antennas focused at the far-field regime, whose single-beam focused at broadside splits into a scanned conical beam for higher frequencies [97]-[87]. Similarly, for the case of $2D$ leaky-wave lenses focused in the near-field zone, it is obtained a splitting from a single focus to a conical (toroidal) focus.

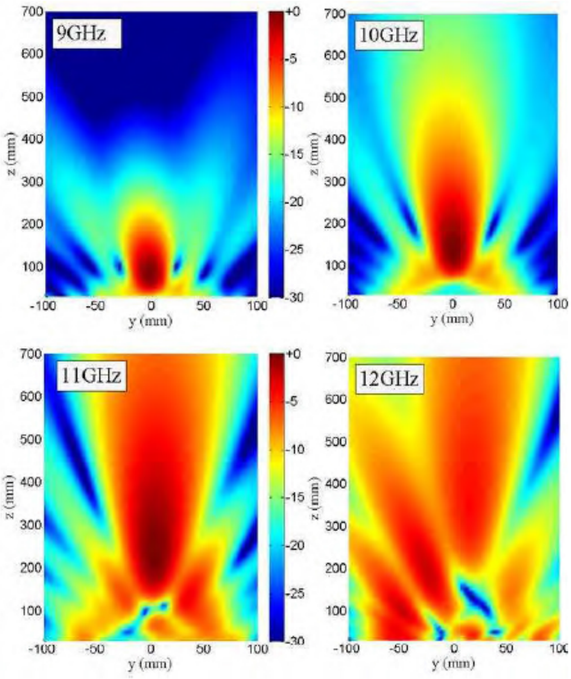

Fig. II.3.15 Theoretical near-field intensity at zy-plane as a function of frequency.

This behavior with frequency is also evident in Figure II.3.16 , which represents the field cuts in the transverse *xy* plane for each studied frequency, and for the resultant focal height ($z = 84mm$ at $9GHz$, $z = 139mm$ at $10GHz$, and $z = 240mm$ at 11GHz). A single focal region with maximum energy concentrated above the lens center ($x = y = 0$) is obtained for the scanning band comprised between 9 and 11GHz. At 12GHz, however, it is clearly observed the splitting of the focus into two focused zones approximately located at $x = 0$ and $y = \pm 50mm$. This splitting condition above 11GHz limits the upper operation frequency of the scanning lens. On the other hand, the lower frequency band is determined by the radiation cutoff of the TM_0 leaky-wave, which in our case is below $9GHz$.

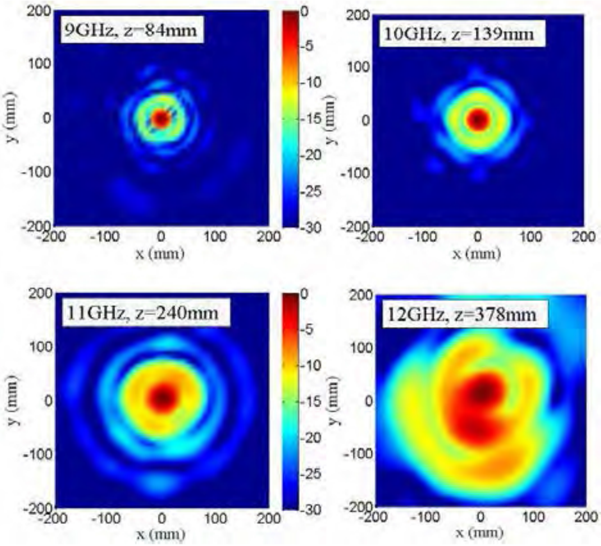

Fig. II.3.16 Theoretical near-field intensity at xy-plane as a function of frequency and for the corresponding focal heights.

The results shown in Figure II.3.15 and Figure II.3.16 correspond to the RHCP component. The response of the cross-polarization LHCP component as frequency is varied in the steering bandwidth (9-11GHz) is also shown in Figure II.3.17.a for the transverse x-cut, and for the corresponding focal heights (results are similar for the y-cut).

As it can be seen, pure RHCP focused near-fields are obtained at the lens axis ($x = y = 0$) in the entire scanning bandwidth, with increased RHCP and LHCP sidelobes as the focal height is frequency steered. Also, it is shown an increase of the focal width as the focal length is enlarged. The level of the LHCP is relatively high due to the limited control of the polarization in the presented lens antenna. A design based on resonant perpendicular slots such as the ones used in RSLA antennas [92]-[32] would have led to a better control of this polarization. This increase in the LHCP can be attributed to the spatial distortion suffered

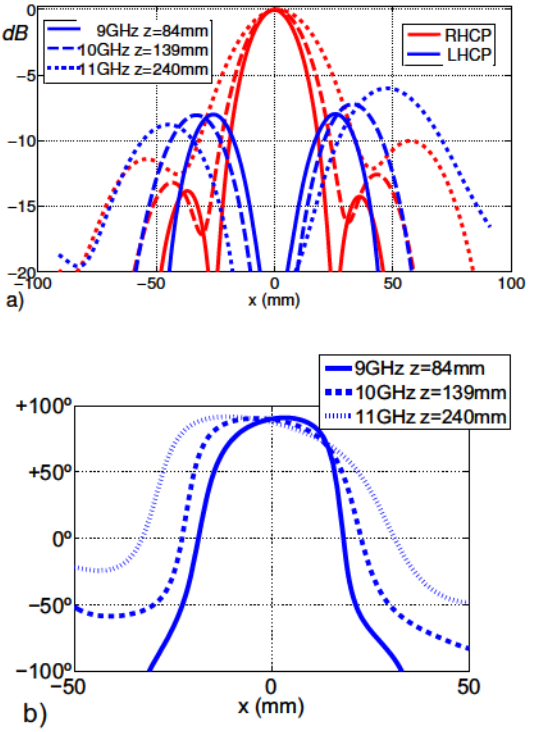

Fig. II.3.17 Intensity of the theoretical near-field along x-axis for the corresponding focal heights as a function of the frequency. (a). amplitude and (b). phase patterns.

by the phase pattern, which is shown in Figure II.3.17.b.

Experimental Validation of Frequency Dispersion

The near-fields were measured along the z-axis from $z = 5mm$ to $z = 213mm$ for five frequencies in the $9.2-11GHz$ band. The measured E_x component is compared with the field obtained from the theoretical dispersion of the leaky wave (LW), showing very good agreement as it can be seen in Figure II.3.18. As predicted by theory, the focal length and the focal depth augment as frequency is increased. The amplitude of E_y component presents similar response with frequency, and it is not shown for brevity. As expected, balanced amplitude of the transverse fields and negligible E_z component was obtained for all this scanning frequency range.

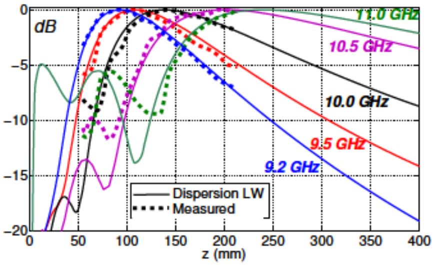

Fig. II.3.18 Frequency dispersion of E_x field intensity at the axial cut.

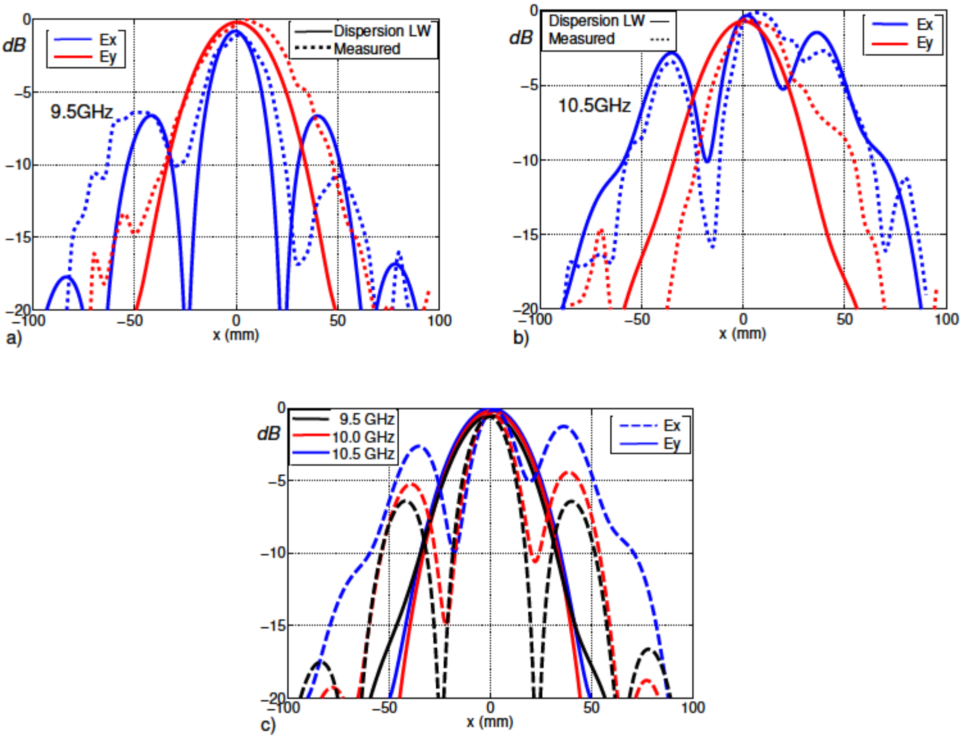

Fig. II.3.19 Frequency dispersion of field intensity along x-axis for z=139mm.

The E_x and E_y fields in the transverse x-axis ($\phi = 0deg$) at a fixed height, $z = 139mm$, are shown in Figure II.3.19.a and Figure II.3.19.b at 9.5GHz and 10.5GHz, respectively. The agreement with the measurements is in within the possible inaccuracies introduced by the measurement setup when displacing manually the probe. The experiments are consistent with theory, thus validating the approach to obtain the frequency dispersion of the fields also in the transverse directions. Figure II.3.19.c compares the theoretical distortion of the transverse focusing pattern at a fixed height as frequency is varied, observing that the highest focusing effect (minimum focal width for E_y) is obtained at 10GHz, which corresponds to the frequency for which the focal distance is located at the observation height $z = 139mm$. Similar validation for the fields in the transverse y-axis ($\phi = 90deg$) was obtained, but it is not shown due to space restriction.

Figure II.3.20.a shows the variation of the focal length, width and depth, as frequency is shifted between 9GHz and 11GHz. CST results are compared with theoretical results based on the leaky wave theory, and also experimental data are plotted with circles, observing good agreement. Figure II.3.20.a also summarizes the performance of the novel holographic lens as a frequency-steering device with 20% bandwidth.

The focal length can be scanned from $z = 84mm$ at 9GHz to $z = 240mm$ at 11GHz, observing increased steering sensitivity (mm/GHz) for higher frequencies. The focal depth has a corresponding growth from $\Delta z = 85mm$ at 9GHz to $\Delta z = 300mm$ at 11GHz, while the focal width Δx changes from $\Delta x = 22mm$ at 9GHz to $\Delta x = 41mm$ at 11GHz. Above 11GHz, the focus splits into two lateral focused regions, as it was described before, and the lens loses the capacity to generate a single focused zone at the vertical axis.

Finally, Figure II.3.20.b shows the variation with frequency of the focusing efficiency and the radiation efficiency. The focusing efficiency has been computed from the focal width for each principal transverse plane (η^x_{FOC},η^y_{FOC}) as described in [98]. The theoretical radiation efficiency η_{RAD} has been calculated directly from the leaky-wave leakage distribution (neglecting ohmic losses) as:

$$\eta_{RAD}(f) = 1 - e^{-2\int\limits_{\rho=0}^{\rho=R} \alpha(\rho,f)\cdot d\rho} \tag{II.3.8}$$

A good agreement is observed in these curves of Figure (II.3.20), showing the pertinence of the leaky wave theory to design holographic antennas.

This chapter has shown that the holographic concept can be implemented using the LWAs. Particularly a continuous double slot Archimedean spiral has been successfully designed and measured showing a good agreement wit the predicted theory. The method described in Chapter II.2 has been used here to focus in the near-field with circular polarization and can be extended to other polarization as it will be shown in the next Chapter.

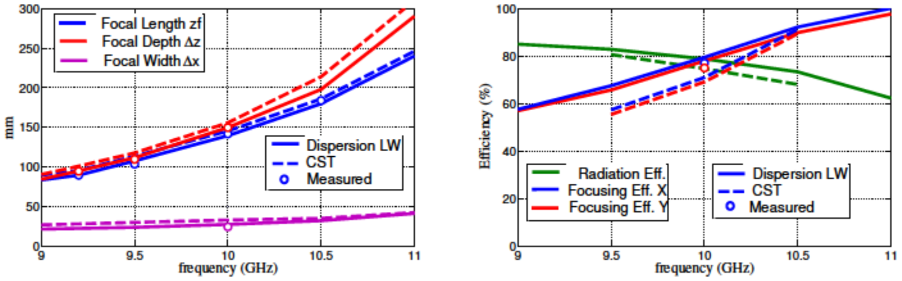

(a) (b)

Fig. II.3.20 (a). Variation of focal length, depth and width with frequency and (b). variation of focusing and radiation efficiencies with frequency.

Chapter II.4

Radially Polarized Slot LWA

Microwave three dimensional near-field focusing with radial polarization using a holographic annular-slot antenna is demonstrated in this Chapter. This radial polarization can generate axially-polarized focused fields in the near-field regime, which complements the more conventional synthesis of transversally-polarized near-field focusing patterns. Moreover, it is shown that more symmetrical focal region is obtained thanks to the radial polarization for similar Fresnel number N and operation frequency.

Introduction

As it has already been mentioned, 3D near-field microwave focusing is an interesting technique for microwave imaging, sensing and heating [99]. In these applications, the spatial resolution is determined by the spot size in both transverse and axial dimensions (see Figure II.4.1). Several microwave phased-array antennas have been proposed [66, 67, 76, 100] to synthesize near-field focused patterns with reduced spot width and depth. All these focused apertures present a $3dB$ focal depth Δz which is notably higher than the focal width $\Delta\rho$ ($\Delta z > 2\Delta\rho$, [61, 66, 67, 76, 98, 100]) due to the electrically-small dimensions involved in the microwave regime if compared to optical devices. As a result, the focused spot is not symmetrical which may be a problem in some applications.

In [101] the strong dependence of the $3D$ intensity distribution near the focus with the Fresnel number N and the displacement of the focus (i.e. focal shift) towards the aperture for low Fresnel Number is studied. In the microwave range most of the 3D-focusing planar antennas use transverse polarization [66, 67, 76, 100] (parallel to the aperture, see Figure

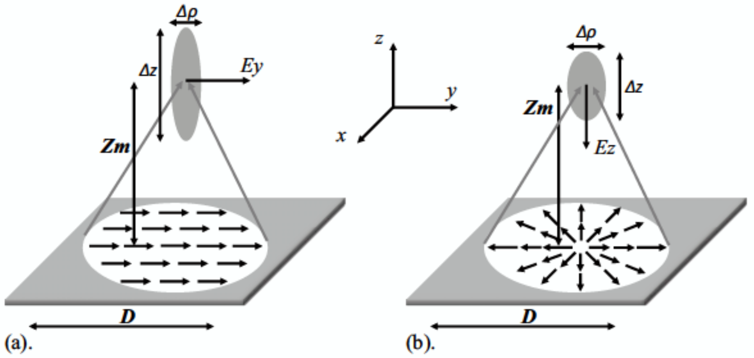

Fig. II.4.1 Near-field focused aperture with (a). transverse and (b). radial polarization.

II.4.1a). Recently the use of planar slot based antennas for axially-polarized near-fields has been proposed [102]-[103]. In [103] a planar RSLA was used to synthesize these fields with a full-wave MoM based approach. The focus was the study of the E_z component only. In this Chapter, we compare the properties of microwave planar antennas focalizing in near-field with axial and transverse polarizations for different Fresnel numbers and focal heights Zm in terms of focal width and depth considering all the components of the field. The theory is then validated with the experimental verification of an annular-slot leaky-wave antenna. This antenna consists of concentric ring slots fed by a coaxial cable and is designed based on the methodology presented in the previous chapters.

II.4.1 Near-field focusing with radial and transverse polarizations

In the microwave range, typical focal numbers are large ($Zm/D > 0.5$ for all the designs in [66, 67, 76, 98, 100] where Zm is the focal length and D is the aperture diameter), due to the limited aperture sizes $D < 10\lambda$ and relatively large focusing distances Zm. Moreover, the involved Fresnel numbers $N = D^2/(4\lambda Zm)$ are also quite low for the same reasons, so the related equations to approximately calculate the half-power focal width $\Delta\rho$ and depth Δz that are valid for $N > 5$ [61, 62], become inaccurate. As a result, most of the previously reported microwave focused apertures show a focal depth which is notably larger than the focal width, and scalar-diffraction can not be used to estimate the focus size. Actually, the polarization of the focused fields plays an important role in the determination of the focal depth, as it is demonstrated next and was already reported in the optical regime for large

N numbers [46]-[101]. However, for very low *N* numbers as the ones normally used in the microwave regime, it is shown that the polarization plays a fundamental role which can help to obtain a more symmetrical focused spot.

The following two equations represent electric field distributions over a focused aperture, being eq II.4.1 linearly polarized (along y, see Figure II.4.1.a) as in [66, 67, 76, 98, 100], whilst eq II.4.2 is radially polarized (along ρ, see Figure II.4.1.b).

$$\vec{E}_a(\vec{r'}) = circ(\rho)e^{j\sqrt{\rho^2+F^2}}\hat{y} \tag{II.4.1}$$

$$\vec{E}_a(\vec{r'}) = circ(\rho)e^{j\sqrt{\rho^2+F^2}}\hat{\rho} \tag{II.4.2}$$

Where the term $e^{j\sqrt{\rho^2+F^2}}$ is associated to the quadratic phase with ρ as a radial distance and $circ(\rho)$ represents the circular function with radial distance ρ.

As it can be seen, the y-polarized aperture fields (see Figure II.4.1.a) create near-field focused fields which are transversally polarized (parallel to the aperture, see Figure II.4.1.a). On the other hand, the ρ-polarized aperture fields create axially-polarized focused fields (z-directed, perpendicular to the aperture) with null transverse components along the lens axis, as shown in Figure II.4.1.b.

We begin this study by comparing the characteristics of the near-field patterns created by apertures with identical size and identical focusing distance *Zm*, for the two polarizations described in Figure II.4.1. The comparison is based on theoretical calculations of the near-fields calculated by doing a full wave integration of the aperture field by means of the Green's function in order to compute accurately the near-field (as it was described in Section II.2.2). It is important to point out that we are comparing apertures with same Fresnel number *N* which means identical diameter *D* and identical focal height *Zm* but different phase distributions (*F*) and a higher focal shift [62] between the theoretical focal point *F* and the maximum of intensity *Zm* is observed for the radial polarization. This difference can be readily attributed to the stronger decrease suffered by the radially-polarized near-fields as the observation point moves further from the focused aperture. Eventually, the antenna can not present axial polarization in the far field, while the transversally polarized fields can propagate through infinite. The focal depth Δz and focal width $\Delta\rho$ relative to the focal width obtained for an aperture with radial polarization is represented in Figure II.4.2.a whilst Figure II.4.2.b shows the same parameters for an aperture with transverse polarization. In both cases these parameters are represented as a function of the Fresnel number (for $2 \leq N \leq 10$) for different heights of the maximum field intensity, namely, $Zm = 2\lambda, 3\lambda, 4\lambda, 6\lambda$, always considering the total field intensity. In order to compare cases with the same focal height we need to modify the theoretical focal length F used in equations II.4.1, II.4.2 to correct the focal shift.

From these figures we can conclude that perfectly symmetrical focal regions ($\Delta\rho/\Delta z = 1$) can only be obtained for radial-polarization at low Fresnel numbers (i.e. $N = 2, Zm = 2, D = 4\lambda$) and it is also clear that the focal region created by the axial polarization is always more symmetrical than the one created by the transverse polarization. This is mainly due to the fact that the focal width of the transverse polarization is much smaller than that of the radial polarization. Also, the global resolution increases with small focusing distances Zm for both polarizations being more affected by this variation the focal depth Δz than the focal width $\Delta\rho$.

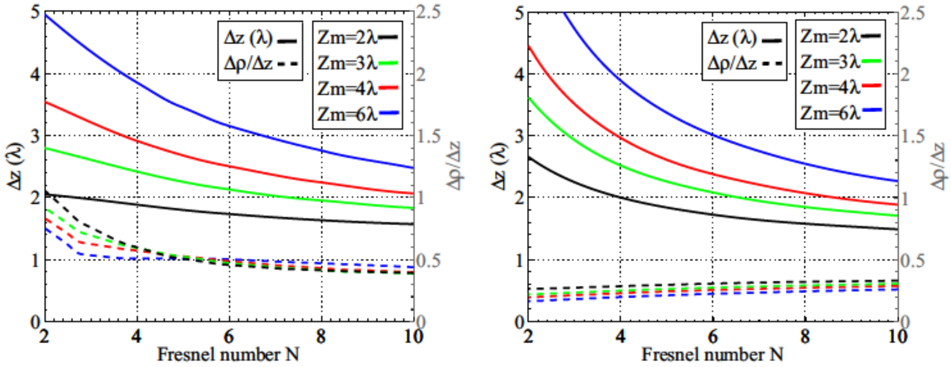

(a)

(b)

Fig. II.4.2 Near-field focused aperture with (a). radial polarization and (b). transverse polarization: half power beamwidth HPBW for the focal depth Δz and relative focal width $\Delta\rho/\Delta z$ as a function of Fresnel number N when $2 <= N <= 10$ for different focal heights Zm.

Considering now a particular example with aperture diameter D=$6\lambda_0$ and Fresnel number N=4 (i.e. $Zm \approx 2.21\lambda$), the near-field 2D-plot (xz plane) for a radially-polarized aperture is presented in Figure II.4.3a, which illustrates a 3dB spot size $\Delta z \times \Delta\rho$ of $2.02\lambda \times 1.28\lambda$ ($\Delta\rho/\Delta z = 0.63$, results in other planes are similar due to azimuthal symmetry). Figure II.4.3.b shows the same results for the transversally-polarized counterpart antenna, demonstrating the more unbalanced elliptic shape with higher focal depth and reduced focal width for the obtained spot (3dB spot size of $2.46\lambda \times 0.61\lambda$, $\Delta\rho/\Delta z = 0.25$) for the same aperture diameter and Fresnel number. The radial polarization produces a more symmetrical 3D focused spot if compared to a transversally-polarized focused region (considering all the field

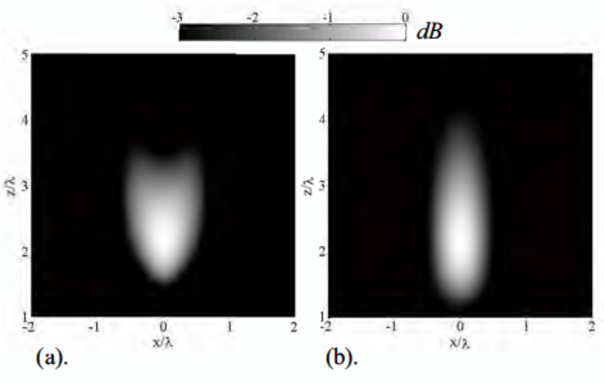

(a). (b).

Fig. II.4.3 Theoretical 3D focused spot for (a). radially and (b). transversally-polarized lens.

components).

Finally we show the different components of the radiated field in the transversal cut for an aperture with radial and transverse polarization to better understand how these apertures radiate. An example for N=4 and several focal lengths Zm with radial polarization is represented in Figure II.4.4.a. The field is represented in a transverse plane at the focal height Zm. We can see how the axial component becomes weaker than the transverse component when the focal height increases as expected. If we compare with a transverse polarized case (see Figure II.4.4.b), here the field is mainly transverse and the axial component is very weak for all heights Zm. The field intensity E_x is larger for the transverse than the E_z in the axial polarization, even when the focal width and depth are smaller for axial polarization. The reason is that the field intensity along x for points outside the z-axis is high for the radial polarized antenna.

All the presented results correspond to theoretical results calculated by using a home-made code to compute the theoretical solutions. These results will be validated with experiments at the 10GHz band in the following section.

II.4.2 Prototype and Experimental Results

The holographic printed-slot technique proposed in this thesis for the synthesis of near-field focusing patterns is used to design a focused antenna with D=6λ_0, F=3λ_0 and N=4 operating at 10GHz. In this design we have used an aperture amplitude function $A(\rho) = cos(\pi\rho/(3.5R))^2$ with radiation efficiency of $\eta = 85\%$, which provides quasi-uniform illu-

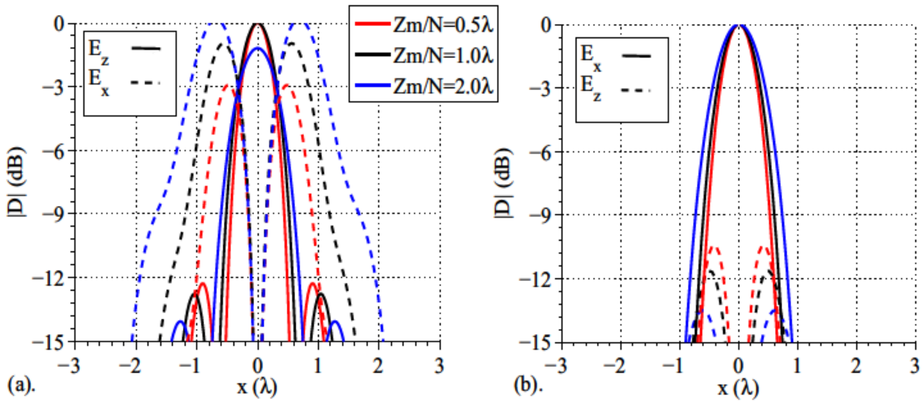

Fig. II.4.4 Radiated fields as a function of the ratio Zm/N for both (a). radial and (b). transverse polarization.

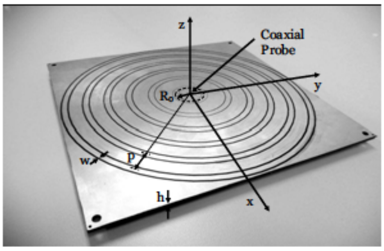

Fig. II.4.5 Fabricated annular-slot holographic antenna with radial polarization.

mination. Instead of using spiral slots which provide transverse circular polarization, here we propose the use of an annular slot configuration as shown in Figure II.4.5 to obtain radial polarization. This shape resembles the annular slot antenna [96] which was formed by a discrete number of crossed slots for each annulus to obtain arbitrary transverse polarization of the far-field focused radiation pattern. More recently, a similar geometry to the annular slot antenna has been proposed to demonstrate the capacity to shape an axially polarized near-field focus at 12.5GHz with N=6.25 [103]. We would like also to report here the ability to obtain a more symmetrical focus in the microwave regime thanks to the use of the radial polarization and low Fresnel number designs. The use of resonant slots in [103] requires a full 2D MoM design methodology, whereas the antenna proposed here is designed with a leaky wave approach in 1D. As it was explained before, the position and width of each annular slot must be appropriately modulated to synthesize the desired near-field focal point. Table II.4.7 summarizes the dimensions of the six designed rings, which are printed on commercial substrate with ε_r=2.2 and thickness h=3.175mm. Also, it must be noticed that each ring is formed by two annular slots separated at a distance $\lambda_{SW}/4$ to minimize reflections. The holographic antenna is simply fed by a vertical coaxial probe located at the center not touching the upper metal.

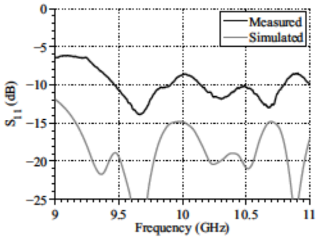

Fig. II.4.6 Reflection coefficient.

Param	ρ (mm)	w (mm)
Ring 1	12.33	0.20
Ring 2	32.68	0.50
Ring 3	51.03	0.80
Ring 4	68.45	0.95
Ring 5	84.98	1.10
Ring 6	100.80	1.25

Fig. II.4.7 Designed annular slot position and widths.

Figure II.4.6 shows the measured reflection coefficient and its comparison with simulated results obtained with full wave simulations (CST MWS [95]). In simulations, the antenna is well-matched over a 20% frequency band, whilst the measured results exhibit a worse matching probably due to inaccuracies in the location of the blind feeding connector with the required precision. To measure the near-field, we have used an optimized probe with 6mm length made from a coaxial cable with diameter 5mm, both small in terms of the wavelength. The step for sampling is fixed to 10mm. The measured near-field distribution along the lens axis is plotted in Figure II.4.8.a, demonstrating the synthesis of pure axially-polarized E_z focused near-fields at the design frequency of 10GHz. The theoretical results are also represented in the same graph, showing very good agreement with theory.

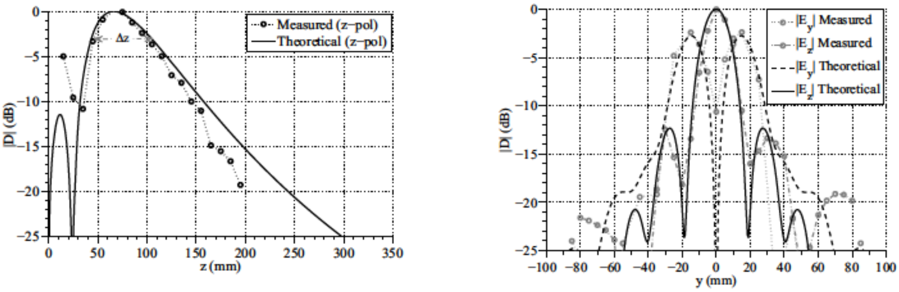

(a) (b)

Fig. II.4.8 (a). Experimental validation of near-field focusing of radially polarized fields at 10GHz for N=4. (b). measured and theoretical transverse distribution of near-field at 10GHz.

Measured near-field distribution along the transverse cut ($\phi = 90deg$, y axis) at its maximum intensity height of z=65mm=2.17λ_0 is depicted in FigureII.4.8.b. The used probe is a coaxial probe and more details about the scheme of the near-field measurement set-up are shown in the previous Chapter. Here again the simulated and measured results are in very good agreement both for the main axial polarization E_z as well as for the side lobes of the cross transverse polarization E_y. In this plane it has been confirmed that the E_x component is zero due to the azimuthal symmetry of the designed antenna. On the other hand, the two sidelobes with cross-polarized component (E_y) appear at a level of -2.5dB with respect to the main E_z lobe, and at an approximate radial distance of $\pm 15mm = \lambda/2$. It must be said that this pattern with focused spatial polarization diversity might find interesting applications for sensing. The central beam can sense the radially polarized field at the lens axis, while the sidelobes can sense the radially polarized field at both sides of the axis.

This chapter has shown that the method described in Chapter II.2 can also be used to design holographic antennas with radially polarized near-field. A double-slot-ring LWA has been successfully designed and measured showing good agreement with the predicted theory.

Chapter II.5

Concluding Remarks

In this first part of the thesis, it has been theoretically demonstrated the ability to design a holographic two-dimensional planar microwave lens, by modulating the position and width of a printed-slot circuit. The design is based on the tapering of a cylindrical leaky wave, pursuing the main objective of controlling the amplitude and phase of its radiated fields. An aperture-driven synthesis technique based on the geometrical dispersion of the LW, which is particularly suited for large apertures, has been presented. The important application of the proposed design technique is that it allows the direct tapering of both the leakage angle and the leakage rate of the radiating leaky mode.

As a first example, a quadratic-phase, quasi-uniform amplitude, circularly-polarized aperture has been designed at 10GHz. The proposed holographic lens uses a continuous spiral-modulated printed slot-circuit with radial separation in the order of half wavelength. This is a much simpler structure than the previously proposed holographic antennas based on subwavelength unit-cells, [50],[31] or *RLSA* designs based on discrete resonant slots [96]-[32], which need hundreds of radiating elements to generate the holographic pattern (thus resulting in tighter fabrication tolerances and advanced design and optimization procedures [80]). The focusing patterns predicted by this theory have been compared with full-wave simulations showing very good agreement. This validates the hypothesis that a single modulated leaky wave is dominating the near-field, even for such a small aperture. Experimental results in the $10GHz$ band confirm the working mechanism of a novel type of microwave lens based on modulated leaky-wave concepts and simple integrated feeding mechanisms. Its main drawback, however, resides in its poor circular polarization performance due to the use of a continuous slit. Moreover, it has been explained and demonstrated the interesting effect of frequency steering of the focal length, which allows electronically adjustment of the focus position in a region by simply changing the frequency of the input signal. Maximum focal length is limited by the splitting of the single focus above a certain frequency. This is a general behavior for any holographic near-field lens, due to the dispersive nature of the modulated leaky wave.

As second example a complete study of apertures which focalize in the near field with linear radial polarization has been presented. Compared to previous designs with transversally polarized focused near-fields, the presented antennas have a more symmetrical focal region and this characteristic improves when the Fresnel number N is low. The study shows that the improvement in the symmetry of the focus spot with the radial polarization is achieved thanks to a decrease in the focal depth and an increase in the focal width. The focal depth of the antenna with radial polarization is slightly smaller than that of an antenna with transverse polarization and it depends on the focal distance Zm. The focal width is significantly greater in the radially polarized lens than in the transversally polarized. The combination of these two results provides us with field distributions which are much more symmetrical as well as having components with perpendicular directions and same intensity which could offer a spatial diversity in certain types of imaging applications. Another important characteristic is that the intensity of the radiation of the cross-polar component E_x in the radial lens can be controlled by means of the ratio Zm/N.

A prototype (for each polarization: circular and radially polarized antenna) operating at $10GHz$ with an aperture diameter $D = 6\lambda$ and implemented as a holographic leaky-wave antenna, has been manufactured and measured, confirming the theory developed along this first Part of the thesis.

Part III

LW Phased Arrays for Telecommunication Applications

Chapter III.1

Introduction

In Earth and planetary coverage applications where high gain is required, it is common to use large phased array antennas that can steer the beam over the coverage area. In many occasions the necessary steering angle is in the order of few degrees, i.e. $10deg$ - $15deg$. For such applications, it is possible to reduce the cost in number of active transceivers by having phased arrays designed with large periods (larger than a wavelength), i.e. thinned arrays. The drawback of such an approach is that it will introduce grating lobes in the visible range, and this would constitute a loss of both power and directivity. In order to avoid this loss, solutions from the use of aperiodic arrays or sparse arrays synthesized with optimization strategies [104] to the use of feeding techniques at the level of subarrays [105]-[106] to mitigate grating lobes are proposed. Some authors have proposed the use of tapering amplitudes in the subarrays combined with the addition of some random aspects in the design [107]. A different approach, first proposed in [108], is the use of (dielectric) super-layers as a means of spatial filters to control the grating and side lobes in phased arrays made of horns. In [109] the super-layers were designed as Chebyshev's filters and the concept was experimentally verified in [110]. Fabry-Perot cavity's (FPC) or leaky wave antennas (LWAs) use dielectric or metallic super-layers to increase the directivity by placing a partially reflecting surface (PRS) in front of an antenna with a ground plane [5, 111]. Leaky wave modes can propagate along the resonant cavity created between the PRS and ground plane altering the far-field of the feed antenna and increasing the effective area of the antenna [111]. The PRS can be made of a dielectric super-layer [109] or a Frequency Selective Surface (FSS) [5]. When a FPC is used in an array, the leaky waves lead to antennas having overlapping areas. Thanks to this effect, it has been demonstrated that such arrays can improve the edge of coverage gain in multibeam space applications [43]. Indeed this solution has the potential to provide enhanced performances over more standard solutions based on subarrays or large directive elements such as conical horns. The use of this type of antennas has also been recently proposed to improve the gain in thinned arrays [11, 26]. Most of these works study the enhancement of directivity at broadside for small arrays.

In this second part of the thesis, we firstly demonstrate that inductive strip grid based MTS leads to higher directivity enhancement for LWAs thanks to the intrinsic suppression of the TM_0 leaky wave mode while maintaining the same frequency bandwidth. A similar effect has been observed in grounded metamaterial dielectrics made of patches, where the TM_0 surface wave is not increased with respect to the hosting dielectric [112]. In order to investigate the impact of this mode, the three configurations (dielectric superstrate, inductive FSS, and capacitive FSS) have been designed in order to have the same TE_1/TM_1 mode wavenumber. LWAs with equivalent TE_1/TM_1 modes will lead to the same levels of mutual coupling, since this is dominated by these leaky waves [113]. Experiments are reported to verify these important results in a waveguide antenna.

Secondly in this part and in order to extend the LWAs to phased array, we investigate the impact of the mutual coupling when such leaky wave antennas are used to improve the performances of poorly sampled phased arrays with a limited scanning range. The impact of the mutual coupling on the embedded patterns has been previously studied in [38] for multibeam applications. Here we extend this study to phased arrays including the impact on the active impedance. The reduction of the grating lobes in the thinned array radiation pattern depends on the dielectric superlayer constant. The larger the dielectric constant, the higher the attenuation of the grating lobe will be. However, this can only be obtained at the cost of an increased mutual coupling. We show that antenna elements based on dielectric superlayers leading to mutual coupling levels larger than -20dB suffer from a loss of directivity in the embedded pattern and a loss of gain in the phased array because of the highly resonant active impedance. We also present a practical implementation of a leaky wave thinned phased array with enhanced scanning properties. Our study demonstrates that a reduction of the grating lobes and a improved gain of the sparse array radiation pattern are possible thanks to the angular filtering introduced by a Fabry-Perot cavity. The presented array is made in PCB and integrated with an inductive FSS super-layer. A full study of the performances of the 7x7 phased array antenna for several scanning angles is presented and compared with a reference solution based on 2x2 sub-arrays. This study shows the improved gain, directivity, grating lobe level, side lobe level, front to back ratio and beam efficiency as a function of the frequency for the leaky wave enhanced phased array.

At the end if this part we show that the LWAs can also be used to synthesize isoflux patterns of specially interest in satellite applications. The drawback in this preliminar study was to point at large angles, trying to do the isoflux mask of a phased array with a LWA. To solve this issue a substrate different to air had to be used in the Fabry-Perot cavity. Unfortunately, this allows the propagation of surfaces waves (SW) inside the cavity. Several practical design are presented focusing on the suppression of the surfaces waves.

Chapter III.2

On a rigourous comparison between dielectric and MTS based LWAs

Fabry-Perot antennas (FPA) achieve high broadside directivity thanks to the simultaneous excitation of a pair of nearly degenerate TE/TM leaky-wave modes using a partially-reflecting surface on top of a ground plane. This partially-reflecting surface can be obtained using a dielectric superstrate or via a capacitive or inductive metasurface (MTS). By using an equivalence between the conventional dielectric superstrate and the MTS-based structures in terms of the dominant TE/TM modes, we show that the use of inductive grid MTSs leads to a directivity enhancement. A higher roll-of in the radiation patterns is achieved thanks to the intrinsic suppression of the spurious TM_0 leaky wave mode. This suppression is mathematically demonstrated and validated with full-wave simulations.

Introduction

The use of partially reflecting surfaces on top of a ground plane to enhance the directivity of small antennas has been considerably studied in literature [5–15]. This type of antennas are typically referred as Leaky Wave Antennas (LWAs) [6–9], Electromagnetic Band-Gap (EBG) antennas [11], Fabry-Perot Antennas (FPA) [12] and even resonant cavity antennas [15]. Hereinafter, we will refer to these antennas as LWAs. LWAs make use of a partially transmissive resonant structure [6] which can be made of a thin dielectric superstrate [6, 13, 14] or by using inductive- or capacitive-Metasurfaces (MTS) [8–12, 14, 15, 73, 114, 115]. Figure III.2.1 shows three examples of these topologies placed on top of a waveguide opening. Recently, LWAs have gained interest for future Ka-band telecommunication satellites due to their potential to create overlapping radiating areas in focal plane arrays with a single feed per beam [24, 25]. Telecommunication space industries are currently interested in developing future thinned arrays with limited scanning ranges for the Ku-band. Besides other possible approaches based on sub-arrays, there is the interest to investigate the potential of LWAs for this application since they would lead to directive array elements even if the array periodicity is large [26]. Future telecommunication thinned arrays will operate with spacing of $2\lambda_0$ and a relative frequency bandwidth of 1.7% at Ku-band (14.25-14.5GHz) with a maximum scanning angle of $8.6deg$. This scenario would require a dielectric superlayer with ε_r=10 (this will be detailed in following chapters). In this Chapter, we investigate which partially reflecting surface, dielectric superstrate or MTS is the most appropriate for this scenario.

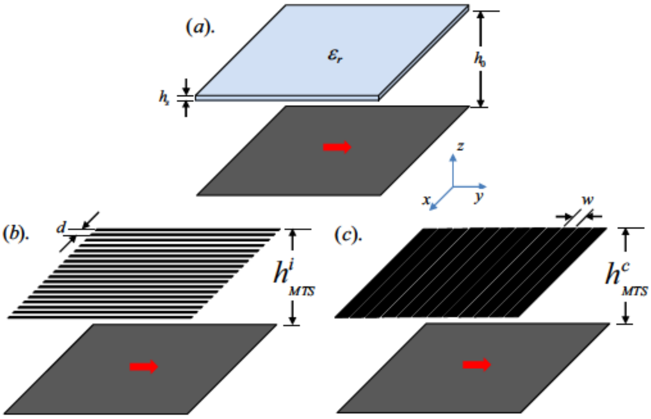

Fig. III.2.1 LW waveguide antenna using (a). a dielectric superstrate with permittivity ε_r, (b). an inductive strip grid based MTS and (c). a capacitive slot grid based MTS. The periodicity of the MTS is d, whereas w indicates the strip width. We refer to capacitive MTS when the strips are aligned to the H-plane and to inductive MTS when the strips are aligned to the E-plane.

The physical phenomenon exploited, in this type of antennas, to achieve high directivity from a point source is the excitation of a pair of nearly degenerated TE_1/TM_1 leaky wave modes. These modes propagate in the resonant region by means of subcritical multiple reflections between the ground plane and the superstrate/MTS, while partially leaking energy in free space. The amount of energy radiated at each reflection is related to the LW attenuation constant and can be controlled by the MTS sheet-impedance or the dielectric constant. For a detuned structure at frequency above the resonant frequency, the far-field radiation pattern exhibits conical shape which eventually degenerates in a pencil beam at the frequency where the real part and imaginary part of the complex leaky wave wavenumber are equal. This occurs almost at the same frequency for both a TE_1 and a TM_1 mode. For the dielectric superlayer, the maximum directivity at broadside is achieved at the resonant condition, i.e. the thickness of the resonant cavity is $h_0 = \lambda_0/2$, and that of the superlayer is $h_s = \lambda_0/4\sqrt{\varepsilon_r}$, [6]. Under this condition, the couple of TE/TM leaky wave modes can propagate with the same phase velocity, creating a nearly uniform phase distribution in the aperture. It has been seen that the generated aperture field is also very well polarized, due to a compensation effect between the TE and TM modal tangential field components [16]. However, this type of LWA also generates an undesired spurious TM_0 leaky-wave mode, conceptually associated with the TEM mode of the perfectly conducting walls parallel plate waveguide [27]. This mode radiates near the Brewster angle creating spurious lobes in the E-plane reducing the beam efficiency. In this paper, we show that inductive strip grid based MTS leads to higher directivity enhancement in equivalent LWAs thanks to the suppression of this TM_0 leaky wave mode while maintaining the same frequency bandwidth. In an inductive strip grid based MTS, this TM_0 leaky wave mode is transformed into a surface wave (SW), whereas the capacitive slot grid based MTS and dielectric superstrate do support the leaky wave mode. The effect of this mode can be attenuated by using a double slot feed [27, 116]. Even when this slot feed is used, the strip grid based MTS leads to the highest directivity for the same frequency bandwidth. Other type of MTSs, such as artificial dielectrics made of patches [112], do not alter the TM_0 mode of the hosting stratification, however they lead to lower directivity enhancement because they introduce asymmetries in the propagation constants of the main TE/TM modes [117].

For array applications, it is important to maximize the directivity of the LWA at the largest possible bandwidth and keeping the mutual coupling levels in the order of -20dB, both (directivity and mutual coupling), are proportional to the TE_1/TM_1 mode wavenumber [27, 118].

III.2.1 On the Equivalence between LWAs

In this section, a theoretical comparison with the three types of LWA shown in Figure III.2.1 is presented. For this purpose, we will investigate how the PRS structures alter the radiation from an elementary magnetic source on an infinite ground plane. A dielectric superlayer or MTS will be located on top of the ground plane at a certain height, h_0 or h_{MTS}, respectively. The dielectric superlayer is characterized by a dielectric constant ε_r and thickness h_s. The MTS will be made of metal strips of width w and periodicity d (fixed to $\lambda_0/4$ in this paper) for simplicity in their analysis since there is an analytical closed form expression for their reactance [119, 120]. This also means that the main parameter determining the properties of these LWAs is the complex transverse propagation constant k_ρ, of the TE_1 and TM_1 modes. Considering LWAs designed for broadside directivity enhancement, a smaller propagation constant (real and imaginary parts) implies higher directivity, but also smaller bandwidth and higher mutual coupling between two closed antennas placed under the same partially reflecting surface. The maximum power density at broadside for a small propagation constant occurs when $\alpha = \beta$ [117]. Therefore, when comparing different LWA configurations, an equivalence should be set by equalizing the corresponding TE_1/TM_1 propagation constants.

Equivalent TE_1/TM_1 modes

The leaky wave propagation constants are the solutions of the dispersion equation associated with the equivalent TE and TM transmission lines [13]. For the geometries under investigation here, the equivalent transmission lines are shown in Figure III.2.2. When the periodicity of the MTS is small compared to the wavelength, their electromagnetic properties can be represented by a purely imaginary shunt impedance $Z_{TE/TM}^{MTS}$ [49]. We report the closed form expression for the impedances of the capacitive slot grid and inductive strip grid based MTS [119] since it would be necessary to derive analytical solutions of the dispersion equation:

$$\begin{aligned}
Z_{TM}^{MTSi} &= jX_0(1-k_\rho^2/k_0^2) && \text{(III.2.1)}\\
Z_{TE}^{MTSi} &= jX_0 && \text{(III.2.2)}\\
Z_{TM}^{MTSc} &= -jX_0 && \text{(III.2.3)}\\
Z_{TE}^{MTSc} &= -jX_0(1-k_\rho^2/k_0^2)^{-1} && \text{(III.2.4)}
\end{aligned}$$

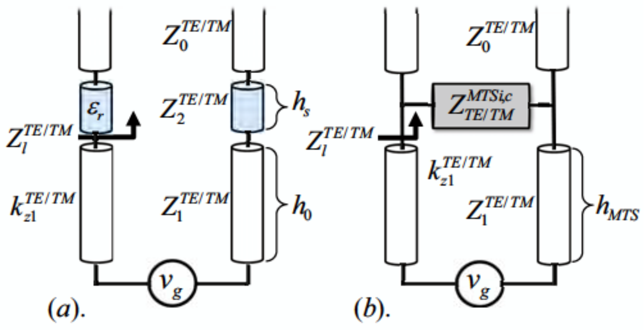

Fig. III.2.2 Equivalent transmission line for (a). dielectric super-layer and (b). equivalent MTS.

Where $X_0 = \frac{\eta_0 k_0 d}{2\pi} \ln|\frac{2d}{\pi w}|$ for $d \leq \lambda_0/4$ and η_0 is the free space wave impedance.

The dispersion equation associated to these equivalent transmission lines is the following:

$$D^{TE/TM}(k_p) = Z_l + jZ_1 tan(k_{z1}h_1) = 0 \tag{III.2.5}$$

Where $Z_l = Z_2 \frac{Z_0 + jZ_2 tan(k_{z2}h_2)}{Z_2 + jZ_0 tan(k_{z2}h_2)}$ for the dielectric case and $Z_l = \frac{Z_{MTS}^{i,c} Z_0}{Z_{MTS}^{i,c} + Z_0}$ for the MTS. Z_0, Z_i represent the TE or TM impedances ($Z_i^{TE} = \frac{\eta_0 k_0}{k_{zi}}$ and $Z_i^{TM} = \frac{\eta_0 k_{zi}}{k_0}$), h_1=h_0 or $h_{MTS}^{i,c}$ and $k_{zi} = \sqrt{\varepsilon_{ri} k_0^2 - k_\rho^2}$.

Therefore, the leaky wave propagation constant greatly depends on the load impedance, Z_l at the top of the cavity as shown in Figure III.2.2. The dispersion equation, once the geometry is known, can be solved numerically to find the leaky wave propagation constants. However, for design purposes, it is more convenient to have analytical approximate formulas to compute these constants. These formulas can be used to impose that equivalent LWAs have the TE_1/TM_1 with the same propagation constants as proposed in [2], as well as to demonstrate that only the inductive strip grid based MTSs do not support the TM_0 leaky mode, independently of the geometrical parameters. In [13], a methodology to derive these formulas for the TE_1/TM_1 modes was proposed for dielectric based LWA and extended in [2] to MTS based LWA. The fundamental step was recognizing that the tangent function $tan(x)$ can be linearly approximated around its zeroes for arguments in the neighborhood of $x \pm \pi$. Using this approximation the dispersion equation will be:

$$k_{z1} = j\frac{Z_l}{hZ_1} + \frac{n\pi}{h} \tag{III.2.6}$$

Note that when the cavity load impedance Z_l is equal to zero, this equation gives the propagation constants of the modes in a parallel plate waveguide (PPW) of thickness h. In order to make this equation analytical for the $n = 1$ in the TE and TM modes, the load impedance Z_l can be approximated by its value around broadside, therefore $Z_l = \frac{\eta_0}{\varepsilon_r}$ for the dielectric superstrate or $Z_l = \frac{\eta_0 Z^{i,c}_{MTS}(\theta=0)}{\eta_0 + Z^{i,c}_{MTS}(\theta=0)}$ for the MTS. By substituting these approximations into eq III.2.6, one arrives to compact formulas for the TE_1/TM_1 modes of LWAs [2, 13]. Then by equalizing both real and imaginary parts of the propagation constants, one can derive expressions for the MTS impedance and cavity height as a function of the parameters of the equivalent dielectric based LWA [2]. The expressions are reported here for convenience:

$$Z^{i,c}_{MTS} = j\eta_0 \left(\frac{-1 \pm \sqrt{1 + 4\pi^2(\varepsilon_r - 1)}}{2\pi(\varepsilon_r - 1)} \right) \tag{III.2.7}$$

$$h^{i,c}_{MTS} = h_0 \frac{\varepsilon_r |Z^{i,c}_{MTS}|^2}{\eta_0^2 + |Z^{i,c}_{MTS}|^2} \tag{III.2.8}$$

Figures III.2.3 and III.2.4 show the TE_1 and TM_1 dispersion diagrams for the three equivalent geometries under investigation, i.e., dielectric superstrate (blue line), inductive strip grid based MTS (red line) and capacitive slot grid based MTS (black line). All curves are calculated for equivalent superstrate permittivity $\varepsilon_r = 4$ (continuous line) and $\varepsilon_r = 10$ (dashed line). The equivalent inductive strip grid based MTS has $Z^i_{MTS} = 119i\Omega$ and must be located at a height of $h^i_{MTS} = 0.9h_0$ whilst the capacitive slot grid based MTS has $Z^c_{MTS} = -132i\Omega$ and needs to be placed at a height of h^c_{MTS}=$1.10h_0$ for ε_r =10 whilst $Z^i_{MTS} = 199i\Omega$, $h^i_{MTS} = 0.87h_0$, $Z^c_{MTS} = -238i\Omega$ and h^c_{MTS}=$1.14h_0$ for ε_r =4, being $h_0 = \frac{\lambda_0}{2}$. It can be observed that the equivalent geometries present comparable solutions of the dispersion equation around the operating frequency (f/f_0=1) at which maximum broadside radiation occurs. A larger discrepancy is observed for lower dielectric constants since the approximate analytical formulas lose accuracy for lower contrast as pointed out in [13]. Table III.2.1 gives the numerical solutions of the dispersion equation of the three equivalent LWAs for ε_r=10 at the central frequency.

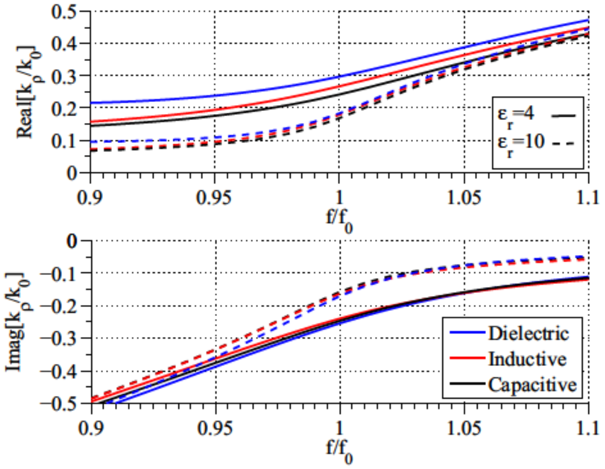

Fig. III.2.3 TE_1 mode solution of the dispersion equation with $\varepsilon_r = 4$ (continuous lines) and $\varepsilon_r = 10$ (dashed lines) for three equivalent cases: dielectric superstrate (blue), inductive strip grid based MTS (red) and capacitive slot grid based MTS (black).

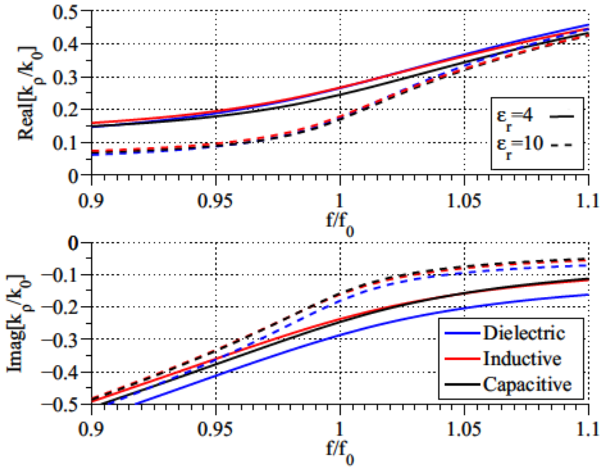

Fig. III.2.4 TM_1 mode solution of the dispersion equation with $\varepsilon_r = 4$ (continuous lines) and $\varepsilon_r = 10$ (dashed lines) for three equivalent cases: dielectric superstrate (blue), inductive strip grid based MTS (red) and capacitive slot grid based MTS (black).

Analytical Dispersion Equation Solution for the TM_0 mode

Following similar steps, a formula can also be obtained for the n=0 TM mode. In this case, the TM dispersion equation becomes:

$$Z_l + j\frac{\eta_0 k_{z1}^2}{h_1 k_0} = 0 \tag{III.2.9}$$

k_ρ/k_0	Dielectric	Inductive	Capacitive
TE	$0.184-j0.171$	$0.179-j0.163$	$0.169-j0.158$
TM	$0.174-j0.181$	$0.179-j0.161$	$0.169-j0.158$
TM_0	$0.972-j0.034$	$1-j0$	$0.979-j0.029$
h_{MTS}	h_0	$0.9h_0$	$1.1h_0$

Table III.2.1 Comparison of the propagation constants obtained for the equivalent MTSs and $\varepsilon_r = 10$ dielectric LWAs at central frequency.

In order to derive an analytical solution, we need to provide an approximate but accurate expression for the load impedance Z_l. We can do this by recalling that the modes in a LWA resemble those of the equivalent PPW. In a PPW, the TEM mode transverse propagation constant is $k_\rho = k_0$. Therefore, when looking for the solution of the TM$_0$ mode, we can approximate Z_l by its value around $k_\rho = k_0$. This is done in the following for three specific cases shown in Figure III.2.1.

Dielectric Superstrate

In this case, the load impedance Z_l is given by $Z_l = Z_2\frac{z_0+jz_2 tan(k_{z2}h_2)}{z_2+jz_0 tan(k_{z2}h_2)}$.

For $k_\rho = k_0$, the dielectric characteristic TM impedance becomes $z = \frac{\eta_0\sqrt{\varepsilon_r - 1}}{\varepsilon_r}$ and $Z_l \approx \frac{z_2^2}{z_0}$.

Substituting these approximations into eq III.2.9, one arrives to the following formula of the longitudinal propagation constant for the TM$_0$ mode:

$$k_{z1}^{SUP} = \sqrt[3]{jk_0^2\frac{\varepsilon_r - 1}{\varepsilon_r^2 h_0}} \tag{III.2.10}$$

LWA based MTS

For the MTS cases, the load impedance is calculated by $Z_l = \frac{Z_{MTS}^{i,c}Z_0}{Z_{MTS}^{i,c}+Z_0}$

Substituting this expression in eq III.2.9, leads to

$$\frac{Z_{TM}^{MTS}\eta_0 k_{z1}}{k_0} + j\frac{\eta_0 h_1 k_{z1}^2}{k_0}\left(Z_{TM}^{MTS} + \frac{\eta_0 k_{z1}}{z_0}\right) = 0 \tag{III.2.11}$$

Thus one solution is $k_{z1} = 0$, and other two solutions come from the following equation

$$Z_{TM}^{MTS} + jh_1 k_{z1} Z_{TM}^{MTS} + jh_1\eta_0\frac{k_{z1}^2}{z_0} = 0 \tag{III.2.12}$$

For inductive strip grid based MTS, the impedance is given by eq III.2.1, which in the E-plane can be written as

$$Z_{TM}^{MTSi} = j\frac{X_0 k_{z1}^2}{k_0^2} \tag{III.2.13}$$

This expression can be replaced in eq III.2.12, giving rise to two solutions: again $k_{z1}^{IND} = 0$ and $k_{z1}^{IND} = j\frac{h_1\eta_0 k_0 + X_0}{X_0 h_1}$. This second solution is non-physical. Therefore the only possible solution for the inductive strip grid based MTS is $k_{z1}^{IND} = 0$.

In the capacitive slot grid based MTS case, the impedance in the E-plane is the following

$$Z_{TM}^{MTSc} = -jX_0 \tag{III.2.14}$$

Replacing this expression into eq III.2.12, one arrives to the following physical solution:

$$k_{z1}^{CAP} = -j\frac{X_0 k_0}{2\eta_0}\left(1+\sqrt{1+\frac{4\eta_0}{X_0 h_1 k_0}}\right) \tag{III.2.15}$$

The final formulas are summarized now as:

$$k_{z1}^{SUP} = \sqrt[3]{jk_0^2\frac{\varepsilon_r - 1}{\varepsilon_r^2 h_0}} \tag{III.2.16}$$

$$k_{z1}^{IND} = 0 \tag{III.2.17}$$

$$k_{z1}^{CAP} = -j\frac{X_0 k_0}{2\eta_0}\left(1+\sqrt{1+\frac{4\eta_0}{k_0 X_0 h_{MTS}}}\right) \tag{III.2.18}$$

The associated transverse propagation constant can be easily calculated by using $k_\rho = \sqrt{k_0^2 - k_{z1}^2}$.

From these equations, we can see that the inductive strip grid based MTS is the only configuration which does not support a TM$_0$ leaky wave, independently of the MTS geometrical parameters. This is because, the TM$_0$ mode is mainly z-polarized and the strips are nearly transparent for this polarization. The TM$_0$ mode in this inductive MTS is transformed into a surface wave (SW) that will only alter the radiation pattern by diffraction at the edges of the structure. The impact on the radiation pattern of both a TM$_0$ leaky mode and a surface wave can be reduced by introducing a spectral null at $k_\rho = k_\rho^{TM_0}$ [27, 116]. However, the inductive MTS still leads to the highest directivity enhancement. We will see next how this implies that the radiated field generated by the inductive strip grid based MTS has a larger roll-off than the one radiated by the dielectric and capacitive based LWAs. Figures III.2.5

and III.2.6 show the exact and approximate solutions of the dispersion equation for the TM$_0$ mode for the same cases than in Figures III.2.3 and III.2.4. Once again, the accuracy of the analytical formulas is higher for higher contrast since the solution get closer to the PPW ones. The exact solution for the TM$_0$ mode is also given in Table III.2.1.

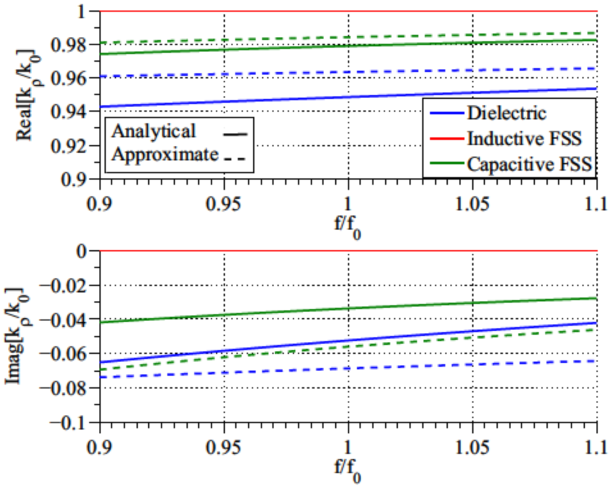

Fig. III.2.5 TM$_0$ mode of the numerical (continuous lines) and approximate (dashed lines) solution of the dispersion equation with ε_r =4 for three equivalent cases: dielectric superstrate (blue), inductive strip grid based MTS (red) and capacitive slot grid based MTS (black).

Theoretical Far-Fields

Next we investigate the radiated fields in the far-field by the three equivalent LWAs. These patterns can be obtained resorting to a rigorous spectral Green's function approach [118]. Figures III.2.7 and III.2.8 show the radiated fields for an elementary source at central frequency in E- and H-plane, respectively, for the same structures described in Figures III.2.3 and III.2.4. An important consequence of the TM$_0$ suppression is observed in the E-plane. In fact, for the dielectric case the existence of the TM$_0$ mode causes a side lobe in an angular direction close to the Brewster angle. For the capacitive slot grid based MTS, the effect of the TM$_0$ is also observed, but at a slightly larger angle. For inductive strip grid based MTS, this peak disappears, with the consequent increase of directivity.

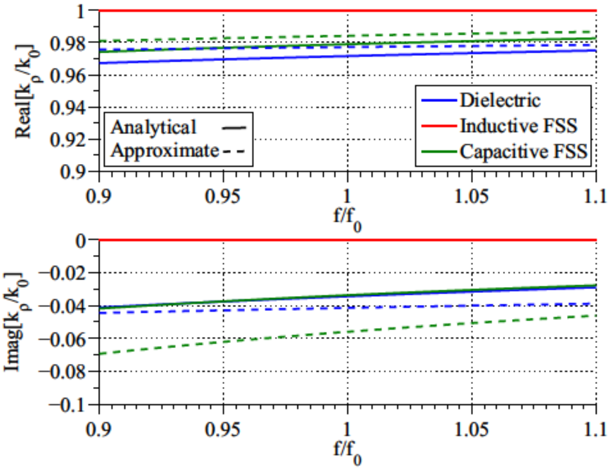

Fig. III.2.6 TM$_0$ mode of the numerical (continuous lines) and approximate (dashed lines) solution of the dispersion equation with $\varepsilon_r = 10$ for three equivalent cases: dielectric superstrate (blue), inductive strip grid based MTS (red) and capacitive slot grid based MTS (black).

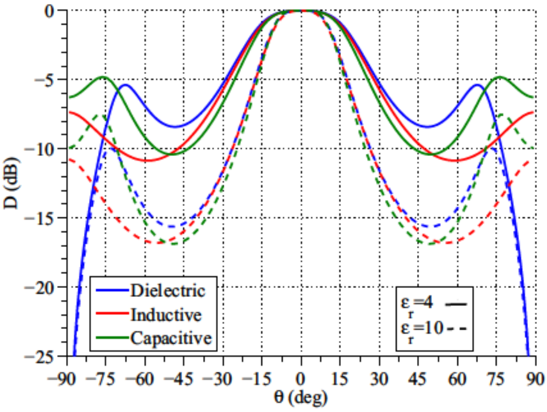

Fig. III.2.7 E-plane Comparison of theoretical radiation patterns for the equivalent structures described in Figure III.2.1 at $f = f_0$.

Figure III.2.9 shows the estimated directivity as a function of the frequency for the three equivalent LWAs for the denser contrast case of Figures III.2.7 and III.2.8. As it can be appreciated, the inductive solution improves the directivity in almost 1dB over the frequency band with respect to the dielectric solution. It is also important to notice that the calculated frequency bandwidth of the LWAs, defined here as when the directivity decays 1dB from the maximum, is the same for the three structures (the precise values are given in the figure

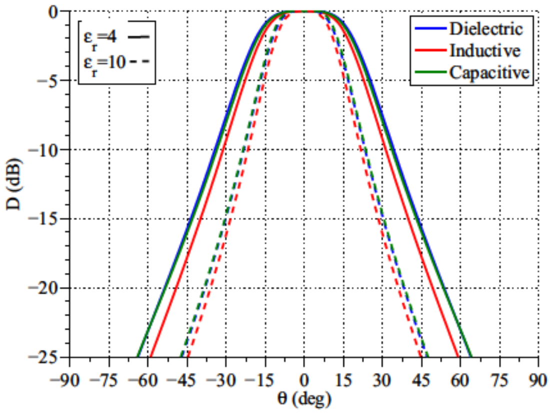

Fig. III.2.8 H-plane Comparison of theoretical radiation patterns for the equivalent structures described in Figure III.2.1 at $f = f_0$.

caption).

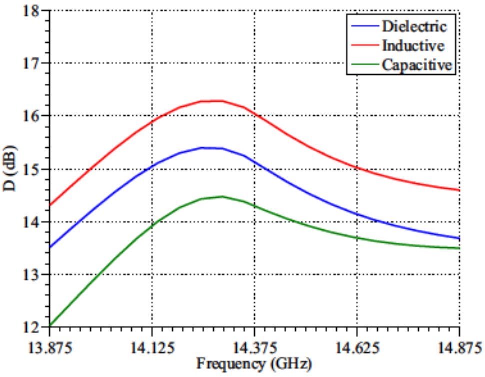

Fig. III.2.9 Directivity as a function of the frequency for the equivalent LWA starting from ε_r=10. The dielectric LWA bandwidth is BW=3.8%, whilst the bandwidth for the inductive and capacitive-based LWAs is 3.7% and 5.7%, respectively.

III.2.2 LWA Designs for Array Applications

In this section, we present three antenna designs based on the geometries shown in Figure III.2.1 that could be used for the application scenario described in the introduction. The three equivalent solutions take as baseline a dielectric constant ε_r=10 and fulfill the equivalence condition derived previously. In contrast with the previous section, here the structures have been analyzed using a commercial software [95] including a waveguide source and a finite ground plane/superstrate ($9.9\lambda_0$ by side). The effect of the TM_0 can be reduced by using a double slot opening in a ground plane as proposed in [27], (see Figure III.2.10) . In the inductive strip grid based MTS case the double slot iris is used to avoid the power loss related to the SW. Therefore it is important to understand if the directivity increase for the inductive strip grid based MTS is still achieved with respect to a well-designed dielectric based LWA. This iris can also be used to match the reflection coefficient S_{11} of the antenna. Figure III.2.11 presents simulated directivities versus the frequency.

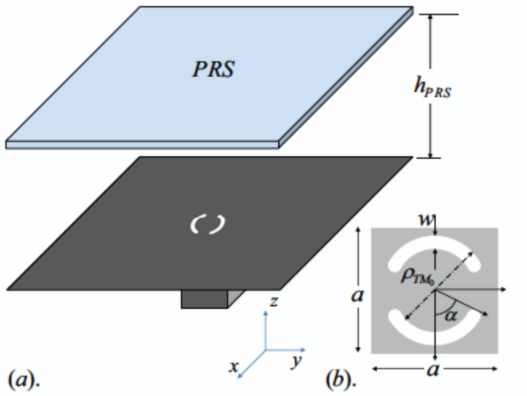

Fig. III.2.10 Description of the basic antenna and iris used to feed the cavity. The parameters of the slots in the iris are $a = 14.6mm$, $w = 0.5mm$, $\rho_{TM_0} = 10.79mm$ and $\alpha = 79deg$. The squared waveguide has a length of $wg = 0.7\lambda_0$ by side.

All the cases in Figure III.2.11 present higher directivities with respect to the theoretical results of Figure III.2.9 due to the inclusion of an actual source feeding the LW cavity. The capacitive case presents also a small frequency shift. Even with the inclusion of the source and suppression of the TM_0 mode, the inductive LWA presents higher directivities over comparable bands. The values of the maximum directivities for each case are summarized in Table III.2.2 for the central frequency f_0=14.375GHz. The radiation patterns for each design are shown in Figures III.2.12 and III.2.13 for the E- and H-plane, respectively, at the frequency at which the directivity is the highest.

Directivity (dB)	Dielectric	Inductive	Capacitive
ε_r=10 at f_0	17.1	18.24	16.52
ε_r=10 at best performance	17.48	18.32	17.62

Table III.2.2 Directivities for the equivalent MTS and dielectric geometries with ε_r=10 at central frequency and maximum value in the band.

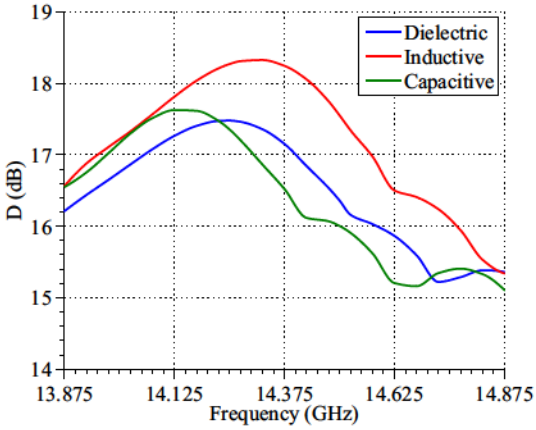

Fig. III.2.11 Directivity as a function of the frequency for the equivalent structures described in Figure III.2.1. The waveguide dimension is $w_g = 0.7\lambda_0$ and the width of the iris has been fixed to w=0.51mm whilst the diameter of the iris has been fixed to $\lambda_{TM_0}/2$ of each case (10.73mm, 10.43mm and 10.66mm for dielectric, inductive strip grid and capacitive slot grid based MTS respectively). The 1dB directivity BW is 3.86% for dielectric, 3.51% for the inductive and 3.3% for the capacitive case respectively.

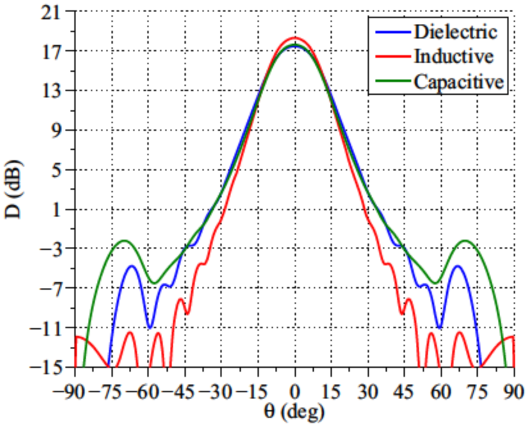

Fig. III.2.12 E-plane Comparison of CST simulated radiation patterns for the equivalent structures described in Figure III.2.11 at the frequency with highest directivity.

III.2.3 Experimental Verification

In order to validate the claim of this section, we have fabricated and measured two prototypes: the dielectric and the inductive based LWA. The dielectric material used for the super-layer is AR1000 with permittivity ε_r=10 and a thickness of 1.57mm. The operation

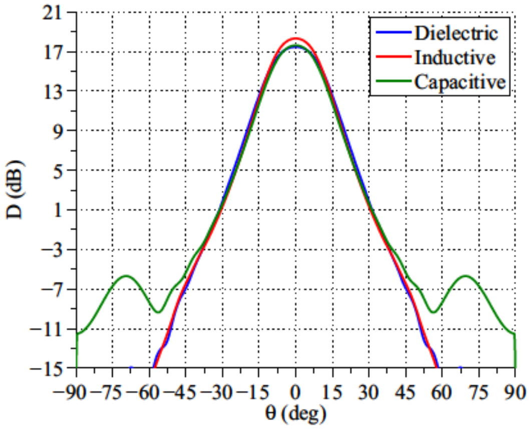

Fig. III.2.13 H-plane Comparison of CST simulated radiation patterns for the equivalent structures described in Figure III.2.11 at the frequency with highest directivity.

frequency is set to 14.375GHz. Figure III.2.14 shows the designed transition, together with the geometrical parameters, from a squared waveguide to a standard rectangular waveguide, necessary for measuring the manufactured prototype. Both manufactured LWA will use the same waveguide feed for simplicity. The MTS has been printed on a Kapton layer (with 0.05*mm* thickness and ε_r=3). This is a flexible material that has been supported by a thin foam layer (with 3*mm* thickness and ε_r=1.067) for the prototype. The inclusion of these layers alters the leaky wave propagation constants for the MTS case. This change can be easily compensated by modifying the cavity dimensions and strip dimensions. To this purpose, we have calculated the solution of the dispersion equation associated with the transmission line model shown in Figure III.2.15. The new cavity dimension is h_{MTS}=6.41*mm* and the width of the strip *w* has changed from the original value of 0.94*mm* to 1*mm*. By changing these parameters, we have been able to obtain the same leaky wave propagation constant as the free standing MTS based LWA, as it is detailed in Table III.2.3.

Inductive strip grid based MTS	k_{z1}^{TE}	k_{z1}^{TM}
air	$0.179-0.163i$	$0.179-0.161i$
Kapton+foam (not optimized)	$0.156-0.163i$	$0.156-0.163i$
Kapton+foam (optimized)	$0.179-0.163i$	$0.179-0.161i$

Table III.2.3 Original and optimized inductive strip grid based MTS design.

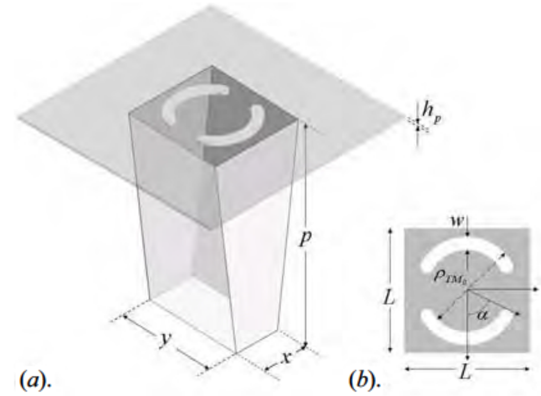

Fig. III.2.14 Description of the iris and transition used to feed the cavity. The parameters of the feeder are for the transition $x = 6.48mm$, $y = 12.95mm$, $p = 45.22mm$, $h_p = 0.5mm$ and the slots in the iris $a = 14.6mm$, $w = 0.5mm$, $\rho_{TM_0} = 10.79mm$, $\alpha = 79deg$. The same basic antenna will be used in both dielectric and inductive strip grid based MTS.

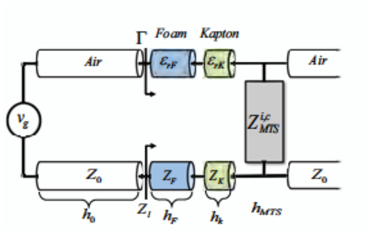

Fig. III.2.15 Practical realization of the inductive strip grid based MTS LWA.

The simulated radiation patterns of the two prototypes are presented in Figure III.2.16. The total antenna size is 9.91x9.91λ_0. We have also included the losses (i.e. for the foam is $tan\delta$=0.0041) and thickness of metals in the simulations. From the simulations a clear increase in directivity is observed for the inductive strip grid based MTS LWA. This increase is approximately 1.6dB. The simulated directivity in the frequency band is shown in Figure III.2.17.

Study of the fabrication tolerances

Before starting the fabrication of the prototypes, a complete analysis of the fabrication tolerances was carried out. The most critical parameters are associated with the highly resonant cavity. The first critical parameter is the height of the cavity h$_{MTS}$. The impact of the height

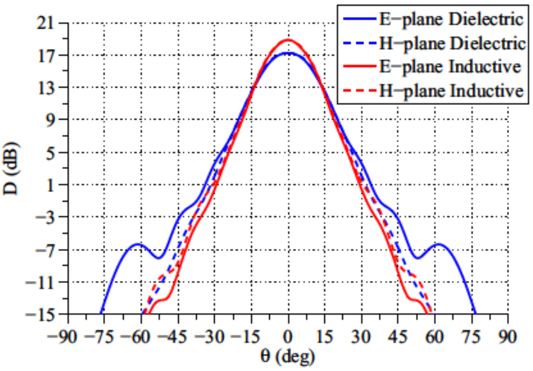

Fig. III.2.16 Simulated radiation pattern for the two prototypes. The directivity of the dielectric superlayer and inductive strip grid based MTS antenna are 17.2dB and 18.8dB respectively at *f*=14.25GHz. Both antennas are fed with the iris shown in Figure III.2.14.

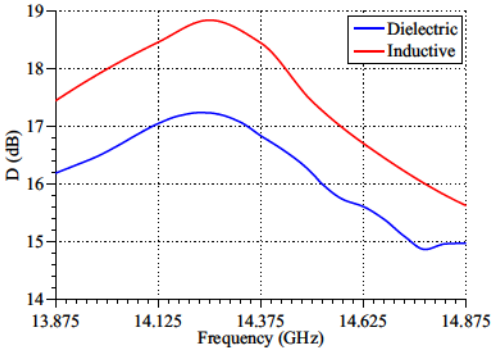

Fig. III.2.17 Simulated directivity in dB for the dielectric and equivalent inductive antennas. The BW is respectively 4.23% and 3.45% for the dielectric and inductive strip grid based MTS prototype with iris and transition.

of the cavity over the radiated fields was already reported in [121]. A variation in our design of around $h_{MTS}+10\%$ (i.e. in the inductive strip grid based MTS LWA) decreases the directivity around 2dB and moves the resonance at lower frequencies whilst a small variation of $h_{MTS}-10\%$ decreases the directivity around 1dB and moves the resonance at higher frequencies. It is worth noting that this parameter has also an important impact on the reflection coefficient. The second parameter that has been studied is a tilt angle of the MTS layer. We have done several simulations of the MTS antenna varying this angle. This parameter affects more strongly the radiation pattern than the matching of the reflection coefficient compared to the other parameters. The effect of this parameter over the radiation pattern is a loss of directivity and a deviation of the pointing angle as this alters the phase distribution over the antenna aperture. A small deviation of 0.3*deg* in this design of $9.91\text{x}9.91\lambda_0$ represents a loss of directivity of around 1dB and a misalignment of the main lobe of around 5*deg*. Taking into account these considerations, we have built and measured the prototype to the best of our laboratory facilities.

Measurements

The fabricated prototypes are shown in Figure III.2.18. Figure III.2.19 shows the measured gain as a function of the frequency. A frequency shift with respect to the simulated directivity shown in Figure III.2.17 has been measured for both the dielectric and inductive based LWAs. The height of the cavity is a sensitive parameter in this type of antennas, and it has to be manually adjusted during the measurements. A more accurate fabrication process would resolve this shift. Despite that, the dielectric and inductive measured gain presents same BW of around 2.52%. The maximum gain is measured at f=13.9GHz. At this frequency the dielectric super-layer and inductive strip grid based MTS antenna have 16.6dB and 19.6dB of directivity respectively (see Figure III.2.20).

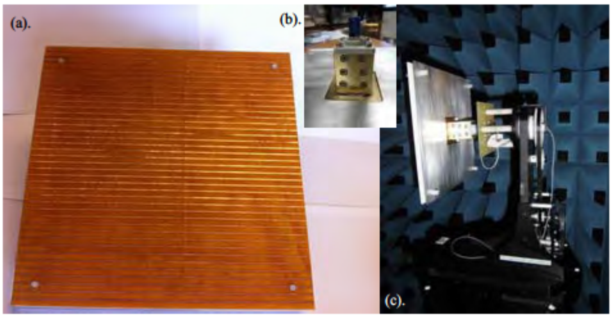

Fig. III.2.18 Prototype photos for (a). MTS (b). waveguide transition (c). measurement set-up

Figure III.2.20 shows the measured radiation patterns for the two prototypes in the main planes at f=13.9GHz. It is evident that the measured radiation patterns agree quite well with the simulated ones, despite the measured frequency shift.

The measured S_{11} is shown in Figure III.2.21 for both, dielectric and inductive strip grid based MTS cases. In the same graph, the results from full wave simulations are included for comparison purposes. Both antennas present comparable frequency bandwidths. The

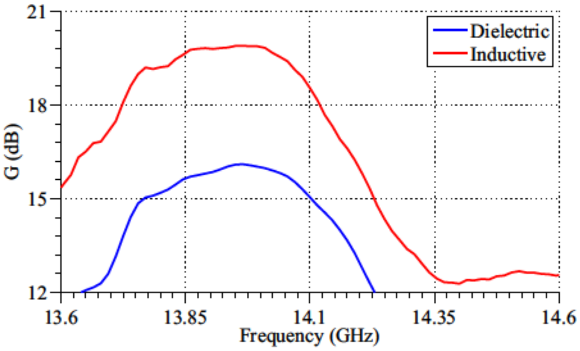

Fig. III.2.19 Measured gain for the dielectric and equivalent inductive LWAs. The BW is 2.52% for both prototypes.

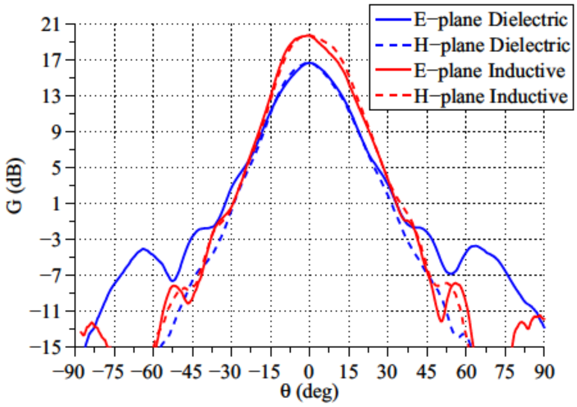

Fig. III.2.20 Measured radiation pattern for the two prototypes. The measured gain of the dielectric super-layer and inductive strip grid based MTS antennas are 16.6dB and 19.6dB respectively at f=13.9GHz. Both antennas are fed with the iris shown in Figure III.2.14.

agreement is quite satisfactory and no significant frequency shift is observed in this case. The measurement campaign for the Figure III.2.21 has been done at a different measurement facility. We believe that the cavity height was not placed at exactly the same position than in the radiation pattern measurements.

In this Chapter, we have rigorously compared the performances of LWAs based on dielectric superlayers with LWAs based on inductive strip and capacitive slot grid based MTS by imposing an equivalence in terms of the fundamental TE/TM modes. This equivalence ensures that the three antennas have comparable frequency bandwidths and levels of mutual coupling if they were to be used in array configurations. We have found that the inductive

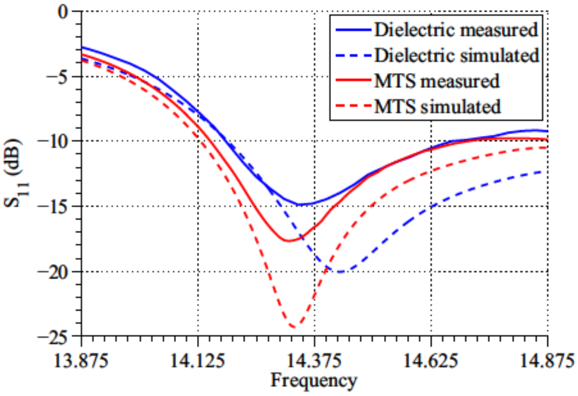

Fig. III.2.21 Measured S_{11} for the dielectric and equivalent inductive antennas. Simulated results are also included for comparison purposes. The BW of the reflection coefficients S_{11} are 3.62% and 3.90% for the measured dielectric and MTS prototypes respectively.

strip grid based MTS leads to the higher directivity enhancement for the same bandwidth. Numerical full wave analysis and experiments have confirmed the theory showing an improved directivity of more than 1dB with the same frequency band of operation. This improvement is especially significant for thinned phased arrays and focal plane arrays based on LWA elements.

Chapter III.3

Mutual coupling impact on leaky wave thinned phased arrays

In order to extend the previous results respect to the inductive MTS, we have to study the impact of the leaky wave modes in a phased array scenario. As application scenario, we consider a maximum scanning angle set to $8.6deg$, and an array spacing of $1.5\lambda_0$ with a relative frequency bandwidth of 5%. For such scenario, it would be desirable to maximize the gain over the scanning and frequency ranges by reducing the grating lobe level. Following these specifications, we will design three leaky wave phased arrays with different levels of mutual coupling. The study will be based on full wave simulations of 11x11 element phased arrays. The conclusions that will be derived in this Chapter can be extended also to PRS based on FSSs. Finally we will also compare the performances of the leaky wave phased arrays with a phased array of standard conical horns.

III.3.1 Array Element Geometry

The array element geometry is the same as the one presented in [38]. The geometry of the array is shown in Figure III.3.1 (for clarity purposes only a 5x5 array is shown). The array is composed of squared waveguide feeds loaded with a double slot iris. This iris is used to match the impedance and to reduce the propagation of the TM_0 mode which is present in the leaky wave cavity [38]. This mode radiates around the Brewster angle leading to increased sidelobes at large angles in the element radiation pattern as we have seem in the previous Chapter. The double slot separation, ρ, has been set to be half of the TM_0 leaky mode wavelength. A circular iris is chosen to reduce the effect of this mode also along the diagonal planes of the antenna. On top of the ground plane placed at $h_1 = \lambda_0/2$, there is a quarter wavelength dielectric superlayer with permittivity ε_r and thickness $h_2 = \lambda_0/4\sqrt{(\varepsilon_r)}$ verifying the standard resonant condition to maximize the directivity in PRS antennas [6]. Three dielectric constants are considered in this study: ε_r=4,8 and 12. The ground plane thickness has been fixed to $h_p = \lambda_0/60$ and the squared waveguide dimensions to $a_0 = 0.7\lambda_0$.

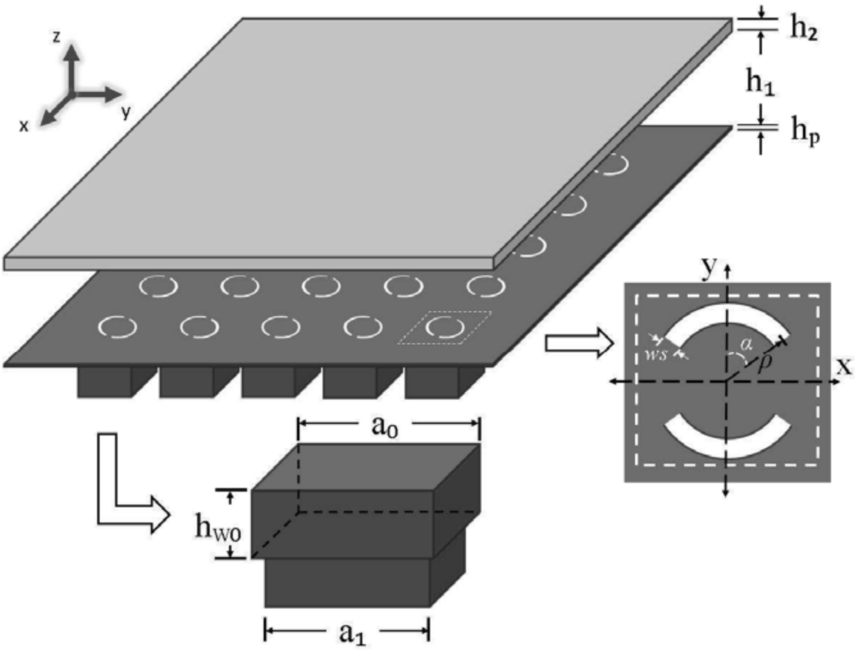

Fig. III.3.1 Antenna geometry. Upper: 5x5 array with dielectric superlayer at top, h_1 is the cavity height and h_2 is the dielectric thickness. h_p is the ground and iris thickness. Each element is composed of a squared waveguide feed and a double slot iris. Lower center: structure of waveguides used to match the active impedance. Center right: parameters of the iris for each element.

The single antenna input impedance can be easily matched by optimizing the iris's width, w_s, and length defined by the angle α. The input reflection coefficients of the single elements, simulated with CST MWS, are shown in Figure III.3.2 for the three considered dielectric constants. The final dimensions of the iris are given in the figure caption. Clearly, the larger the dielectric constant is, the smaller is the impedance bandwidth [118]. Even so, all dielectric constants selected for the study lead, in principle, to a sufficient bandwidth for

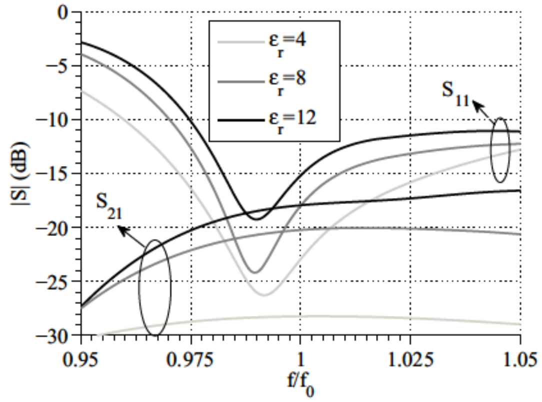

Fig. III.3.2 Reflection coefficient S_{11} and mutual coupling S_{21} at $1.5\lambda_0$ for different dielectric superlayers. The iris dimensions are $w_s = 0.028\lambda_0, 0.024\lambda_0, 0.024\lambda_0$ and $\rho = 0.526\lambda_0, 0.516\lambda_0, 0.5\lambda_0$ for each dielectric constant respectively.

the considered application.

Figure III.3.3 shows the radiation pattern at the central frequency for the three single antennas in the E-plane. It is possible to appreciate that the larger the dielectric constant, the larger is the roll-off of the field and therefore the attenuation of the grating lobe (present at an angle of $31deg$ for broadside radiation pattern). The patterns shown in Figure III.3.3 present very steep roll-off thanks to the suppression of the spurious TM_0 mode with the use of the double iris, which is usually ignored by most authors.

III.3.2 Mutual Coupling Impact and Compensation

The selection of the dielectric constant is a trade-off between the attenuation of the grating lobes and the impact of the mutual coupling on the embedded pattern. Figure III.3.3 also shows how mutual coupling level, at a distance of $1.5\lambda_0$, increases with the dielectric constant. The mutual coupling impacts on both the active input impedance and the embedded pattern. In [38] it was shown that a maximum mutual coupling value of -20dB is acceptable for the design of multibeam antennas based on leaky wave arrays. Here we will see that this limit is also a good compromise for the phased array applications. In order to study the impact of the mutual coupling on the embedded pattern, we have simulated a 5x5 array where only the central element is fed. The simulations have been done on a small 5x5 array assuming that only the two neighboring elements contribute significantly to the embedded pattern and active impedance. The impact of the coupling can be observed in Figure III.3.3, where the embedded patterns are shown for all three dielectric cases together with the isolated element patterns. Due to the fact that the closest elements are not radiating in phase with respect to the central element, the directivity at broadside of the embedded pattern is reduced with respect to the isolated case. This effect is more significant as the dielectric constant increases. For ε_r=4, the effect of the mutual coupling is negligible and the single and embedded patterns are basically the same. However, the attenuation of the grating lobe at $31deg$ is only -8.4dB. For ε_r=8, the difference between the two patterns is a bit larger, but even so we obtain a larger attenuation of the grating lobe (-12.4dB). Instead, for the case with the largest mutual coupling (ε_r=12), the enhanced directivity at broadside with respect to the ε_r=8 case is reduced significantly in the embedded pattern, and therefore practically all the possible improvement on the grating lobe attenuation is also lost leading to just a 2.75dB better attenuation than the ε_r=8 case. Moreover, the use of this dielectric also comes at the cost of a reduced frequency impedance matching leading to a lower phased array gain as we will see in the next section.

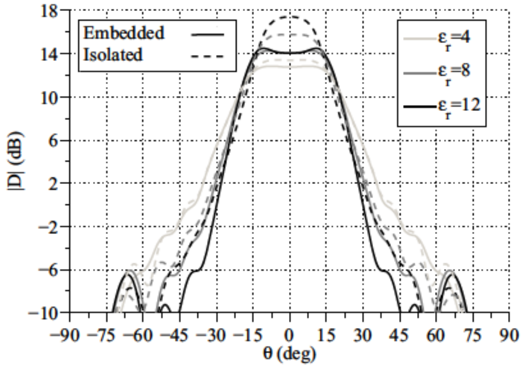

Fig. III.3.3 Comparison between the 5x5 embedded and the element pattern in the E-Plane for each dielectric superlayer (ε_r=4,8,12) at central frequency.

The mutual coupling has also an important effect on the active impedance. This active impedance for the central element at broadside can be calculated by summing all the mutual impedances as follows: $Z_(a_1) = \Sigma_{(i=1)}^{N} Z_1 n$, where the subscript $_1$ is related to the central element. The effect of the mutual coupling shifts the resonance of the antenna towards lower frequencies. This shift could be compensated by reducing the iris length using a smaller α. However this will impact on the TM$_0$ mode reduction on the diagonal plane. Here we have instead chosen to match this input impedance with a waveguide step as shown in Figure III.3.1 (lower center). The impedance has been matched with an in-house developed code by optimizing the length, h_{w0}, and the waveguide width dimension, a_1. For the case of ε_r=4, no matching structure is needed because of the low mutual coupling level.

In order to validate the presented leaky wave thinned array concept, full wave simulations of the three 11x11 phased arrays have been performed with CST MWS. Figure III.3.4.a,b,c show the active reflection coefficients of all the array elements of the leaky wave array at broadside for the three dielectric constant cases. The simulated active coefficient resembles very well the active coefficient designed in the previous section for all cases. For the ε_r=4 the black-solid curve predicted in our code is identical to the active reflection coefficient for all array elements. For the other two cases, even though differences are observed, we can still notice a good agreement for the optimized band. Figure III.3.4.d,e,f show the active coefficient at the limit of the scanning range, i.e. θ=8.6*deg*, in the H-plane. The dimensions of the waveguide step which are required to match the active impedance are given in the captions. Note that in the case of ε_r=12, the required waveguide dimensions lead to a cutoff frequency of 9.8GHz. In the E-plane for the same scanning angle similar results for the active coefficient have been observed.

Figure III.3.5 presents the H- and E-plane of the radiation pattern for the three phased arrays simulated at two scanning conditions: broadside and the edge of the scanning range. For comparison purposes, we have included in the figures the embedded patterns for each one of the cases. We can see how the array patterns follow very well these embedded patterns. The ε_r=4 array exhibits the lowest directivity and attenuation of the grating lobes. Instead the ε_r=12 array presents the highest grating lobe attenuation and directivity. However the directivity of the ε_r=8 case is practically the same than for ε_r=12 because of the effect of the mutual coupling of this last one in the embedded pattern. The grating lobe attenuation for ε_r=8 is only 3.1dBs worse than for the ε_r=12 case. This, together with the worse impedance matching of the high dielectric case, makes of ε_r=8 a better trade-off design and confirms the appropriate selection of a -20dB mutual coupling level.

A two-dimensional representation of the farfield in elevation and azimuth is shown in Figure III.3.6. The high spots observed at large angles are associated to the grating lobes. The grating lobe level is also significant in the D-plane. In this plane the grating lobe is located at 67*deg* which is close to the radiation angle of the TM_0 mode. In the diagonal plane, the suppression of this mode is not perfect because the iris current distribution is not constant over the whole iris. Even so, its effect is greatly reduced by the presence of this iris.

As a reference bench mark an 11x11 phased array of conical horns is also presented in this section. The conical horn length has been chosen to maximize its directivity [64]. The designed geometry and dimensions are shown in Figure III.3.7. The dimensions of the horn are given in the figure caption. Obviously, this array presents a very good impedance matching over the whole frequency and scanning range. The array and embedded patterns are shown in Figure III.3.8a and III.3.8b for H- and E-planes respectively. As we can see, the dielectric superlayer provides higher directivity and attenuation of the grating lobes than the classical solution of conical horn antennas.

Finally we can summarize the frequency and scanning behavior of the designed array in the following two figures. On the left axes, the values of the directivity and gain are provided. On the right axes, instead, the values of the grating lobes with respect to the maximum directivity are summarized. For all cases the sidelobe levels are below -12dB. Figure III.3.9.a shows the directivity, gain and grating lobe attenuation for broadside, whereas Figure III.3.9.b and III.3.9.c shows the same parameters but for a 8.6*deg* scanning in the H- and E-plane, respectively. We can observe that we obtain much better directivity values for all enhanced phased arrays than for the horn case because of the better array aperture illumination achieved with the leaky wave antennas. However, the case of ε_r=12 suffers from significant gain losses due to the limited matching of the active impedance. Instead the gain in the ε_r=8 case is practically the same than directivity. For this case we can achieve over 2.2dB more gain over all the frequency band and scanning range, and an attenuation of the grating lobes of more than 10dB.

As conclusion, we have shown that an increase in the gain of more than 2.2dB is obtained in the leaky wave array with respect to the horn array with a reduction of the grating lobe of -10dB over the complete frequency band. Moreover the proposed leaky wave phased array presents nearly constant gain over the whole scanning range, which is very suited for Earth coverage applications.

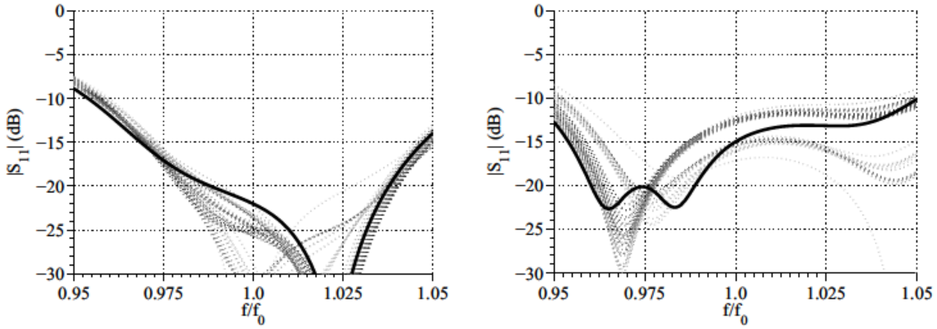

(a) ε_r=4 at broadside

(b) ε_r=8 at broadside

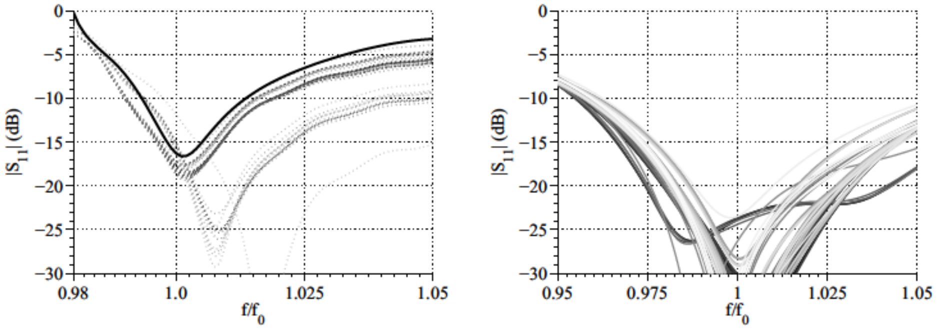

(c) ε_r=12 at broadside

(d) ε_r=4 at θ=8.6*deg* in the H-plane

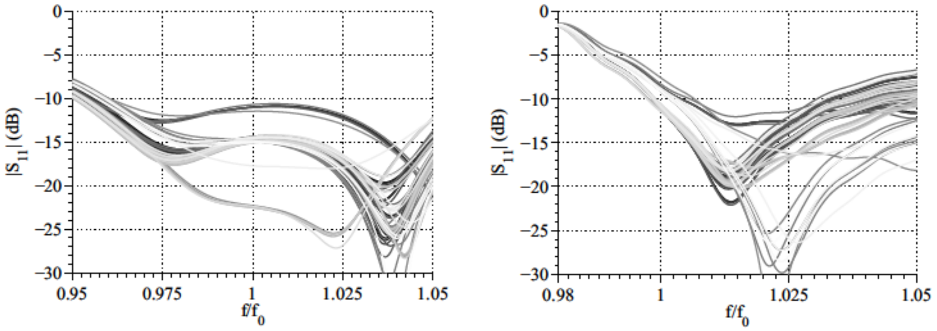

(e) ε_r=8 at θ=8.6*deg* in the H-plane

(f) ε_r=12 at θ=8.6*deg* in the H-plane

Fig. III.3.4 Active reflection coefficient for all elements of the 11x11 array. The active reflection coefficient simulated with the developed in house code for the active impedance is also shown in a black-solid line (upper figures).

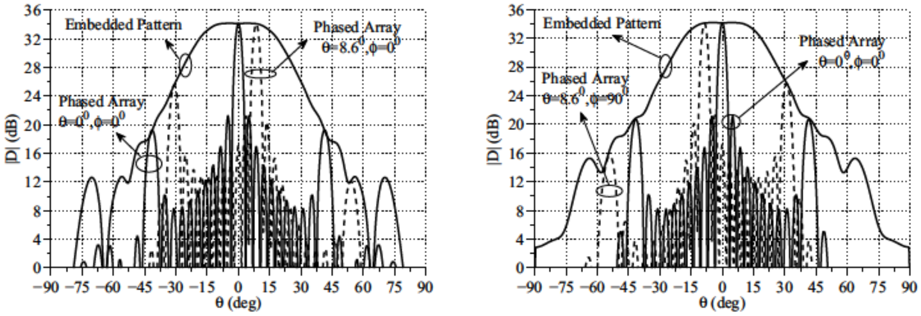

(a) ε_r=4 in the H-plane (b) ε_r=4 in the E-plane

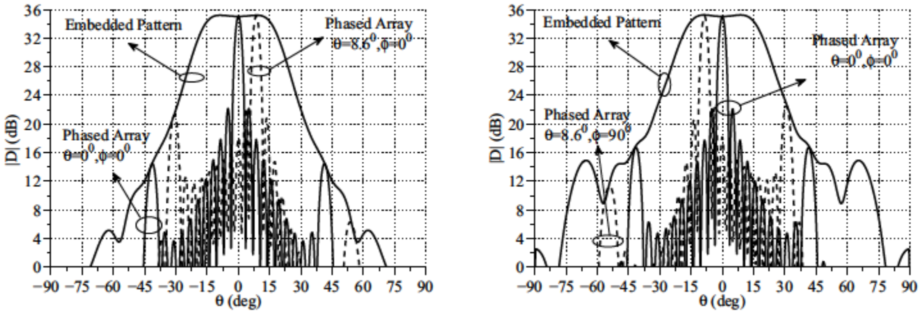

(c) ε_r=8 in the H-plane (d) ε_r=8 in the E-plane

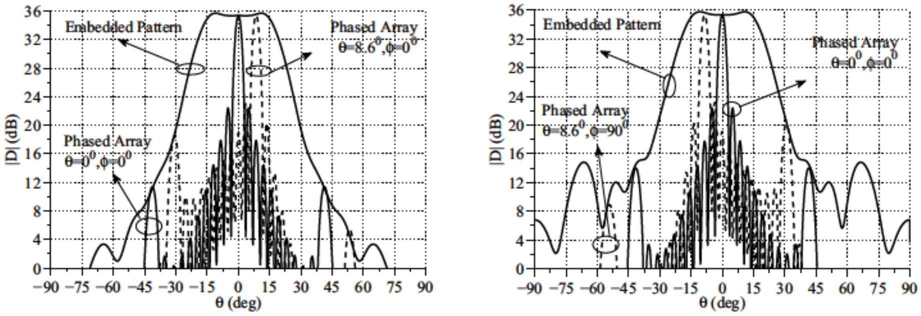

(e) ε_r=12 in the H-plane (f) ε_r=12 in the E-plane

Fig. III.3.5 Embedded and the 11x11 array radiation patterns for the dielectric superlayer antenna with ε_r=4, 8 and 12 at several scanning angles.

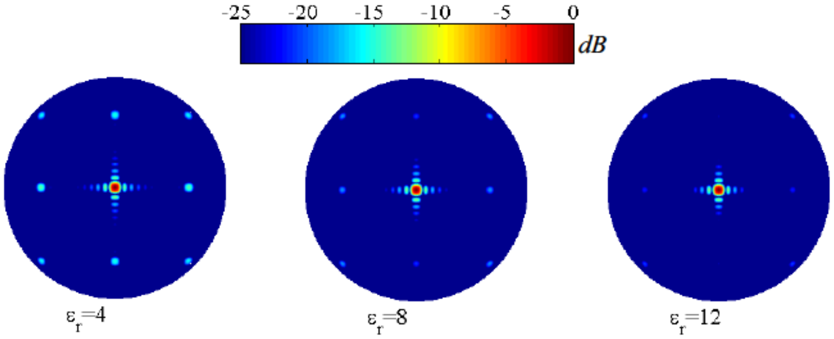

Fig. III.3.6 Farfield components in a polar coordinate system of the 11x11 phased arrays with ε_r=4,8,12.

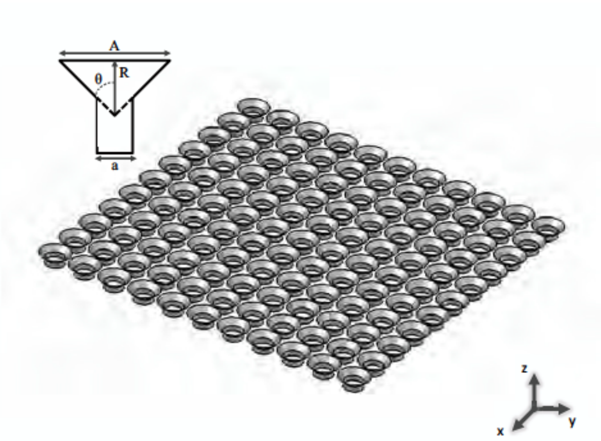

Fig. III.3.7 Horn array geometry. Center: 11x11 array of conical horns spaced 1.5λ_0. Upper detail: dimensions in order to maximize the directivity, A=1.4λ_0, a=0.86λ_0, R=0.653λ_0, $\theta = tan^{-1}(A/R)$.

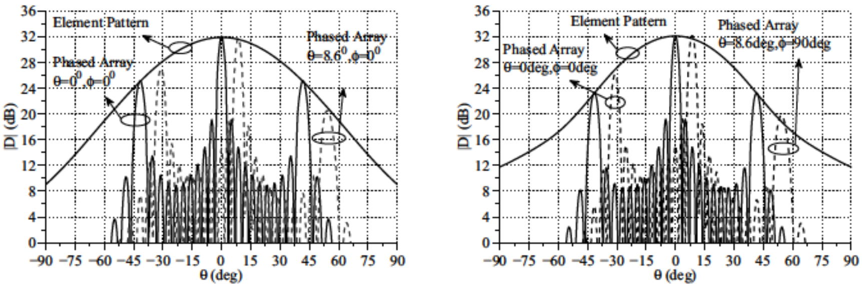

(a) (b)

Fig. III.3.8 (a). H-plane and (b). E-plane 11x11 array radiation patterns for the horn antenna array at scan $\phi=0deg$ and $\theta=8.6deg$.

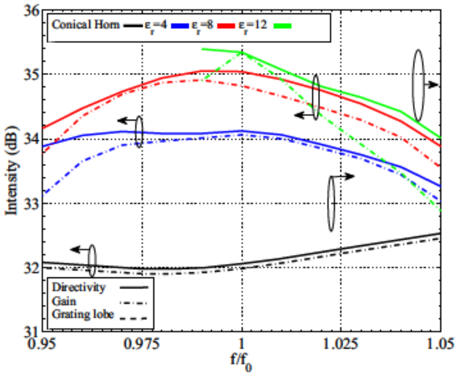

Broadside

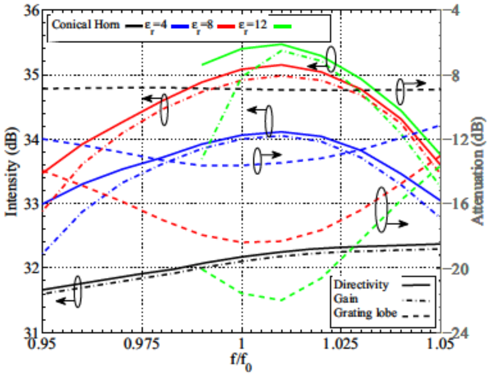

Scanning in the H-plane

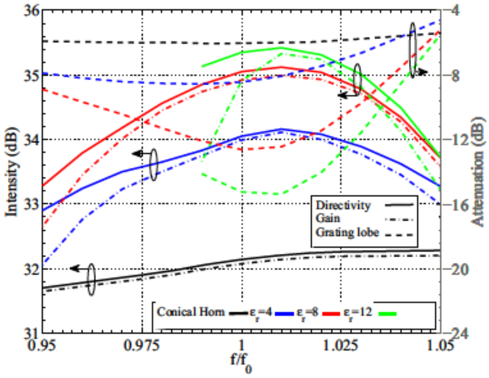

Scanning in the E-plane

Fig. III.3.9 Dependence on frequency of the main parameters of the leaky-wave array antenna for ε_r = 4, 8, 12 and conical horn cases at broadside, at one scan angle of 8.6*deg* in the H-plane and E-plane respectively.

Chapter III.4

Leaky Wave Thinned Phased Array in PCB Technology

In this Chapter, we want to show a practical implementation in PCB technology of the leaky wave thinned array concept. The presented array will be made in PCB and integrated with an inductive MTS super-layer. A full study of the performances of the 7x7 phased array antenna for several scanning angles is presented and compared with a reference solution based on 2x2 sub-arrays. This study will analyze the gain, directivity, grating lobe level, side lobe level, front to back ratio and beam efficiency as a function of the frequency for the leaky wave enhanced phased array.

III.4.1 Array Element Optimization

The array is coupled to an inductive MTS acting as the array PRS. In Chapter III.2, we showed that an inductive strip grid based MTS leads to higher directivity enhancement, in comparison with dielectric based or capacitive based leaky waves, but without compromising the antenna frequency bandwidth or mutual coupling thanks to the intrinsic suppression of the TM_0 undesired leaky mode. This section presents an implementation that fulfils the specifications, summarized in Table III.4.1, for future telecommunication Ku-band satellites. The array phase-shifting is performed on array elements separated at a distance of $2\lambda_0$ to reduce the front-end cost. Two array configurations, shown in Figure III.4.1.a and III.4.1.b, are designed in PCB technology and optimized to fullfil these requirements: an array of leaky wave antenna elements and a more classical approach consisting of array elements made by 2x2 sub-arrays. The number of elements in the leaky wave array is decimated by a factor of 4 with respect to the reference array. For this scenario, the grating lobes will appear in the angular region from 26*deg* to 90*deg* for the considered scanning range.

Scenario	
Pointing angle	$\Delta\theta = 8.6deg$
Inter-element distance	$2\lambda_0$
Work band (GHz)	Ku-band (14.25-14.5)
Elements distribution	7x7 squared lattice
Polarization	Linear

Table III.4.1 Specifications for the application scenario.

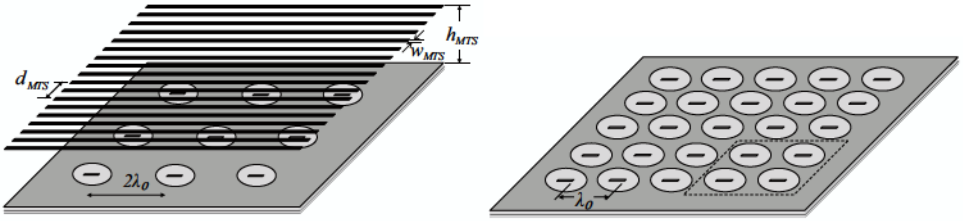

(a)

(b)

Fig. III.4.1 (a). Leaky wave thinned phased array: h_{MTS} is the cavity height, w_{MTS} and d_{MTS} are the MTS periodicity and strip width respectively. The array has a periodicity of $2\lambda_0$. (b). thinned phased array composed by 2x2 sub-arrays. The array element spacing is λ_0, but the phase shifting is applied at the sub-array level (i.e. corresponding to a periodicity of $2\lambda_0$).

The geometry of the array element is shown in Figure III.4.2. The array is printed on a double grounded substrate of dielectric constant ε_r=2.2 and with a height of $h = 3.2mm$. The height is selected in such a way that only the TM_0 surface wave inside this substrate is above cut-off. Surrounding the antenna, there is a circular cavity of radius r_s=9.15*mm* made of via-holes to avoid the propagation of this surface wave. The antenna is matched to a 50Ω SMA connector via a microstrip stub with dimensions L_m=5.20*mm* (length of stub) and w_m=0.50*mm* (width of the stub). The dielectric substrate for the microstrip stub has a thickness of h_m=0.5*mm* and the same permittivity $\varepsilon_r = 2.2$. The presented antenna is similar to the one reported in [88] where a planar EBG was used to suppress the TM_0 surface wave instead of the via-holes proposed in this configuration. At the bottom of the

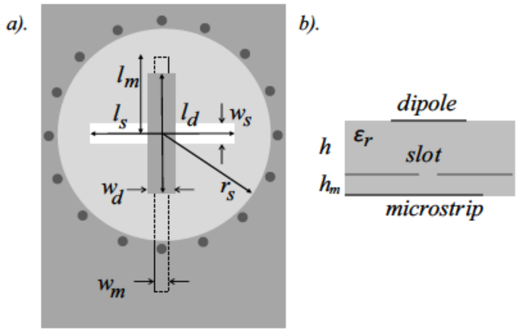

Fig. III.4.2 Antenna geometry of the single element: top and side views of the printed antenna microstrip element: slot (l_s, w_s) in a via-hole based circular cavity (ρ_s) coupled to a dipole (l_p, w_p) and excited via microstrip (l_m, w_m). (a). top view and (b). side view.

circular cavity, there is a slot excited via a microstrip line. The width and length of the slot are w_s=0.79*mm* and L_s=10.50*mm* respectively . At the top of the cavity there is a dipole of length L_d=7.68*mm* and width w_d=0.20*mm* used to increase the frequency bandwidth of the antenna and to improve the symmetry of the radiated field in the main planes. The optimal solution was selected with respect to the symmetry of the pattern and the reflection coefficient. In Figure III.4.3, the radiated field of the proposed antenna element is shown, here the good rotational symmetry of the patterns is clearly observed.

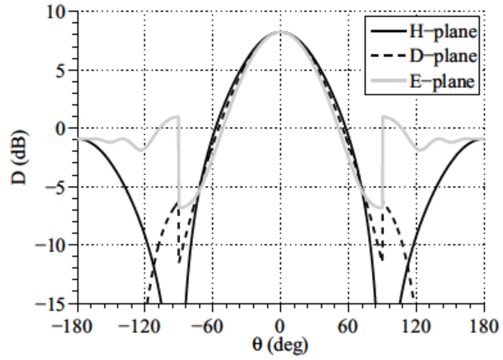

Fig. III.4.3 Simulated radiation patterns of the array element designed in PCB.

This element geometry will be used as the building element in the reference array as well as in the proposed leaky wave one. The benchmark case is composed of a 2x2 sub-array with the elements placed at a distance of λ_0 from each other (see Figure III.4.1.b). Instead, for the proposed leaky wave approach, an inductive MTS at certain height h_{MTS} as shown in Figure III.4.1.b is located on top of the ground plane. Following the conclusions derived in Chapters III.2 and III.3 we have designed the MST (d_{MTS}=5.20mm,w_{MTS}=1.05mm,h_{MTS}=9.55mm) equivalent to a dielectric superlayer with ε_r=10, in order to have a level of mutual coupling between the array elements at a distance of $2\lambda_0$ of -20dB. Figure III.4.4 shows the reflection coefficient S_{11} for both array elements. The benchmark one presents a very good matching over a frequency band of more than 7%. The MTS one, instead, presents a smaller bandwidth due to the resonant frequency behaviour of the leaky wave antennas. Nevertheless, this bandwidth is sufficient for the considered application (i.e. 14.25-14.50GHz).

Figure III.4.4 also presents the directivity of the two designed array elements as a function of the frequency. Due to its resonant behaviour, the directivity varies rapidly with the frequency in the MTS case. Even so, the directivity for the MTS is larger than for the benchmark in the frequency bandwidth of interest. The MTS and the benchmark present significantly low values of cross-polarization. In both designs the level of cross-polarization is at least 38dB below the co-polarization level in the entire band and this is considering not the global maximum of each of them, but the value of co/cross polarization at the same angle (we have considered angles up to 10deg according to the scanning specifications). Indeed as described in [122], the broadside radiation generated by leaky wave Fabry-Perot antennas comes from almost perfectly polarized aperture field.

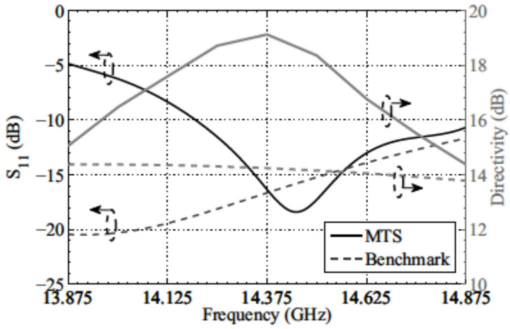

Fig. III.4.4 Reflection coefficient S_{11} and directivity for MTS leaky wave element (solid lines) compared to the basic printed antenna element of the benchmark reference (dashed lines). The reflection coefficient is shown in the left axis whilst the directivity is represented in the right one.

A two dimensional representation of the farfield in elevation and azimuth at 14.375GHz is shown in Figure III.4.5 and III.4.6 for the benchmark and MTS array elements, respectively. The plots shown in (a) and (b) are the radiated fields in the upper medium (i.e. $0 \leq \theta \leq 90$). Instead, the plots shown in (c) and (d) are the radiated fields in the lower medium (i.e. $90 \leq \theta \leq 180$ or the back radiation). Also in the left part of each figure we can find the co-polarized fields whilst in the right side we have the cross-polarized fields. As we can see, the MTS antenna provides significant lower levels of cross polar component of the field than the benchmark [122] as well as lower front to back ratio. Figure III.4.7 shows the radiated fields for both antenna elements in the H-plane at 14.375GHz as an example. We can appreciate that the MST provides higher directivity, thanks to the leaky wave enhancement and the lower front to back ratio. In the same Figure, the embedded pattern for the MTS case of the center element in a 5x5 array configuration is also included. This element embedded pattern presents lower directivity due to the effect of the mutual coupling as described in [43, 113]. Even if the directivity is reduced from the isolated case, the MST case still leads to a larger attenuation of the grating lobes that will be present in the angular region from $26deg$ to $90deg$ for the considered scanning range when compared to the benchmark case.

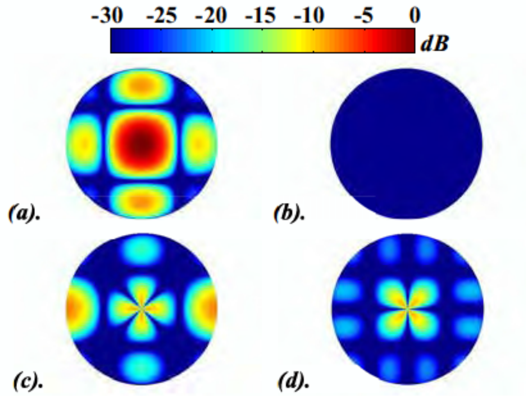

Fig. III.4.5 2D representation of the benchmark array element radiation pattern: (a). co-polarized and (b). cross-polarized fields in the upper medium, (c). co-polarized and (d). cross-polarized fields in the lower medium.

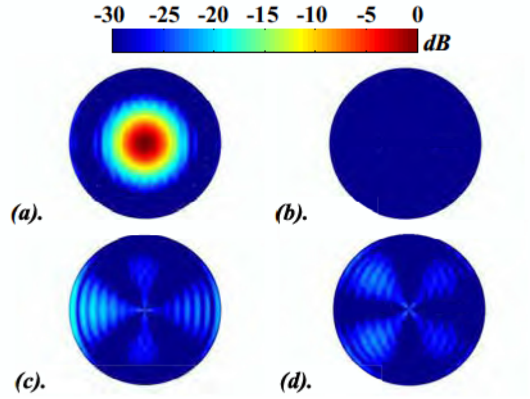

Fig. III.4.6 2D representation of the MTS array element radiation pattern: (a). co-polarized and (b). cross-polarized fields in the upper medium (c). co-polarized and (d). cross-polarized fields in the lower medium.

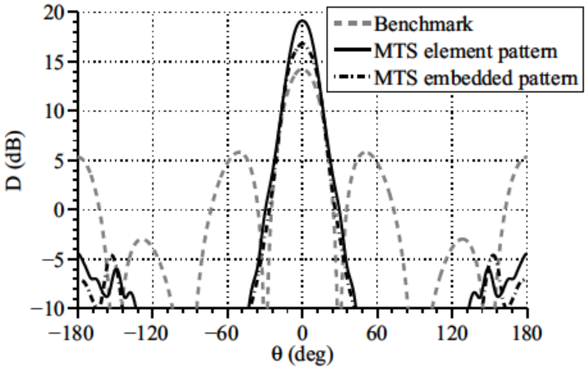

Fig. III.4.7 H-Plane radiation pattern of the benchmark and MTS based array elements at the central frequencies (including embedded pattern of a 5x5 array for the MTS case).

III.4.2 Phased array performances

In this section, we investigate the performances of a leaky wave thinned array compared to a thinned array based on phasing sub-arrays (seen in Figure III.4.1). We present full wave simulations carried out with CST MWS [95] of 7x7 phased arrays scanning at broadside and at the edge of the scanning range, $\theta = 8.6deg$, in both H- and E-planes. The array element phasing is at spacing of $2\lambda_0$ for both cases. Due to the low mutual coupling in the bechmark array, the active reflection coefficients are well matched in the entire band. For the MTS array, the active reflection coefficients are slightly moved to the left with respect to the impedance of the single element (seen in Figure III.4.4). Figure III.4.8 shows the simulated active reflection coefficient for all the 49 array elements at several scanning conditions. For all the shown cases, the active reflection coefficients are well-matched over the frequency band of interested. The bandwidth of the benchmark is obviously larger due to the inherent lower mutual coupling.

A two dimensional representation of the farfield in elevation and azimuth at the central frequency, 14.375GHz, is shown in Figures III.4.9-III.4.11 for the three simulated scanning conditions. The plots shown in (a) and (b) are the radiated fields in the upper medium for the MTS and benchmark arrays, respectively. Instead, the plots shown in (c) and (d) are the radiated fields in the lower medium (back radiation). As we can see, the MTS based array provides higher attenuation of the grating lobes than the benchmark in all the cases.

Figures III.4.12 and III.4.13 show the embedded pattern and the array radiation patterns for two scanning angles (at broadside and at scan angle of $\theta = 8.6deg$) of both arrays in the H-plane at the central frequency. The embedded pattern in the MTS case is calculated using 5x5 elements. In the benchmark case the element pattern of the 2x2 sub-array embedded in an array is basically the same than the isolated sub-array because this antenna presents a very low mutual coupling. The position of the nearest grating lobe for the benchmark at broadside and at the maximum scanning angle is $\pm 90deg$ (i.e. because the inter-element distance at broadside in the sub-array is λ_0) and $\pm 20deg$ respectively. For the same situations the grating lobes are at $\pm 30deg$ and $\pm 20deg$ for the MTS array. At broadside the nearest grating lobe is attenuated 18.79dB (benchmark) and 19.31dB (MTS). Moreover a larger improvement in the suppression of the grating lobe can be clearly appreciated at the maximum scanning angle (θ =8.6deg) thanks to the angular filtering of the MTS case respect to the benchmark. There, the benchmark only leads to a 5dB attenuation of the grating lobe (i.e. attenuation respect to the maximum directivity at this scanning angle) whilst the MTS leads to 9.26dB.

To finalize, the performance analysis of the phased array, we present the variation of the main parameters as a function of the frequency for both the MTS based and benchmark arrays at the three scanning conditions previously studied. Figures III.4.14a and III.4.14d show the frequency variation, for both arrays, of the directivity (D), the gain (G), the grating lobe level (GL) and the front to back ratio (FB) at broadside. For all Figures the band

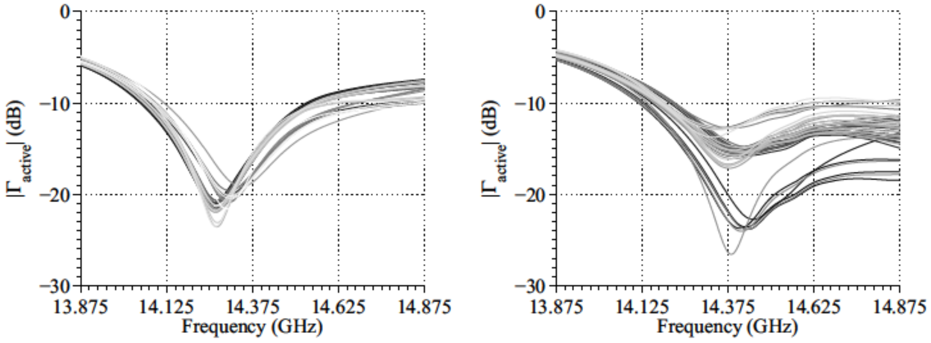

(a) 7x7 MTS array at broadside.

(b) 7x7 MTS array at $\theta = 8.6deg$ in H-plane.

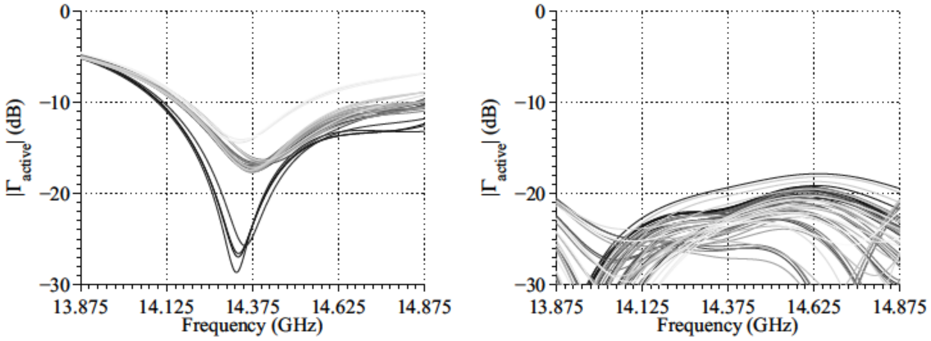

(c) 7x7 MTS array at $\theta = 8.6deg$ in E-plane.

(d) 7x7 reference array at broadside.

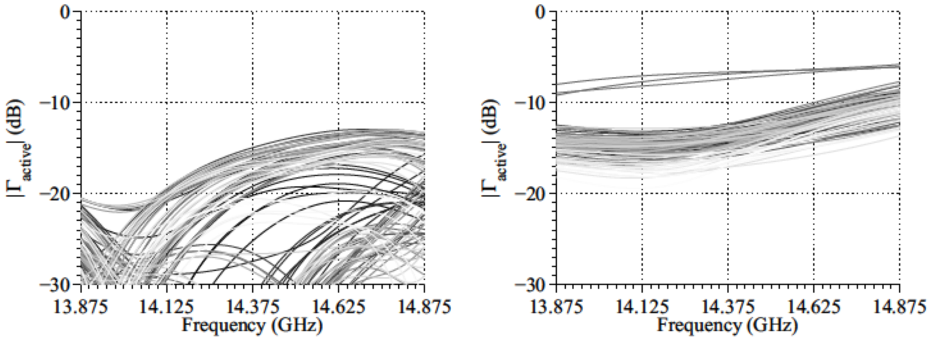

(e) 7x7 reference array at $\theta = 8.6deg$ in H-plane.

(f) 7x7 reference array at $\theta = 8.6deg$ in E-plane.

Fig. III.4.8 Active reflection coefficient calculated with CST for all of the 49 elements of the MTS and benchmark phased arrays at different scanning angles.

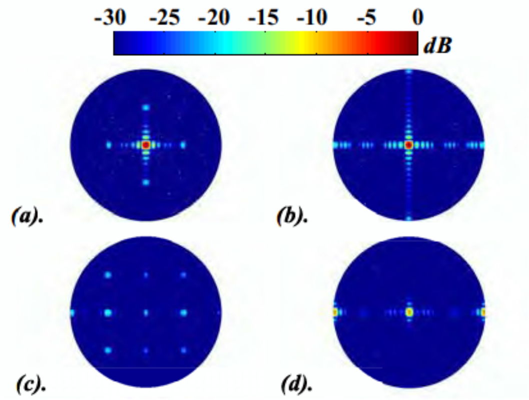

Fig. III.4.9 Farfield in the upper (a)-(b) and lower (c)-(d) medium in a polar coordinate system of the 7x7 MTS (a)-(c) and benchmark (b)-(d) arrays radiating at broadside.

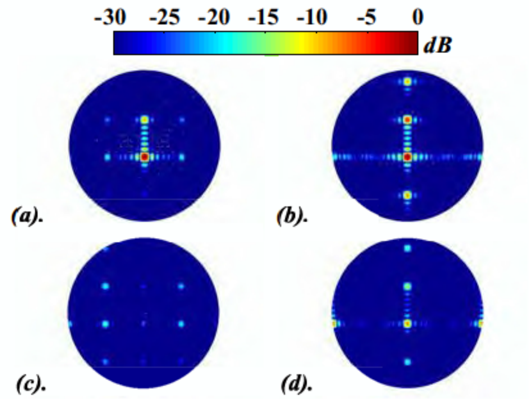

Fig. III.4.10 Farfield in the upper (a)-(b) and lower (c)-(d) medium in a polar coordinate system of the 7x7 MTS (a)-(c) and benchmark (b)-(d) arrays radiating at the scanning angle $\theta = 8.6deg$ in E-plane.

of interest is highlighted in gray. The grating lobe level (GL) is calculated as the difference between the maximum of the grating lobes and the maximum of the directivity. The front to back ratio (FB) is the relationship between the maximum radiation in the lower medium respect to the maximum in the upper medium. At broadside in the case of the benchmark, the location of the grating lobe is at $90deg$ because as mentioned before, the inter-element distance in the sub-array is λ_0 and they are all-in-phase for broadside radiation. For this situation, the back lobe level is comparable to the grating lobe level. The MTS array, also at broadside, provides larger directivity, and both lower grating lobe and front to back levels. Figures (III.4.14b-III.4.14e) and (III.4.14c-III.4.14f) show the same parameters

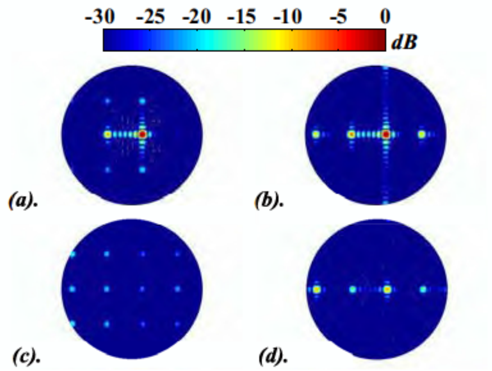

Fig. III.4.11 Farfield in the upper (a)-(b) and lower (c)-(d) medium in a polar coordinate system of the 7x7 MTS (a)-(c) and benchmark (b)-(d) arrays radiating at the scanning angle $\theta = 8.6deg$ in H-plane.

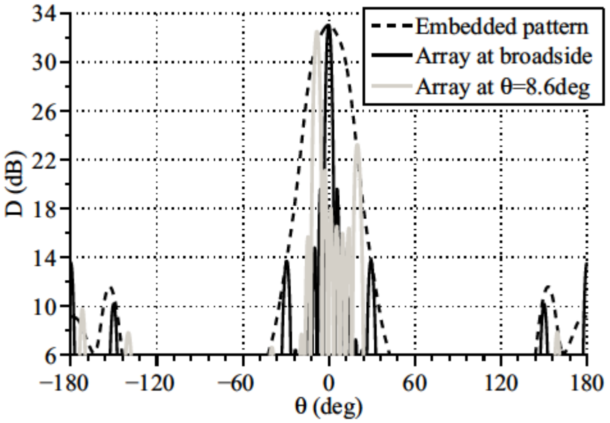

Fig. III.4.12 H-plane radiation pattern for the 7x7 phased array (MTS case) at broadside (dark solid line) and at scanning angle of $\theta = 8.6deg$ (gray solid line) including also the 5x5 embedded pattern (dark dashed line).

but for the other two extreme scanning conditions. Also in those cases, the MTS based array provides higher directivity and lower grating lobe level and front to back ratio. Over the frequency band specified in the application scenario (i.e. 14.25GHz-14.50GHz) and for the three scanning cases analyzed, the MTS array always provides at least 1dB more gain than the benchmark array.

To summarize, table III.4.2 presents the directivity, gain, grating lobe level, side lobe level and front to back ratio at the central frequency. The increase in the MTS gain is associated to several facts: the reduction of the grating lobe and of the back radiation, and a

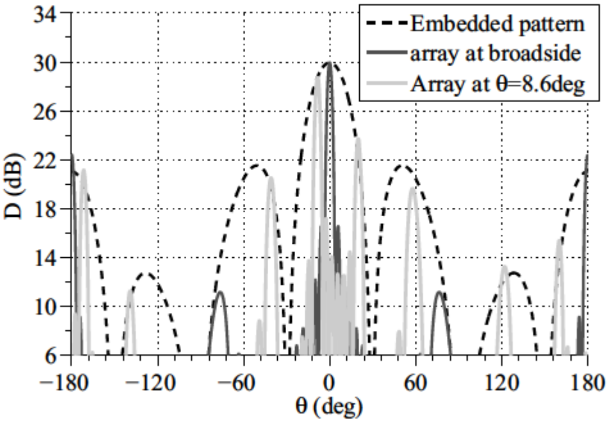

Fig. III.4.13 H-plane radiation pattern for the 7x7 benchmark array at broadside (dark solid line) and at scanning angle of $\theta = 8.6deg$ (gray solid line) including also the element pattern (dark dashed line).

slight increase in the radiating area at the array edges (see Figure III.4.1.a).

Benchmark MTS	Broadside	$\phi = 0deg$	$\phi = 90deg$
Directivity (D)	29.94 33.01	28.73 32.48	30.87 32.5
Gain (G)	29.91 32.92	28.69 32.35	30.67 32.4
Grating Lobe (GL)	-7.36 -17.63	-5.04 -9.26	-7.16 -8.91
Side Lobe (SL)	-13.4 -12.4	-11.56 -11.36	-11.96 -11.24
Front to Back (FB)	-7.36 -16.79	-7.52 -16.41	-8.36 -17.29

Table III.4.2 Main parameters of the 7x7 phased array compared to the reference benchmark for the three scanning angles at central frequency.

In the next Figures (III.4.15-III.4.16) the beam efficiency and the Front to Back efficiency have been calculated for the 7x7 MTS array antenna and compared to the benchmark array at broadside and at the maximum scanning angle for E- and H-plane. The beam efficiency is calculated by means of the eq(III.4.1) as a function of the frequency. Figure III.4.16 represents how much power is radiated with respect to the back radiation. For these

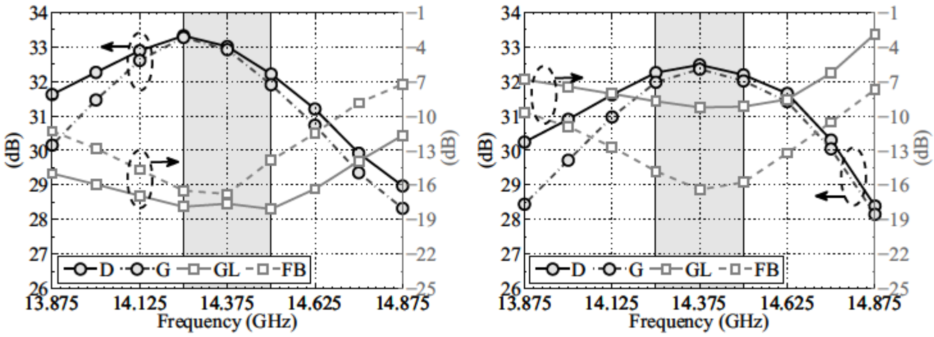

(a) MTS array at broadside

(b) MTS array at $\theta = 8.6deg$ in the H-plane

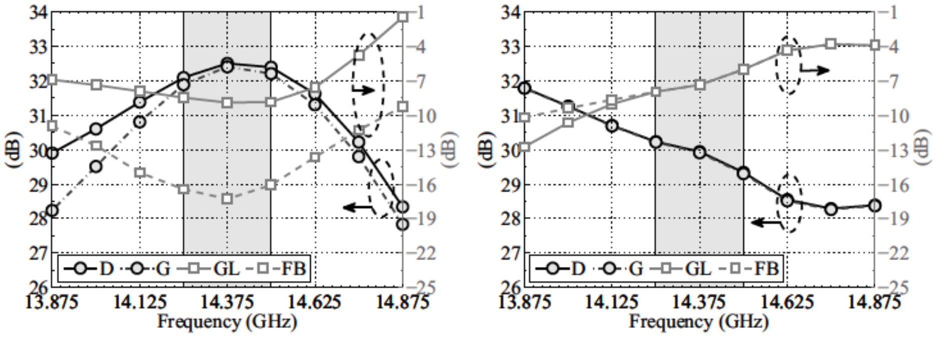

(c) MTS array at $\theta = 8.6deg$ in the E-plane

(d) Benchmark array at broadside

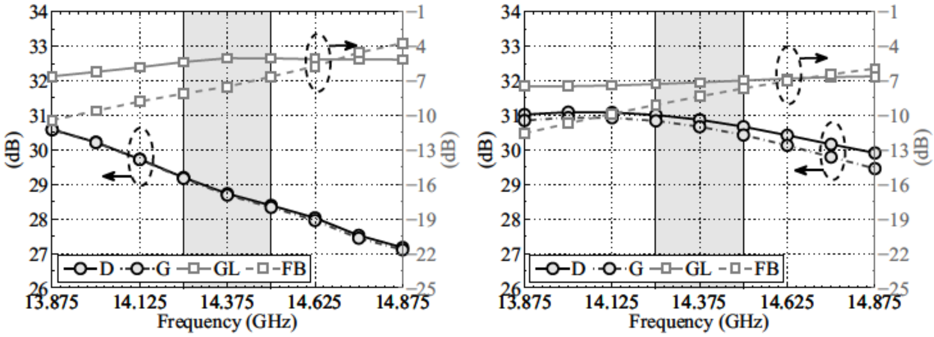

(e) Benchmark array at $\theta = 8.6deg$ in the H-plane

(f) Benchmark array at $\theta = 8.6deg$ in the E-plane

Fig. III.4.14 Frequency analysis for the main parameters: directivity (D), gain (G), grating lobe (GL) and front to back ratio (FB). D and G must be read on in the left side axis whilst GL and FB are represented on the right axis.

Figures the band of interest is also highlighted in gray.

$$BE = \frac{\Omega_{MB}}{\Omega_A} = \frac{\int_0^{\theta_1}\int_0^{2\pi} U(\theta,\phi) sin\theta d\theta d\phi}{\int_0^{\pi}\int_0^{2\pi} U(\theta,\phi) sin\theta d\theta d\phi} \tag{III.4.1}$$

Where Ω_A is the antenna solid angle (integral of the normalized power pattern over 4π stereoradians) and Ω_{MB} is the solid angle of the main beam up to the first nulls in the beam pattern (integral of the normalized power pattern over the main beam). θ_1 is the angle for the first null and $U(\theta,\phi)$ is the radiation intensity (power per unit solid angle).

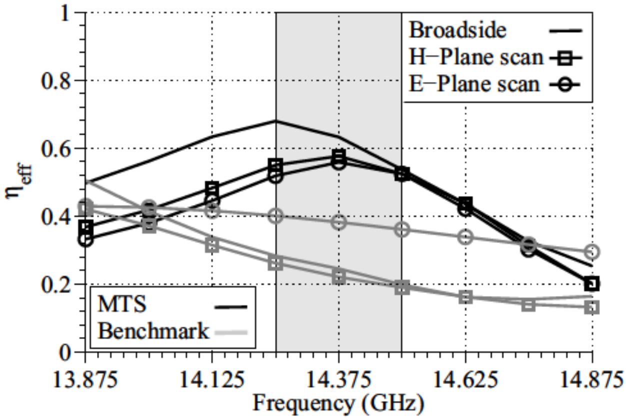

Fig. III.4.15 Beam efficiency as a function of the frequency (at broadside and at the maximum scanning angle of θ=8.6*deg* in the H and E-planes). In dark-lines is represented the MTS array design and in gray-lines the reference benchmark array antenna. The solid-line represents the beam efficiency at broadside whilst square-line is the scan in the H-plane and the circle-line is the scan in the E-plane.

From these two Figures (III.4.15 and III.4.16) we can conclude that the MTS array presents a better beam efficiency and front to back efficiency on the band of interest (gray area) with respect to the reference benchmark composed of sub-arrays.

Our study has demonstrated that a reduction of the grating lobes and an improved gain of the sparse array radiation pattern are possible thanks to the angular filtering introduced by a Fabry-Perot cavity.

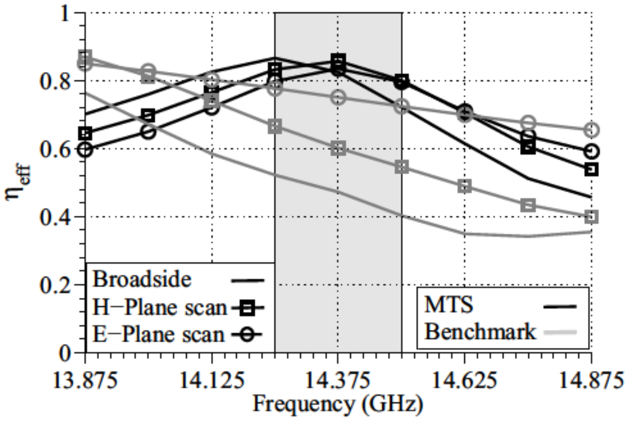

Fig. III.4.16 Front to Back efficiency as a function of the frequency (at broadside and at the maximum scanning angle of $\theta=8.6deg$ in the H and E-planes). In dark-lines is represented the MTS array design and in gray-lines the reference benchmark array antenna. The solid-line represents the front to back efficiency at broadside whilst square-line is the scan in the H-plane and the circle-line is the scan in the E-plane.

Chapter III.5

Leaky Wave Phased Arrays for Isoflux Applications

In this chapter we show how LWAs can also be used to synthesize isoflux patterns of special interest in satellite applications. The main challenge in this preliminary study was the design of phased arrays in combination with LWAs that scan at very large pointing angles following an isoflux mask.

III.5.1 Isoflux Applications

There is an increasing interest in antennas that scan over a large coverage area. These antennas are used in satellite applications that are normally located at low orbits. The radiation patterns of such antennas should compensate the losses caused by the large scanning and the different attenuation due to a different covered distance. Some examples of solutions have been reported in the literature as for instance in [123] where simulation results with a choke antenna are presented reaching almost $5dB$ of compensating losses when pointing to $40deg$. Other interesting work is presented in [124] where again a choke antenna is successfully measured reaching a $3dB$ of compensating losses for $63deg$ with $12dB$ of cross-polarization level. On the other hand [125] shows a printed design using the FSS concept, which compensates almost $5dB$ pointing to $50deg$ and keeping the cross polarized field below $13dB$ in the x-band. In this section we will show a new approach based on the use of partially reflecting surfaces *PRS* or Fabry-Perot cavities to compensate the losses for large pointing angles.

A PRS is used to create a leaky wave radiating at large angles (i.e. 50-60deg). The goal is to design an antenna that distributes a uniform power density over a very large angular region called *isoflux pattern* compensating the EOE (Edge of Earth) propagation losses as well as the pointing losses.

All of the previous isoflux antenna designs have been based on large apertures to get the isoflux profile and consequently they can not be used in a phased array configuration. In contrast the new design proposed here uses a *PRS* to create the isoflux profile and small antennas as feeders. This opens the possibility to extend the compensation of propagation losses to phased arrays.

In this application the inter-element distance will be smaller than in the previous Chapter and the distribution of the array elements will be in the form of a triangular lattice. We will show the performance of an array of 11x11 elements assuming linear polarization. The main specifications given by EADS/CASA for this design are described in table III.5.1.

Scenario 2	
Pointing angle	θ= 65deg to 70deg
Inter-element spacing (patch)	$0.5\lambda_0$ and $0.7\lambda_0$
Frequency Band	X-band and Ka-band
Element distribution	Triangle lattice
Phase and amplitude control	6 bits (amplitude and phase)
Polarization	Linear or circular

Table III.5.1 Summary of the desired requirements.

Considering the previous table we assume that the reference scenario is an array antenna that will be located on a LEO satellite (i.e. 160-2000 Km). Therefore, if all the angles have the same importance the best solution would be to radiate the power in an homogeneous distribution for the complete angular range. Hence, the antenna should counterbalance the propagation losses enlarging the gain towards the directions where the path is longer (Figure III.5.1).

In accordance with Figure III.5.1 the relation between satellite to Earth distance is [125]:

$$R_e^2 = R^2 + (R_e + h)^2 - 2R(R_e + h)cos(\theta) \qquad \text{(III.5.1)}$$

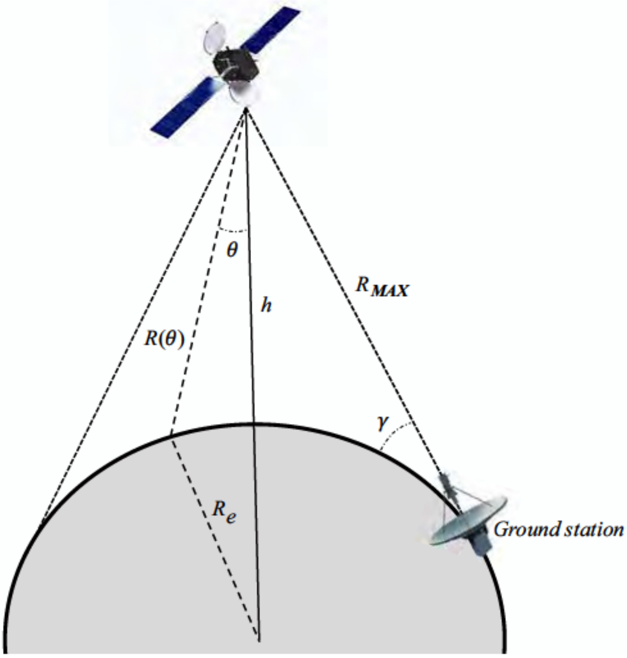

Fig. III.5.1 Geometrical description of a LEO satellite communication scenario.

The gain profile to provide an homogeneous power density on ground is:

$$G(\theta,h) = \frac{4\pi g^2(\theta,h)}{\int\int_{\Omega} g^2(\theta,h)d\Omega} \tag{III.5.2}$$

where:

$$g(\theta,h) = \begin{cases} |cos\theta|\sigma - \sqrt{1-\sigma^2 sin^2\theta} & \text{for } \theta < \theta_e \\ 0 & \text{for } \theta > \theta_e \end{cases} \tag{III.5.3}$$

where $R_e \cong 6371km$, $\sigma = (1+R_e)$ and $\theta_e = sin^{-}1(1/\sigma) - \gamma$. The minimum angle ($\gamma$) to see the satellite from the ground station is considered about $7deg$ for the minimum LEO satellite height h (i.e. 160 km). For satellite altitudes between 160 and 320 km the relevant isoflux patterns are shown in Figure III.5.3.

III.5.2 Design of an Isoflux LWA

Isoflux patterns can be obtained using a leaky wave antenna with a pointing direction of θ_e (the angle at which we want to compensate the propagation losses or the maximum scanning angle). To this aim, a uniform LWA with several dielectric layers or MTS's can be used. The geometry of the proposed structure is shown in Figure III.5.2.

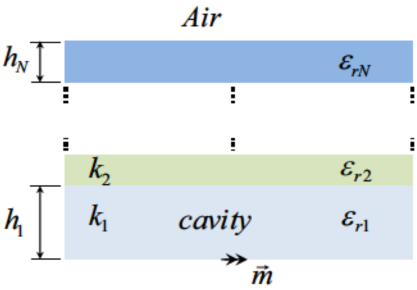

Fig. III.5.2 Geometry of the super-layer design.

In order to have a leaky wave pointing towards θ_e with a PRS structure, according to [6] the height of the cavity (n=1) and super-layers (n>1) when pointing at an angle must be:

$$\begin{aligned} h_1 &= \frac{\lambda_0}{2\sqrt{(\varepsilon_{r1} - sin^2(\theta_e))}} \\ h_{n>1} &= \frac{\lambda_0}{4\sqrt{(\varepsilon_{rn} - sin^2(\theta_e))}} \end{aligned} \tag{III.5.4}$$

The height of the cavity mainly controls the pointing angle and the heights of the super-layers controls the directivity of the pattern. However these heights must be optimized in order to obtain the desired radiated field (because these equations do not have into account the maximum compensation respect to broadside, symmetry of the patterns, etc.). As the final shape of the radiated fields depends on the super-layer structure, it is also very convenient to use a source with low directivity (i.e. apertures around $0.5\lambda_0$). After obtaining the radiation pattern, the dispersion equation of the structure has to be solved to verify if the design is feasible. Solving the dispersion equation enables us to know if surface waves are created (and its propagation constant value) and if the attenuation constant of the leaky wave leads to practical cases (i.e. meaning that those constants can not be too small as values close to zero imply too large antennas).

The first step in our optimization method is to choose the number of layers (N) and use the design equation (III.5.4) to calculate the initial values of the heights (seed) for arbitrary values of the permittivity. After that the radiated fields are calculated through the Green's function from the equivalent transmission line model of the layered structure (see Appendix B). This calculation is carried out with a Matlab home-made code for a small antenna (i.e. diameter $d \leq 0.6\lambda_0$). The calculated fields are optimized in order to follow a desired angular mask. A cost function can be used to adjust the radiated fields to the desired mask, as it is explained in the following section.

Cost Function The goal is to point to a large angle θ_e whilst the isoflux pattern exceeds a lower limit on broadside. Figure III.5.3 shows the main distances that must be minimized in order to obtain an arbitrary mask filter. Our mask has been adjusted according to the values in Table III.5.1.

The pattern to optimize is desired to be as symmetrical as possible. We consider a maximum difference between the E- and H-planes of 1dB at the maximum scanning angle. The cost function is composed of:

C_1 :The distance ⓐ should be close to zero if the E- and H-planes have a radiation pattern pointing out to θ_e.

C_2 :The distance ⓑ is related to the maximum distance at broadside in the region ranged between $-\theta_e <= \theta <= \theta_e$, θ in degrees. This distance/value is considered to be acceptable if it is around $5dB$.

C_3 :The distance ⓒ is related to the $roll-off$ in the transition region (gray) and should be as large as possible.

Moreover, the mathematical description of the cost function is as follows:

$$\begin{aligned} \underset{i}{\text{minimize}} \quad & f(i) = k_i C_i = k_1 C_1 + k_2 C_2 + k_3 C_3 \\ \text{subject to} \quad & ||E_{max}^{TM}| - |E_{max}^{TE}|| \leq 1dB, \end{aligned} \tag{III.5.5}$$

Depending on the application we can control the constant k_i in order to emphasize a specific region of the pattern. In our design, for example, we primarily focus on the cost function C_1 and the constraint $||E_{max}^{TM}| - |E_{max}^{TE}|| \leq 1dB$.

Single Antennas

We present first a full study of a single antenna with linear polarization. This element is composed of a Fabry Perot cavity excited by a circular printed antenna (i.e. double slot an-

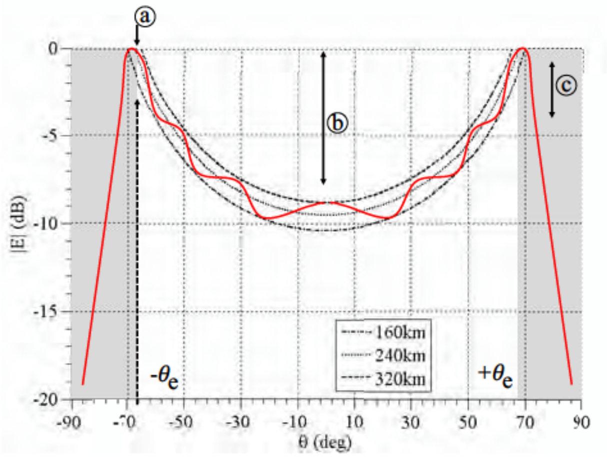

Fig. III.5.3 Objective function for a satellite ranging from 160km to 320km. The red line shows the mask. θ_e represents the maximum scanning angle.

tenna with radius of $0.3\lambda_0$, see Figure III.5.10.a) and four layers will be used (N=4 according to Figure III.5.2). This study has been made using a Matlab home-made code.

When using more than two layers the number of degrees of freedom is larger which enables us to achieve masks like the one shown in Figure III.5.4. This Figure shows one of the various masks that can be achieved with this type of structures. The main parameters used in this design (henceforth $isoflux_1$) are presented in Table III.5.2

ε_{r1}	1.41	h_1	$0.57\lambda_0$
ε_{r2}	16.22	h_2	$0.06\lambda_0$
ε_{r3}	2.83	h_3	$0.08\lambda_0$
ε_{r4}	2.32	h_4	$0.11\lambda_0$

Table III.5.2 Main parameters of the $isoflux_1$ design.

The interesting part of the mask presented here is that the solution of the dispersion equation shows that the values of the propagation vector are properly feasible. That means that the attenuation constant is not too small (i.e. $\alpha/k_0 > 0.01$). In Figure III.5.5 we can see the dispersion equation for the TM_0 mode as a function of the propagation vector. There it can be seen that there is a surface wave close to $\beta/k_0 \approx 1.20$. The exact values of the propagation vector are shown in the Figure III.5.6, where the real and imaginary parts of the

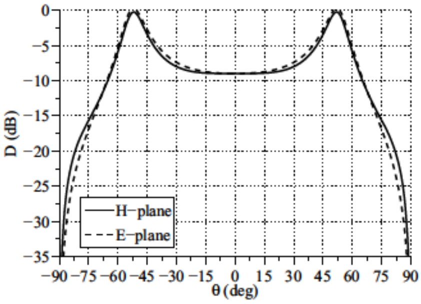

Fig. III.5.4 $Isoflux_1$ design shows a flattered shape at broadside, a $9dB$ of compensating losses at $50deg$, a very good roll-off at angles greater than $50deg$ and symmetric H and E-planes.

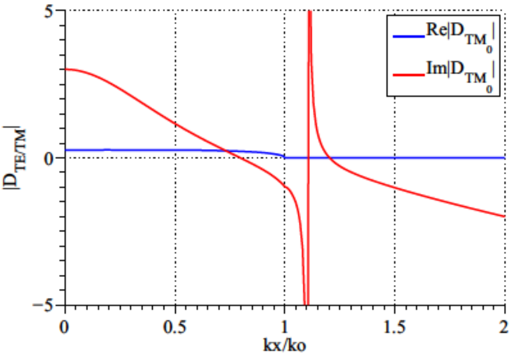

Fig. III.5.5 TM_0 modes of the dispersion equation as a function of the normalized leaky wave wavevector.

LW-vector are solved for the TM/TE modes as a function of the frequency.

The values of the propagation vector are summarized in Table III.5.3.

$k_p(TE)$	$0.80-0.06i$
$k_p(TM)$	$0.80-0.06i$
$k_p(TM_0)$	1.20

Table III.5.3 Leaky wave wavevector at central frequency for $isoflux_1$ design.

As shown in the table above, there exists a value of the propagation constant which is related to the surface wave (i.e. $k_p(TM_0) = 1.20$). However, as demonstrated in previous studies this surface wave can be attenuated introducing a null value in the spectral function

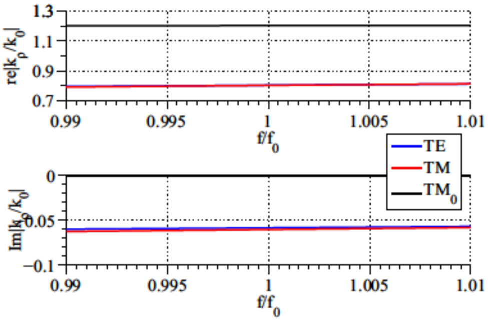

Fig. III.5.6 Dispersion equation values of the $isoflux_1$ design. A notable difference can be appreciated between the TE and TM attenuation constant.

using as excitation a double slot with an approximate distance of $\lambda_{TM_0}/2$.

The operating frequency bandwidth of the antenna depends on the variation of the leaky wave propagation constant with the frequency. In order to have a smaller variation in the propagation constant of the main modes (TM and TE), a new design can be made with a smaller values of permittivity in the superlayers. The main parameters used in this second design (henceforth $isoflux_2$) are presented in Table III.5.4.

ε_{r1}	1.24	h_1	$0.6\lambda_0$
ε_{r2}	8	h_2	$0.1\lambda_0$
ε_{r3}	1.7	h_3	$0.09\lambda_0$
ε_{r4}	3.5	h_4	$0.06\lambda_0$

Table III.5.4 Main parameters of the $isoflux_2$ design.

Figure III.5.7 shows the radiated fields in the main E and H planes for this second design.

In Figure III.5.8 we can see the dispersion equations for the TM$_0$ mode as a function of the propagation vector. There it can be seen that there is a surface wave close to $\beta/k_0 \approx 1.07$. The exact values of the propagation vector are shown in Figure III.5.9, where the real and imaginary parts of the LW-vector are solved for the TM/TE modes as a function of the frequency.

The values of the propagation vector for the $isoflux_2$ design (at central frequency) are presented in Table III.5.5.

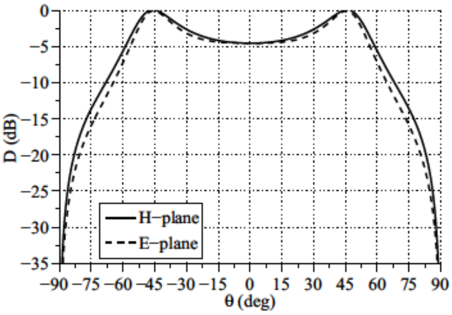

Fig. III.5.7 $Isoflux_2$ shows a flattered shape at broadside, a $5dB$ of compensating losses at $50deg$, good roll-off at angles greater than $50deg$ and symmetric H and E-planes.

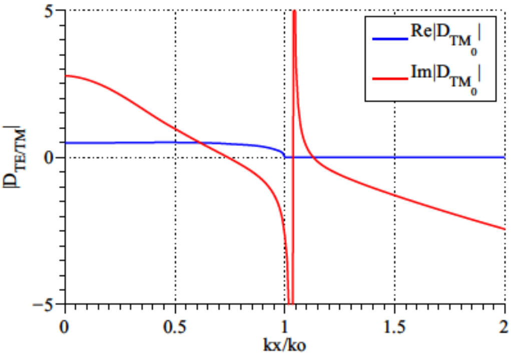

Fig. III.5.8 TM_0 modes of the dispersion equation as a function of the normalized leaky wave wavevector.

$k_p(TE)$	$0.74-0.10i$
$k_p(TM)$	$0.76-0.125i$
$k_p(TM_0)$	1.07

Table III.5.5 Leaky wave wavevector at central frequency for the $isoflux_2$ design.

CST validation of the multilayer dielectric designs

Regarding the validation with the full wave simulator CST [95] we consider a single antenna element which is a dielectric superlayered structure over a printed double-slot design (see Figure III.5.10). The dielectric structure is composed of four layers of which one is the antenna cavity and three are the dielectric superlayers. The simulated structure has a circular geometry with a radius of $15\lambda_0$ to reduce the non-coherent interference from the edges

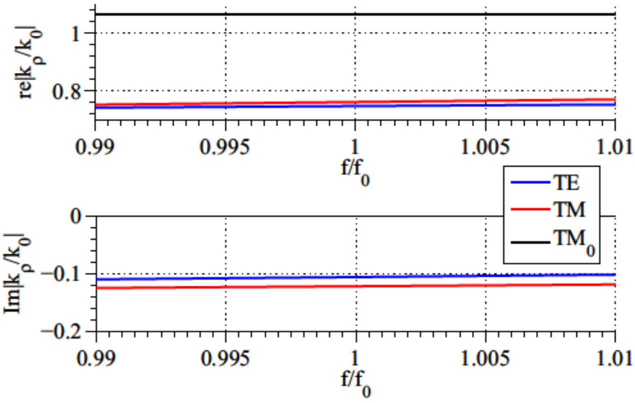

Fig. III.5.9 Dispersion equation values of the $isoflux_2$ design. A notable difference can be appreciated between the TE and TM attenuation constant.

associated to the residual surface wave. Figure III.5.10.a also shows that an absorber at the edge of the circular aperture is added in the simulations to suppress the residual edge radiation. In Figure III.5.10.b the basic printed antenna (superior view) is also shown. It consists of a couple of semi-circular slots fed with a stripline. As mentioned, these slots at a distance of $\lambda_{TM_0}/2$ help to reduce the surface wave. The circular cavity is limited by vias which eliminate the surface waves in the substrate and are located over a circle with a diameter of $0.6\lambda_0$. This surface wave is different from the SW excited in the cavity of the LWA. The angle α has been fixed at a value of $\alpha = 44deg$. Besides, a lateral view of the structure can be seen in the Figure III.5.10.c where the stripline feeds each slot and the ground plane (below the stripline) eliminates the back radiation.

The existence of the surface wave in the cavity of the LWA alters the radiation pattern while resulting in a power loss of the system. Figure III.5.11 shows the electric field inside the leaky wave cavity. We can see that the field attenuates along the radial direction, and only some residual part of the field arrives to the absorber, mainly around the $45deg$ directions.

Figure III.5.12 shows the radiated field in the main planes for the $isoflux_1$ design. There we can see that the H-plane is compensating about 9dB whilst the E-plane almost 6dB. The pattern barely presents a ripple towards broadside. This ripple is the effect of the residual surface wave and will be increased when the absorber is removed. The difference between the main H- and E-planes of around 3dB in Figure III.5.12 respect to the theoretical fields shown in Figure III.5.4, is explained by the inclusion of the double slot iris. This comparison

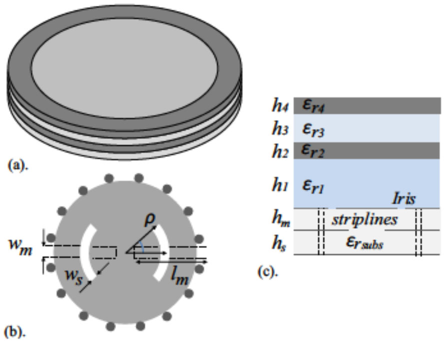

Fig. III.5.10 Parameters of the single antenna element: f_0 =8.2GHz. The diameter of the aperture is fixed to $0.6\lambda_0$ and it is limited by vias. The diameter distance between the slots is set to $d = 2\rho = \lambda_{TM_0}/2$ for each design.

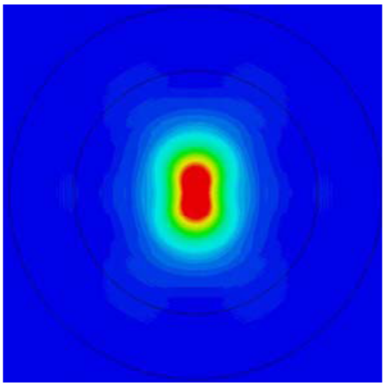

Fig. III.5.11 Aperture fields inside the first cavity at $z = h_1/2$ for the $isoflux_1$ design with absorber.

is shown in Figure III.5.13. This iris reduces the surface wave in the cavity layer (and thus the ripple) but also reduces the maximum directivity at the E-plane.

A sensitive fact over this kind of structures is that the attenuation constant is inversely proportional to the maximum scan angle (i.e. for broadside is around $\alpha/k_0 = 0.15$ and for $50deg$ its value is around $\alpha/k_0 = 0.05$), this means that larger pointing angles require larger antenna in order to attenuate the leaky wave. When the absorber is removed we must find the optimum length of the antenna in order to reduce the reflections inside the cavity caused by the remaining surface wave. The dimension of the slots have also been changed to match the reflection coefficient. On the other hand, the calculated radiation efficiency is 96%.

Figure III.5.14 shows the fields inside the cavity whilst Figure III.5.15.a shows how

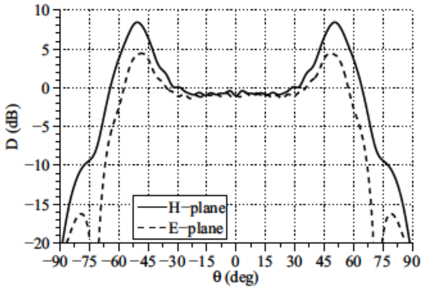

Fig. III.5.12 Radiated fields of the dielectric iris structure with absorber for $isoflux_1$ design. The distance between slots is $\frac{\lambda_{TM_0}}{2} = 0.83\lambda_0$ at $f_0 = 8.2GHz$.

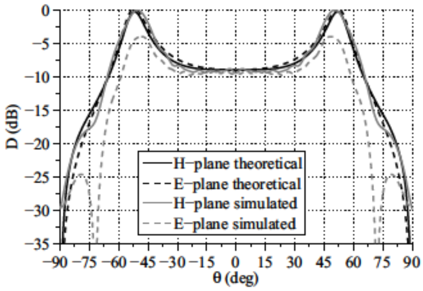

Fig. III.5.13 Radiated fields in the main planes for $isoflux_1$ theoretical versus simulated in CST.

the reflection coefficient has a good matching over only 4%. There we can see how the reflections increase without the absorber. These reflections impact the ripple of the radiated fields as seen in Figure III.5.15.b.

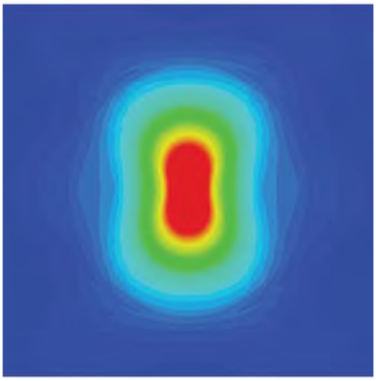

Fig. III.5.14 Aperture fields inside the first cavity $z = h1/2$ for the $isoflux_1$ design without absorber.

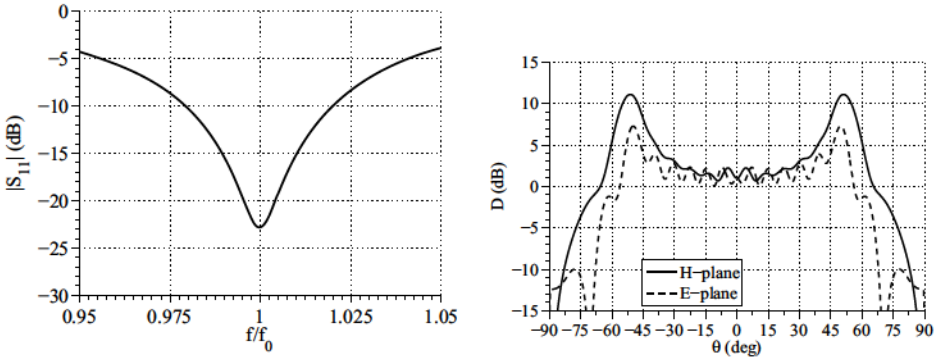

(a) Reflection coefficient

(b) Radiation pattern

Fig. III.5.15 Reflection coefficient and radiated fields in the main planes for the $isoflux_1$ design without absorber.

The frequency behavior of the $isoflux_1$ design is shown in Figure III.5.16. This Figure presents the variation of the radiation pattern in the main H- and E-planes. Here we show a band of 1GHz (7.7GHz-8.7GHz).

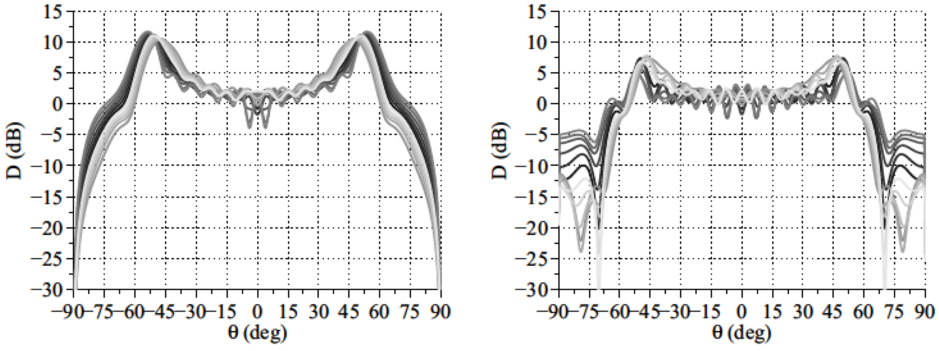

(a) Frequency behavior in the H-plane

(b) Frequency behavior in the E-plane

Fig. III.5.16 Frequency behavior of the radiated fields in the main (a). H- and (b). E-planes for the $isoflux_1$ design without absorber. Here we show a band of 1GHz (7.7GHz-8.7GHz).

From these two Figures a variation of ±1dB and ±2dB in the main H- and E-planes, can be observed. For this frequency band the maximum variation of the pointing angle is $6deg$ for both planes. As the required band is around 4.9% (8-8.4GHz), this solution is suitable to be used in this scenario.

The validation on CST of the $isoflux_2$ design is shown in Figure III.5.17. As it can be seen the reflection coefficient is well macthed over a 5% of the frequency band as this design is less resonant than the $isoflux_1$. As well as for the $isoflux_1$ design the double slot iris impacts on the maximum directivity of the antenna in the E-plane. Despite this, the validated fields on CST agree well with the theoretical calculated fields.

For this design, the radiation efficiency is 99.6%.

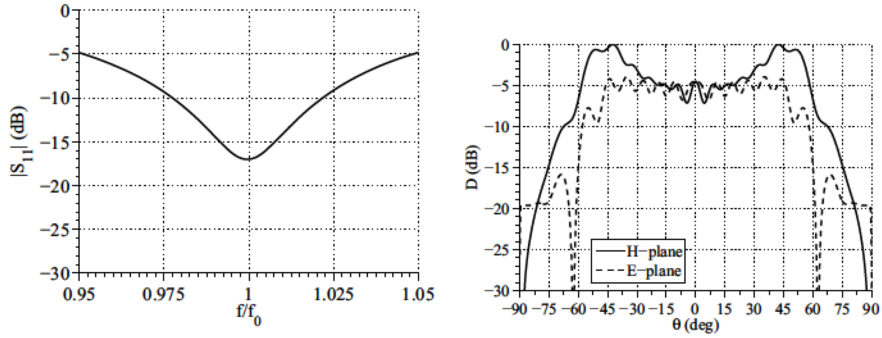

(a) Reflection coefficient

(b) Radiation pattern

Fig. III.5.17 Reflection coefficient and radiated field in the main planes for the $isoflux_2$ design without absorber.

III.5.3 Performance evaluation of isoflux LW phased arrays

As discussed in the preceding section it is possible to make an individual antenna where the field is radiating with isoflux profile. In the current section our goal is to known if an array made of those elements with a small inter-element distance would also be able to compensate the propagation losses.

The first thing we need to check is the embedded radiation pattern, as the small inter-element distance for sure will affect the isolated radiation pattern. To this aim the embedded pattern is obtained feeding the central element whilst the other elements of a 5x5 phased array are switched-off. The geometry used (an hexagonal lattice) in the active array is shown in Figure III.5.19.b and the inter-element distance has been fixed to $0.6\lambda_0$. Figure III.5.18a shows how the high level of mutual coupling impacts on the embedded pattern for the $isoflux_1$ design. This alteration in the radiated field is also increased by the high values of the permittivity of PRS that we have used in the multilayer structure. In Figure III.5.18a only around $3dB$ of compensation from broadside respect to the maximum scan angle (i.e. $50deg$) is achieved. This difference with the isolated pattern strongly depends on the inter-element spacing (i.e. $0.6\lambda_0$), and consequently it is not possible to reduce this negative effect on the radiated fields. In the $isoflux_2$ case we can not find a much better compensated embedded pattern (see Figure III.5.18b). On the contrary we can see around $2dB$ of losses in $50deg$ with respect to broadside, but the main planes are quite symmetrical.

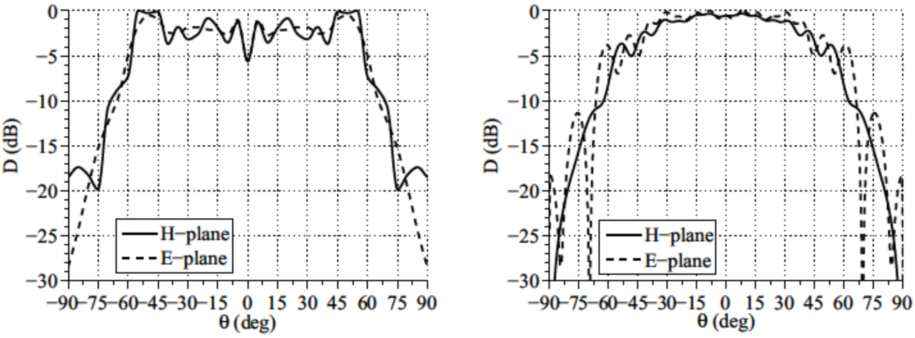

(a) $isoflux_1$ design (b) $isoflux_2$ design

Fig. III.5.18 Embedded pattern in the main E and H-planes for the $isoflux_1$ and $isoflux_2$ designs without absorber for a 5x5 phased array.

Scan Blindness and Grating Lobes In the array scenario, the scan blindness is an undesired effect related to the surface wave whilst the grating lobe is related to the inter-element distance and the lattice of the array. These two undesired effects can be seen in a spectral representation of the (k_x, k_y) (Figures III.5.20-III.5.23), where the solid line represents the grating lobe boundary (i.e. the parametric equation is $k_0^2 = k_x^2 + k_y^2$) whilst the dashed line represents the scan blindness boundary (i.e. with $k_\rho(TM_0)^2 = k_x^2 + k_y^2$). The gray circles represent the spectral distance to the other array elements (the number of gray circles depends on the array lattice). The representation on these figures is easy to understand, if there is an intersection of the gray circles with the dashed-line, this array configuration for this stratified media has scan blindness in the intersection angles. On the other hand, if the gray circles have also intersection with the solid lines, the array configuration has grating lobes in the specified angles.

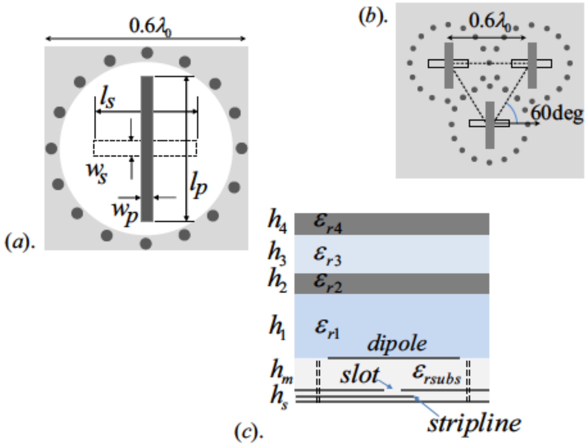

Fig. III.5.19 Main parameters of the basic reference antenna in a periodic scenario to calculate the active impedance. (a). periodic cell. (b). triangular lattice. (c). lateral view of layered structure. The length and the width of the dipole is $l_d = 10.56mm$ and $w_d = 0.68mm$ and for the slot $l_s = 13.07mm$ and $w_d = 0.75mm$ respectively. The permitivity of the susbtrates for the basic antenna (without taking into account the stratified media) is $\varepsilon_{rsubs} = 1.5$. The height of the susbtrate layer between the dipole and slot is $h_m = 3mm$ whilst the height of the substrate between the slot and the ground plane is $h_s = 1mm$. In the middle of the this last layer there is a stripline feeding the slot.

As the inter-element distance in the hexagonal lattice is small enough, there is not grating lobe in both $isoflux_1$ and $isoflux_2$ design (i.e. the gray circles do not have intersection with the solid line) as it can be seen in Figures III.5.21 and III.5.23. For the first $isoflux1$ design there is a surface wave for $\beta_{TM_0} = 1.2$ and the lower scan blindness angle appears at $\theta = 48.99$ $\phi = -30.33$ (see Figure III.5.20). For the second $isoflux2$ design there are not scan blindness angles intersecting the circle of diameter 1.07 (i.e. dashed line) due to the smaller propagation constant. This can be seen in Figure III.5.22. As there are not scan blindness angles for the $isoflux_2$, the geometry of the active array element does not have to include the double slot iris (the effect of the surface wave does not alter the radiation pattern). We have chosen a geometry simpler than the single element geometry (a dipole fed by a slot instead the double slot iris) and as it is shown in Figure III.5.19.

Active Array Performances

The active array performance of the $isoflux_1$ design, has resulted in poor matching of the active impedance and also in the existence of a scan blindness angle within the scanning angular range. These results for $isoflux_1$ design are omitted for brevity. For the $isoflux_2$

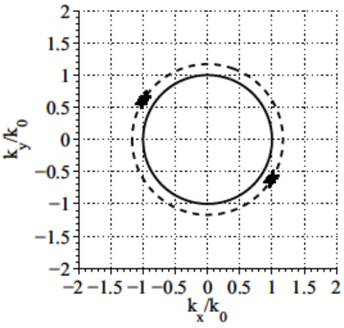

Fig. III.5.20 Scan blindness for $isoflux_1$ design.

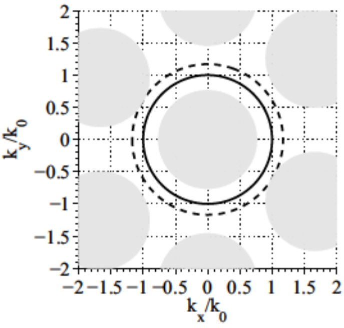

Fig. III.5.21 Grating lobe for $isoflux_1$ design.

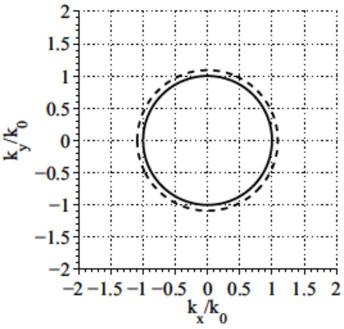

Fig. III.5.22 Scan blindness for $isoflux_2$ design.

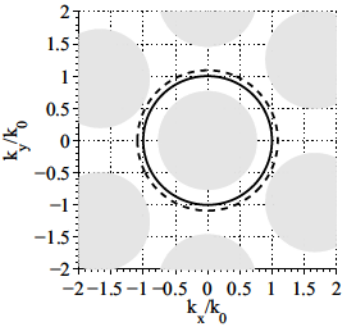

Fig. III.5.23 Grating lobe for $isoflux_2$ design.

design, we obtain a level of mutual coupling as it is shown in Figure III.5.24a. Although this level is more than -20dB and the embedded pattern is different from the isolated pattern it is not possible to reduce it because we cannot further increase the inter-element distance without adding grating lobes. Also in Figure III.5.24b, the active reflection coefficient of the 11x11 elements of a phased array at broadside are presented.

The active reflection coefficient of the 11x11 elements of a phased array for several scanning angles (detailed in the figure caption) are shown in Figure III.5.25. In all these scanning angles the active impedance presents a reasonably good agreement with the reflection coefficient of the isolated element considering the large scanning range.

The embedded pattern and the array radiation pattern for the selected scanning angles for the H-plane are represented all in the same Figure III.5.26. From this Figure, we can conclude that the isoflux array pattern follows the shape of the embedded pattern. This means

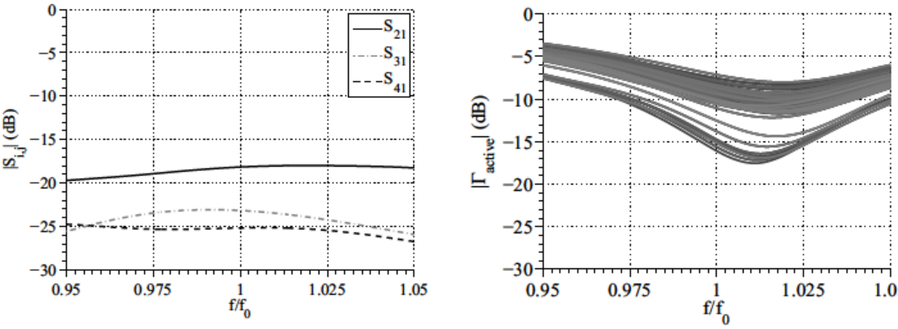

(a) Mutual coupling level

(b) Active reflection coefficient at broadside

Fig. III.5.24 Mutual coupling level for an 11x11 phased array and active reflection coefficients at broadside.

that if we want to compensate at larger angles, we have to analytically include the embedded pattern (in the array configuration) and optimize this instead of the isolated pattern as we have done here. This is a future line of this work.

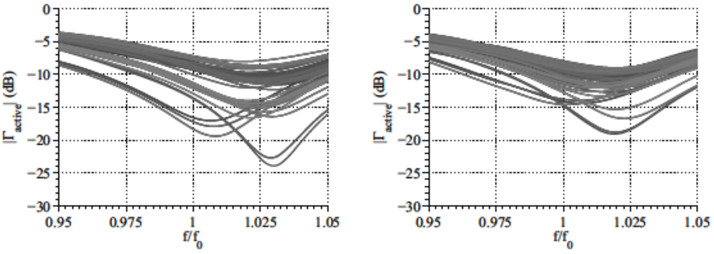

(a) $\theta = 15deg$ in the E-plane (b) $\theta = 15deg$ in the H-plane

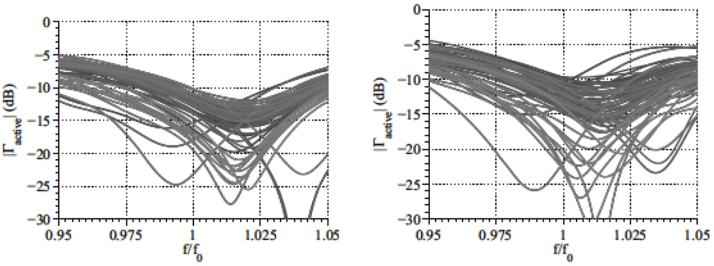

(c) $\theta = 30deg$ in the E-plane (d) $\theta = 30deg$ in the H-plane

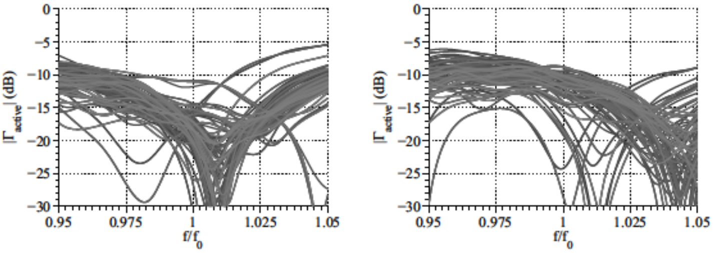

(e) $\theta = 45deg$ in the E-plane (f) $\theta = 45deg$ in the H-plane

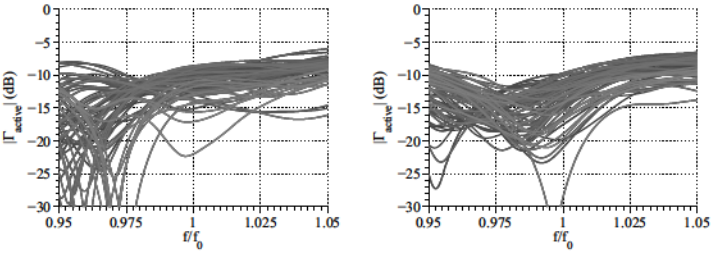

(g) $\theta = 60deg$ in the E-plane (h) $\theta = 60deg$ in the H-plane

Fig. III.5.25 Active reflection coefficients for an 11x11 phased array, in four different scanning angles at the two main planes.

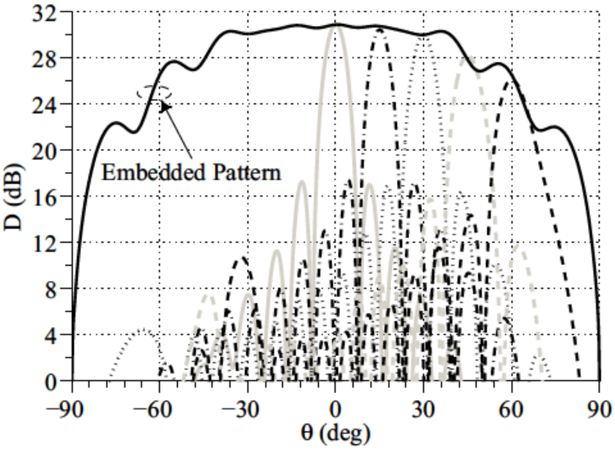

Fig. III.5.26 Embedded pattern and array radiation pattern at the different scanning angles for an 11x11 array.

Chapter III.6

Concluding Remarks

Firstly, in this second part of the thesis we have rigorously compared the performances of LWAs based on dielectric superlayers with LWAs based on inductive and capacitive MTS by imposing an equivalence in terms of the fundamental TE/TM modes. This equivalence ensures that the three antennas have comparable frequency bandwidths and levels of mutual coupling if they were to be used in array configurations. We have found the inductive MTS to be the best performing solution since it leads s a higher roll-off of the radiation pattern as a consequence of the intrinsic suppression of the radiation from the spurious TM leaky-wave mode. This suppression is demonstrated rigorously with simple and controllable closed form formulas. Numerical full wave analysis and experiments have confirmed the theory showing an improved gain of more than 1dB with the same frequency band of operation. This improvement is especially interesting for its use in thinned phased arrays and single beam focal plane arrays at ka-band satellite applications.

Secondly it has also been shown how the highest gain of thinned arrays integrated with dielectric superlayers acting as angular filters of the grating lobes is obtained when the mutual coupling levels are in the order of -20dB. By considering the single antenna radiation pattern, one can conclude that the use of larger dielectric constant allows a higher roll off and therefore larger grating lobe attenuation. However the impact of the increased mutual coupling limits the theoretical achievable attenuation and reduces the array gain. As an example we have designed enhanced phased array with a dielectric constant of ε_r=8 showing a 2.2dB increased gain over the whole 5% frequency band and the considered scanning range, with respect to a conical horn phased array. This enhanced phased array with a periodicity of $1.5\lambda_0$ presents grating lobe values lower than 10dB with respect to the maximum at the edges of both the scanning range and the frequency band.

Thirdly we have presented a practical implementation of a leaky wave thinned phased array with enhanced scanning properties. Our study demonstrates that a reduction of the grating lobes and an improved gain of the sparse array radiation pattern are possible thanks to the angular filtering introduced by a Fabry-Perot cavity. The presented array was made in PCB technology and integrated with an inductive MTS superlayer. A full study of the performances of the 7x7 phased array antenna for several scanning angles is presented and compared with a reference solution based on 2x2 sub-arrays. This study shows the improved gain, directivity, grating lobe level, side lobe level, front to back ratio and beam efficiency as a function of the frequency for the leaky wave enhanced phased array.

Finally, we have designed leaky wave antennas with isoflux radiation patterns, based on the use of multilayer structures. After that due to the simple geometry of PRS and the small size of the elementary antenna, this isoflux concept has been easily extended to array configuration using the two designed individual antennas. With a proper design (i.e. a small interelement spacing must be chosen, in our case $0.6\lambda_0$ in an hexagonal lattice) the grating lobe and the scan blindness are avoided in the scanning range (i.e. $-50deg \leq \theta \leq 50deg$). As a consequence of this small interelement spacing, the active impedance is mismatched for large incident angles. Moreover the mutual coupling has also a strong negative impact on the embedded patterns and the isoflux concept has not been successfully demonstrated for a phased array. In the future, a new study must be done in order to find how to minimize the mutual coupling. This can be done by modifying the optimization tool in order to include the impact of the mutual coupling in the embedded pattern.

Part IV

Conclusions and Future Lines

Conclusions

Along this PhD dissertation, different leaky wave antenna solutions have been investigated with the purpose of providing new designs with improved performances for different scenarios. Considering this, the thesis covers two important topics, one oriented to antennas that provide focusing in the near-field (periodic LWAs) and the other to far-field designs mainly related to array configuration for space applications (uniform LWAs).

The first topic is adressed in Part I of the thesis. There the proposed novel holographic antenna opens to a new variety of microwave focusing devices which are highly efficient, extremely simple, and low-cost, and that provide the interesting capability of frequency adjustment of the focal length (steering). This interesting frequency response has been accurately and efficiently predicted by the proposed theory for modulated leaky modes, and it might be useful for microwave imaging, sensing and heating applications. Compared to electronically scanned focused antennas, frequency scanning provides a much simpler mechanism to steer the focus and with a very reduced cost. The method reported here (Chapter 3) directly synthesizes the radiated fields from the arbitrary fields imposed over the antenna aperture. The computational cost of the dispersion matrix is equal for any size of the antenna making this method suitable for large antennas. A more symmetrical focal region is demonstrated for radially-polarized antennas compared to the circularly-polarized antennas. This characteristic is studied as a function of the Fresnel Number. This method has the drawback that does not allow a good control of the polarization because of the use of a continuous slit instead of several discrete perpendicular slots, and as a result specially the transversal-circular polarization is rigorously obtained only on the antenna axis. The methodology was used to design, manufacture and measure two prototypes that are able to focus in near-field, one with transversal-circular polarization and another one with radial polarization. Both of them present good agreement between the theoretical and experimental results.

The second important topic afforded on this work deals with far-field applications and it is addressed in Part II. Particularly the capability of this kind of antennas to do far-field beam shaping is analyzed. Initially different types of PRS were studied (inductive, capacitive and dielectric), demonstrating that inductive strip grid based MTSs allow to obtain the more directive radiation pattern because they do not support the propagation of the TM_0 spurious mode. A study of the main radiation parameters in the frequency bandwidth is conducted. All results have been verified by the fabrication and measurement of two prototypes (dielectric slot and inductive strip grid based MTS LWA). Afterwards dealing with array applications, we have studied how the mutual coupling in arrays made with this type of antennas impacts the active impedance and the roll off of the embedded patterns. These LWAs were used as array elements to achieve the grating lobe angular filtering in a phased array leaky wave antenna. We showed that antenna elements based on dielectric superlayers leading to mutual coupling levels smaller than -20dB do not suffer from a significant loss of directivity in the embedded pattern or a loss of gain in the phased array.

These two previous ideas (inductive strip grid based MTS does not support the TM_0 spurious mode and the maximum mutual coupling should be less than -20dB) were combined to design a thinned LW phased array in PCB technology for angular filtering using an inductive strip grid based MTS as PRS. This design demonstrated higher performance of this antenna respect to the classical array composed of subarrays. The results were presented for several scanning angles in the entire frequency band. The specifications for this design were given by the research project [1] funded by EADS CASA. Two prototypes to verify this results are currently in manufacturing process.

At the end of Part II we also demonstrate that it is possible to design isoflux antennas with a small basic antenna as a feeder and adding a Fabry-Perot cavity. Several designs for array element have been presented, and full wave simulations have been successfully reported showing quite symmetrical fields with the main lobe pointing towards large angles. The challenge in this preliminary study was to point at large angles, trying to do the isoflux mask of a phased array with a LWA. To solve this issue a substrate different to air had to be used in the Fabry-Perot cavity. Unfortunately, this allows the propagation of surfaces waves (SW) inside the cavity, that will destroy the performance in array scenario.

In all the presented designs, due to the large scanning range the interlement distance was less than λ_0 and as a consequence, the active impedance is very hard to match and the mutual coupling has a strong impact on the embedded pattern. Nevertheless, some interesting results have been also obtained in this final part of the Thesis.

---

[1] "Diseño de Agrupaciones de Antenas con Filtros Angulares Realizados Mediante Estructuras Periódicas Selectivas en Frecuencia", EADS CASA ESPACIO (ECE), 2012-2013

Future Lines

There are many opportunities for extending the work that has been developed along this Thesis. This section presents some of these possible future directions.

Concerning Part II of the Thesis, the work on holographic LWAs needs to be extended to find out a way to allow the arbitrary control of the polarization. This is not an easy task because both TE and TM modes should be modulated simultaneously instead of only the TEM mode. This can be addressed by increasing the substrate thickness so that both TE_1 and TM_1 can propagate. An appropriate combination of dipoles and slots to modulate these modes on the main azimuthally planes should be defined. Then a similar procedure for synthesis that the one developed in this thesis (i.e. Chapter II.2) could be applied.

A second line of research, related to some of the results of Part III, in particular to Chapter III.2, is to investigate more complex geometries of MTS, to be used with circularly polarized feeds or even to create circularly polarized fields from a linearly polarized source by using the geometry of the FSS. It will be also of interest to design other more complex MTS that does not support the spurious TM_0 mode and can be used for other purposes: circular polarization, dual band or reconfigurability.

May be one of the most important research lines opened after the thesis is to study how to reduce the mutual coupling between elements in a phased leaky wave array. This will allow the use of more reflective PRSs in order to increase the directivity without a considerable loss in the bandwidth. Even more this reduction in the mutual coupling would be also very useful to improve the results of Chapter III.5. One of the designs shown in that chapter presents a good matching for all the scanning angles but the strong mutual coupling impacts on the embedded pattern and the design loses the good performance of the isolated pattern. It must be taken into account that in these isoflux designs the inter-element distances can not be increased due to the grating lobes and the large scanning angles. Other possible alternative, for isoflux array designs will be to considered to replace the dielectric super-layer by MTSs.

Appendix A

Holographic Antenna Synthesis

In this appendix we present how to synthesize holographic antennas (as the ones studied in Part II) using an optimization procedure derived from the solution of the dispersion equation. This methodology presented here allows the synthesis in a discrete geometry of any arbitrary field distribution (as the ones shown in Chapters II.3 and II.4). These fields are focused on the near-field with circular or radial polarization. As it was described in Chapter II.2, we first have to define some parameters to synthesize an arbitrary field (i.e. constants like the height h, permittivity ε_r of the substrate, the central frequency f_0, the radiation efficiency η_{eff}, etc.). Overall we have to build a matrix that relates the geometry (width of the slot or strip w and the period P, see Figure II.2.4) of the LWA with the propagation constant (attenuation α and phase β) for each point in the aperture of the planar antenna. We must first fix the period P, and change the slot's width w for several values and solve the dispersion equation. After that we update a different P and change w again in a range of values. In order to solve the dispersion equation we use a method of moments MoM as it is described in [18]. The result is a dispersion matrix that relates the physical geometry (P,w) with the LW propagation vector (α,β). At the end the dispersion matrix is interpolated in order to refine it for other values of P and w. After the generation of the dispersion matrix we perform an optimized search of the theoretical values on it.

A.1 Geometry Synthesis Algorithm

Lets summarize in detail the steps to synthesize a geometry with the following algorithm.

1. Obtain the dispersion matrix in a range of values for P,w. These values are related to

α and β (see Figure II.2.4). We have to obtain values with $0 \leq \alpha, \beta \leq 1$. The variation of P or w changes the value of α and β at the same time.

2. Create two functions @alpha and @beta that lead to know the theoretical values of α, β required over the aperture of the desired design (see eq II.2.5 and eq II.2.6). These two functions are function of the ϕ angle, the radius ρ and the arbitrary constants η_{eff}, Ln, etc.

3. Verify the maximum and minimum values of the dispersion matrix. These must be bounded by the theoretical boundaries of the design. We have to lock bang gap zones (forward or backward zones depend on the own design).

4. Interpolate the matrix in order to increase the resolution.

5. Generate the theoretical α and β (using @alpha and @beta) to initial values $\rho = Ro$ and $\phi = 0$.

6. Find the theoretical (α and β) in the dispersion matrix. To minimize the error, we can use a square function as:

$$\begin{aligned} \underset{x}{\text{minimize}} \quad & f_0(x) = (\alpha - a)^2 + (\beta - b)^2 \\ \text{subject to} \quad & |\beta - b| = error \end{aligned}$$

   Where "a" and "b" are the actual values in the dispersion matrix related to the geometrical structure (P, w). The error variable controls the accuracy in the radiation angle at the expense of the accuracy in the α variable (related to the radiation efficiency).

7. Obtain the best value for P, w associated to theoretical α and β that causes minimum error. After that, we have to update the angle ϕ. This variable contains the polarization's information of the design in the focal region. For example if the chosen polarization is circular the ratio ρ will be (for linear polarization this variable ϕ is discrete: $0, 2\pi, 4\pi ...$):

$$\rho(\phi) = R_0 + \lambda_{SW} \frac{\phi}{2\pi} \tag{A.1}$$

   Note: Because the algorithm is a function of ϕ the discretization process can be made as "*continuous*" as we like.

8. Repeat this process until the value of ρ reaches the maximum (i.e. maximum diameter of the design, *Ln*).

The most important consideration in this procedure is that the variation of ϕ represents small changes in α and β and consequently (P, w) will have smooth transitions. Figure A.1 shows how changes in ϕ represent an increase of ρ and ire responsible for the circular polarization (if ρ is constant, we have linear polarization). This procedure is easier to understand with the help of Figure A.1, where a spiral is drawn over the aperture as a consequence of the circular polarization. Red points over the spiral line are the angles where the procedure has been synthesized (in this case the spiral is more “continuous” for smaller values of ρ).

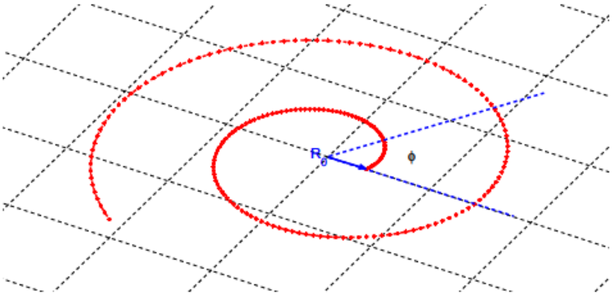

Fig. A.1 Spiral generated as a function of ρ and ϕ

Appendix B

Green's Function of Planar Stratified Dielectric Media

This appendix summarizes how to calculate the SGF associated to an arbitrary number of planar dielectric layers (stratified dielectric media) as well as the inclusion of a single MTS layer. This SGF is derived by solving the corresponding equivalent transmission line problem. The current and voltage generators of the transmission line are associated to elementary dipole or slot, respectively. This SGF is used for calculating the fields radiated by planar antennas in the presence of these stratifications as well as to impose the relevant dispersion equations.

B.1 Spectral Green's Function

The SGF is only reported here for the electrical field created by a magnetic or an electric current in a stratified media, for other cases see [18]. We consider the source oriented in the x or y direction and the stratified media is along z. As the SGF depends on line voltages and currents in the equivalent transmission line model, we consider a grounded slab (ε_r,h) as it is shown in Figure B.1. For both elementary sources z' represents the position of the source (in the first case $z' = 0$ and in the second one $z' = h$), and $k_p^2 = k_x^2 + k_y^2$.

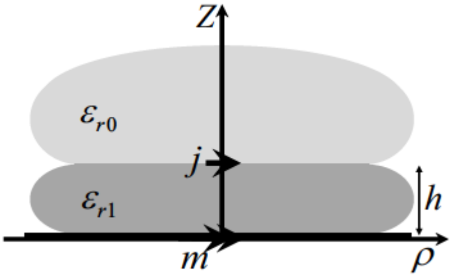

Fig. B.1 An electric source placed at the dielectric-air interface and a magnetic source at the ground plane of a grounded slab.

The expression of the Green's function in the spectral domain is:

$$g^{es}(x,y,z;x',y',z') = \frac{1}{2\pi^2}\int_{-\infty}^{\infty}\int_{-\infty}^{\infty} \underline{\underline{G}}^{es}(k_y,k_y,z,z')e^{-jk_x(x-x')}e^{-jk_y(y-y')}d_{k_x}d_{k_y} \tag{B.1}$$

Here the superscripts e represents the desired electric field and the source s can be a magnetic m or electric j current respectively. The dyadic SGF associated to electric **E** field when a magnetic current $\mathbf{m}(x',y',z')$ is considered as source is:

$$\underline{\underline{G}}^{em}(k_y,k_y,z,z') = \begin{bmatrix} \frac{k_xk_y}{k_p^2}({}^mV_{TM}(k_p,z,z') -{}^m V_{TE}(k_p,z,z')) & -\frac{1}{k_p^2}({}^mV_{TM}(k_p,z,z')k_x^2 +{}^m V_{TE}(k_p,z,z')k_y^2) \\ \frac{1}{k_p^2}({}^mV_{TM}(k_p,z,z')k_y^2 +{}^m V_{TE}(k_p,z,z')k_x^2) & \frac{k_xk_y}{k_p^2}({}^mV_{TE}(k_p,z,z') -{}^m V_{TM}(k_p,z,z')) \\ -\frac{k_y}{k_{z_i}}Z^m_{TM_i}I_{TM}(k_p,z,z') & \frac{k_x}{k_{z_i}}Z^m_{TM_i}I_{TM}(k_p,z,z') \end{bmatrix} \tag{B.2}$$

Where V_{TM}, V_{TE}, I_{TM}, I_{TE}, Z_{TM}, Z_{TM}, are the voltages, currents and impedances solution of the equivalent transmission line (see Figure B.2) as a function the TE and TM impedances ($Z_{TMi} = \eta\frac{k_{zi}}{k_i}$ and $Z_{TEi} = \eta\frac{k_i}{k_{zi}}$). The magnetic current is represented by a unitary series voltage generator.

The dyadic SGF associated to the electric **E** field when an electric current $\mathbf{j}(x',y',z')$ is considered as source is:

$$\underline{\underline{G}}^{ej}(k_y,k_y,z,z') = \begin{bmatrix} -\frac{1}{k_p^2}({}^jV_{TM}(k_p,z,z')k_x^2 +{}^j V_{TE}(k_p,z,z')k_y^2) & \frac{k_xk_y}{k_p^2}(-{}^jV_{TM}(k_p,z,z') +{}^j V_{TE}(k_p,z,z')) \\ \frac{k_xk_y}{k_p^2}({}^jV_{TE}(k_p,z,z') -{}^j V_{TM}(k_p,z,z')) & -\frac{1}{k_p^2}({}^jV_{TE}(k_p,z,z')k_x^2 +{}^j V_{TM}(k_p,z,z')k_y^2) \\ \frac{k_x}{k_{z_i}}Z^j_{TM_i}I_{TM}(k_p,z,z') & \frac{k_y}{k_{z_i}}Z^j_{TM_i}I_{TM}(k_p,z,z') \end{bmatrix} \tag{B.3}$$

In this case the electric current is represented by a unitary parallel current generator

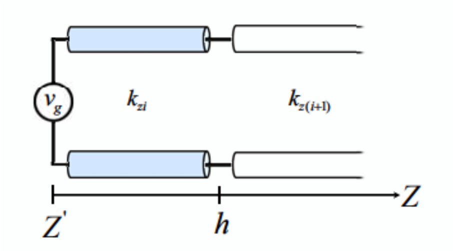

Fig. B.2 Equivalent transmission line to be solved for the case of a single stratification of height h above a ground plane: magnetic source.

placed at $z' = h$ (see Figure B.3).

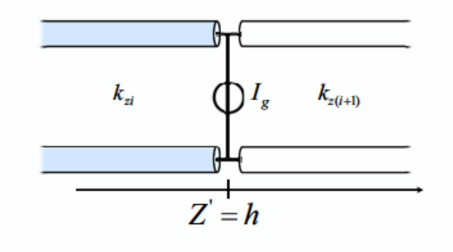

Fig. B.3 Equivalent transmission line to be solved for the case of a single stratification of height h above a ground plane: electric source.

B.2 Solutions of the equivalent transmission line

Using the circuit theory we can know the line voltage and current in any point of a stratified media as it is shown in Figure B.4.a. This is possible by imposing the adequate boundary conditions with the defined excitation source.

In the following steps we will show the process to solve n-layer dielectric and MTS structures.

B.2.1 N-Dielectric Layers

Consider an n-layered stratified media as it can be seen in Figure B.4a.

There $\lambda_0 = \frac{c}{f_0}$, $k_0 = \frac{2\pi}{\lambda_0}$, $\zeta_0 = 120\pi$, $\zeta = \frac{\zeta_0}{\sqrt{\varepsilon_r}}$, $k = k_0\sqrt{\varepsilon_r}$, $k_p = \sqrt{k_x^2+k_y^2}$ and $k_z = \sqrt{k^2-k_p^2}$, where k_z is the LW propagation vector that depends on (k_x, k_y). The modal

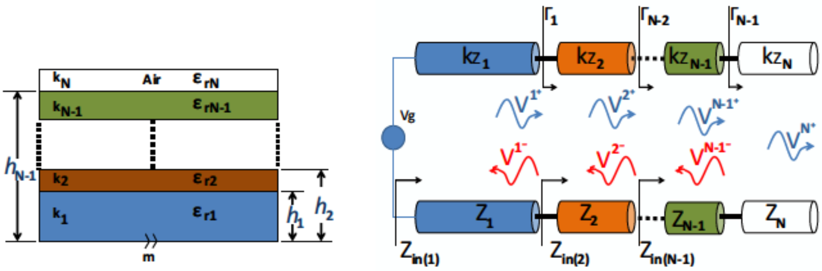
k_N
Air
ε_{rN}
k_{N-1}
ε_{rN-1}
h_{N-1}
k_2
ε_{r2}
k_1
ε_{r1}
h_1
h_2
m
Γ_1
Γ_{N-2}
Γ_{N-1}
kz_1
kz_2
kz_{N-1}
kz_N
Vg
V^{1+}
V^{2+}
V^{N-1+}
V^{N+}
V^{1-}
V^{2-}
V^{N-1-}
Z_1
Z_2
Z_{N-1}
Z_N
$Z_{in(1)}$
$Z_{in(2)}$
$Z_{in(N-1)}$

(a) (b)

Fig. B.4 (a). Geometry and (b). equivalent transmission line model of the dielectric stratified media.

impedance can be defined as $Z_{TM} = \zeta \frac{k_z}{k}$ and $Z_{TE} = \zeta \frac{k}{k_z}$. Now we can calculate the reflection coefficient in each section as a function of the characteristic impedances and input impedances:

$$\Gamma_{n-1} = \frac{Z_{in(n)} - Z_{n-1}}{Z_{in(n)} + Z_{n-1}} \tag{B.4}$$

In the case of n=N, $Z_{in(N)} = Z_N$ in other case, $Z_{in(n)} = Z_n \frac{Z_{in(n+1)} + jZ_n tan(kz_n h_n)}{Z_n + jZ_{in(n+1)} tan(kz_n h_n)}$. Reminding that $V^{N-} = 0$ and by Kirchhoff's circuit law, the line voltage and current in each layer assuming lossless media is:

$$^{m}V^{n}(k_p,z) = V^{n+}e^{-jk_{zn}z} + V^{n-}e^{jk_{zn}z} \tag{B.5}$$

$$^{m}I^{n}(k_p,z) = \frac{1}{Z_n}(V^{n+}e^{-jk_{zn}z} - V^{n+}e^{jk_{zn}z}) \tag{B.6}$$

The relation between incident and reflected wave allows to find:

$$V^{n-1^{-}} = \Gamma_{n-1} V^{n-1^{+}} e^{-j2k_{zn-1}h_{n-1}} \quad \forall n \quad 2 \leq n \leq N \tag{B.7}$$

At the end:

$$V^{1^+} = \frac{Z_1}{Z_{in(1)}} \cdot V_g \cdot \frac{1}{(1-\Gamma_1 e^{-j2k_{z1}h_1})} = V_g \cdot \frac{1}{(1+\Gamma_1 e^{-j2k_{z1}h_1})} \tag{B.8}$$

V^{1^-} is found with eq B.7. The voltage amplitude in the $n+1$ medium is obtained by imposing the continuity of the voltage solutions at $z = h_n$.

$$V^{n+1^+} = \frac{e^{-jk_{zn}h_n}}{e^{-jk_{zn+1}h_n}} \cdot \frac{(1+\Gamma_n)}{(1+\Gamma_{n+1}e^{-j2k_{zn+1}(h_{n+1}-h_n)})} \cdot V^{n^+} \tag{B.9}$$

Again V^{n+1^-} is found with eq B.7 and the complete incident and reflected voltage in the n-layer is found by eq B.6. Thus the final voltage and current as a function of the distance z is:

$$\begin{aligned} {}^{m}V^{N}(k_p,z) &= {}^{m}V^{N-1}(k_p,h_{N-1})e^{-jk_{zN}z} \qquad \text{(B.10)} \\ {}^{m}I^{N}(k_p,z) &= \frac{1}{Z_N} \cdot {}^{m}V^{N-1}(k_p,h_{N-1})e^{-jk_{zN}z} \qquad \text{(B.11)} \end{aligned}$$

B.2.2 MTS

For the MTS structure we can apply the same previous steps: from the MTS stratified media structure, we can represent the transmission line model (see Figure B.5). Here we have represented a practical model of a MTS with two layers (for example, Foam and Kapton) as mechanical substrate to support the metasurface.

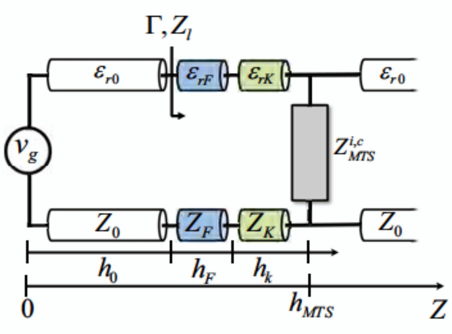
Γ, Z_l
ε_{r0}
ε_{rF}
ε_{rK}
ε_{r0}
v_g
$Z^{i,c}_{MTS}$
Z_0
Z_F
Z_K
Z_0
h_0
h_F
h_k
0
h_{MTS}
Z

Fig. B.5 Equivalent transmission line model for a practical MTS stratified media.

The voltages and currents as a function of the distance can be known by

$$
\begin{aligned}
{}^{m}V^{1}(k_p,z) &= V^{1+}e^{-jk_{z1}z}+V^{1-}e^{jk_{z1}z} && \text{(B.12)}\\
{}^{m}I^{1}(k_p,z) &= \frac{1}{Z_1}(V^{1+}e^{-jk_{z1}z}-V^{1-}e^{jk_{z1}z}) && \text{(B.13)}
\end{aligned}
$$

$$
\begin{aligned}
{}^{m}V^{2}(k_p,z) &= V^{2+}e^{-jk_{z2}z} && \text{(B.14)}\\
{}^{m}I^{2}(k_p,z) &= \frac{1}{Z_2}(V^{2+}e^{-jk_{z2}z}) && \text{(B.15)}
\end{aligned}
$$

$Z_{in2}=Z_g||Z_2$, and Z_g, Z_2 depend on k_x, k_y. Z_g is an imaginary impedance that is designed with the Tretyakov model [126]. The modal impedances are similarly defined (see eq B.7 and eq B.8). The reflection coefficient and the input impedance can be then calculated by:

$$\Gamma_1=\frac{Z_{in(2)}-Z_1}{Z_{in(2)}+Z_1} \tag{B.16}$$

$$Z_{in(1)}=Z_1\frac{Z_{in(2)}+jZ_1tan(kz_1h_{FSS})}{Z_1+jZ_{in(2)}tan(kz_1h_{FSS})} \tag{B.17}$$

$$V^{1^+} = \frac{Z_1}{Z_{in(1)}} \cdot V_g \cdot \frac{1}{(1-\Gamma_1 e^{-j2k_{z1}h_{FSS}})} = V_g \cdot \frac{1}{(1+\Gamma_1 e^{-j2k_{z1}h_{FSS}})} \tag{B.18}$$

Now equalizing voltages in $z = h_{FSS}$, N=2.

$$V^{2+} = \frac{Z_g Z_2}{Z_g + Z_2} \cdot \frac{1}{e^{-jk_{z2}h_{FSS}}} \cdot \frac{1}{Z_1} \cdot (V^{1+} e^{-jk_{z1}h_{FSS}}(1-\Gamma_1)) \tag{B.19}$$

$$V^{2+} = \frac{Z_g Z_2}{Z_g + Z_2} \cdot \frac{e^{-jk_{z1}h_{FSS}}}{e^{-jk_{z2}h_{FSS}}} \cdot \frac{1}{Z_1} \cdot (1-\Gamma_1) \cdot V^{1+} \tag{B.20}$$

These voltages and current lines will be useful to solve the spatial and spectral Green' function required to calculate the radiated near- and far-field.

Appendix C

Calculation of the Radiated Far and Near-Fields

In this appendix we show how to calculate the far- and near-field of a planar antenna embbeded in a planar stratified medium.

The electric field $\vec{E}$ radiated by a generic volumetric current density can be calculated as the convolution integral with the pertinent spatial Green's function and the spatial current distribution:

$$\vec{E}(\vec{r}) = \iiint\limits_{v} \widetilde{G}^{ej}(\vec{r}-\vec{r}')\,j(\vec{r}')d\vec{r}' \tag{C.1}$$

Due to the planar geometry of the antennas studied in this thesis, the current distribution is defined over a surface domain at a certain quote in the stratification. Figure C.1 shows the considered study case. Overall the observation point P can be located in any region of the space, but depends on this region, the field will have a different dependence of the distance r. In the near- field region (i.e. when $r \leq \lambda/\pi$) the field has radial components and can not be represented as a propagating wave whilst in the far-field (i.e. when $r \gg \lambda/\pi$) the radiated field has only transverse components and thus it can be represented as a propagating spherical wave. This means that the Green's function has in general terms in $(kR)^{-}1$, $(kR)^{-}2$ and $(kR)^{-}3$ but in the far-field, for which $R \gg \lambda$, only the terms with $(kR)^{-}1$ survive. On the other hand, the dominant terms in the near-field, for which $R \ll \lambda$, are the terms with $(kR)^{-}3$ whilst the terms with $(kR)^{-}2$ dominate the intermediate-field at $R \approx \lambda$.

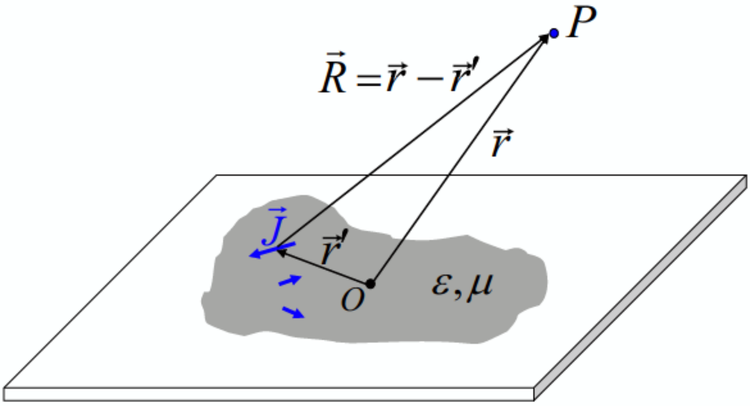

Fig. C.1 Superficial current density over a planar antenna. To calculate the far-fields, we consider $\vec{R} \gg \vec{r}'$

For the case of planar antennas embedded in a stratified media, the Green's function is only know analytically in the spectral domain [17]. Therefore the electric field radiated by the antenna can be conveniently expressed as the inverse Fourier transform of the product between the spectral Green's function (SGF) (see appendix B) and the Fourier transform (FT) of these current distributions. In rectangular coordinates the expression to calculate the electric Field E(x,y,z) if we consider a magnetic source in any region is [18]:

$$E(x,y,z) = \frac{1}{(2\pi)^2} \int_{-\infty}^{\infty} \int_{-\infty}^{\infty} \underline{\underline{G}}^{es}(k_x,k_y,z,z') S(k_x,k_y) e^{-jk_x x} e^{-jk_y y} d_{k_x} d_{k_y} \tag{C.2}$$

Where $\underline{\underline{G}}^{es}(k_x,k_y,z,z')$ is the spectral Green's function for a source s (magnetic m or electric j current). $S(k_x,k_y)$ represents the Fourier Transform of the excitation current.

Depending on the nature of our design, we will be interested to find the near- or far-field (second and third part of this thesis respectively). In order to properly solve the integral equation (eq C.2) we have to derive the proper approximations, as it is shown in the next two sections.

C.1 Far-Field Calculation

The far-field can be approximated from eq C.2, using the convolution of the Dyadic Green's function of the stratified media with the magnetic or electric source distribution. An asymptotic evaluation can be done if one multiplies and divides eq C.2 by $\frac{e^{-jk_z z}}{k_z}$ so it can assumed that $(k_z \underline{\underline{G}}^{em}(k_x,k_y,z,z') S(k_x,k_y) e^{-jk_z z})$ has a slow variation around k_x, k_y in the surrounding of the saddle point $k_x = k_{xs}, k_y = k_{ys}$ and extract it from the integral as a constant [18]:

$$E(x,y,z) = k_{zs}\underline{\underline{G}}^{es}(k_{xs},k_{ys},z,z')S(k_{xs},k_{ys})e^{jk_{zs}z}\left(\frac{1}{(2\pi)^2}\int_{-\infty}^{\infty}\int_{-\infty}^{\infty}\frac{e^{-jk_xx}e^{-jk_yy}e^{-jk_zz}}{k_z}d_{k_x}d_{k_y}\right) \tag{C.3}$$

The integral in the second term is a canonical integral, thus:

$$E(x,y,z) \approx 2jk_{zs}\underline{\underline{G}}^{es}(k_{xs},k_{ys},z,z')S(k_{xs},k_{ys})e^{jk_{zs}z}\frac{e^{-jkr}}{4\pi r} \tag{C.4}$$

Where

$$\begin{aligned} k_{xs} &= k_0 \sin\theta\cos\phi \\ k_{ys} &= k_0 \sin\theta\sin\phi \\ k_{zs} &= k_0 \cos\theta \end{aligned}$$

Now changing the coordinate system from rectangular to spherical:

$$E_\theta = E_x \cdot cos\theta \cdot cos\phi + E_y \cdot cos\theta \cdot sin\phi - E_z \cdot sin\theta \tag{C.5}$$

$$E_\phi = -E_x \cdot sin\phi + E_y \cdot cos\phi \tag{C.6}$$

Due to $\vec{R} \gg \vec{r}'$, the radiated far-field does not depend on the origin of the coordinate system. In fact as the observation point is located far away from the origin $|\vec{R}| \to +\infty$, the current distribution can be seen as a punctual concentrated charge.

C.2 Near Field Calculation

On the opposite side when we consider the near-field, the position of each current element $\vec{J}_i$ is determinant, as it can seen in Figure C.2. This can be interpreted because the tensor $\vec{R}$ depends on the considered element current $\vec{J}_i$ and the resulting field is the summation of all the elementary current contributions. As a consequence of this fact the spatial Green's function are more convenient for this case, although this has a problem because this is not analytically in a stratified medium. However, due to the kind of antennas studied in this thesis (i.e. Part III, Chapters II.2-II.4) there is a simple way to calculate the radiated near-

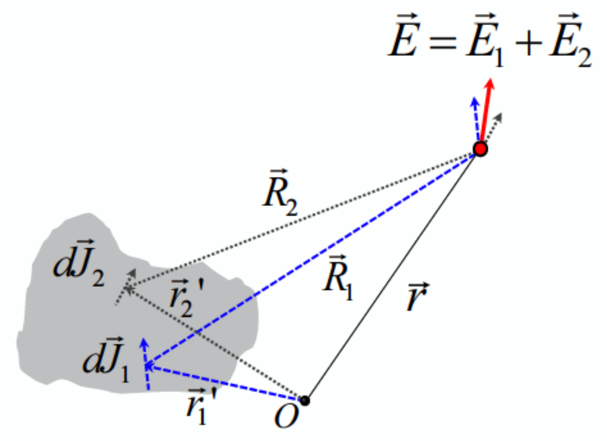

Fig. C.2 Radiated near-field by a superficial electric current density.

fields. For holographic antennas, we have approximated the field distribution on the antenna aperture (i.e. just above the radiating slots) by a leaky distribution, (eq II.2.18- II.2.20). Moreover, in general, the radiation of any directive antenna could be related to an equivalent magnetic current distribution defined just above the antenna (or dielectric stratification) and radiating in free space. When this equivalent current over the antenna is known, we can use the spatial Green's function in the free space (this is analytically known) in order to find the radiated near-fields. In the near field the electric field can be calculated by using the radiative components of the free space Green's function as follows:

$$\vec{E}(\vec{r}) = \iint_{s} jk\widehat{R}\times M(\vec{r}')d\vec{r}' \tag{C.7}$$

Where $\widehat{R}$ is the unit vector between the differential current contribution and the observation point as shown in Figure C.2. Other more general way of doing it (when the fields over the aperture of the antenna are unknown or time-consuming to calculate them) consists on the pre-tabulation of the Green's function in the space domain (further details of this procedure can be found in [18]).

References

[1] W. W. Hansen, "Radiating Electromagnetic Wave Guide," Jun 1946. US Patent 2,402,622.

[2] M. Ettorre, "Analysis and Design of Efficient Planar Leaky-Wave Antennas," *PhD thesis, University of Siena, Siena, Italy*, 2008.

[3] C. Balanis, *Modern antenna handbook.* John Wiley & Sons, 2011.

[4] D. Jackson and N. Alexopoulos, "Gain Enhancement Methods for Printed Circuit Antennas," *IEEE Transactions on Antennas and Propagation*, vol. 33, pp. 976–987, Sep 1985.

[5] G. Trentini, "Partially Reflecting Sheet Arrays," *IRE Transactions on Antennas and Propagation*, vol. 4, pp. 666–671, Oct 1956.

[6] D. Jackson, A. Oliner, and A. Ip, "Leaky-Wave Propagation and Radiation for a Narrow-Beam Multiple-Layer Dielectric Structure," *IEEE Transactions on Antennas and Propagation*, vol. 41, pp. 344–348, Mar 1993.

[7] C. Cheype, C. Serier, M. Thevenot, T. Monediere, A. Reineix, and B. Jecko, "An Electromagnetic Bandgap Resonator Antenna," *IEEE Transactions on Antennas and Propagation*, vol. 50, pp. 1285–1290, Sep 2002.

[8] T. Zhao, D. Jackson, J. Williams, H. Yang, and A. Oliner, "2-D Periodic Leaky-Wave Antennas-Part I: Metal Patch Design," *IEEE Transactions on Antennas and Propagation*, vol. 53, pp. 3505–3514, Nov 2005.

[9] T. Zhao, D. Jackson, and J. Williams, "2-D Periodic Leaky-Wave Antennas-Part II: Slot Design," *IEEE Transactions on Antennas and Propagation*, vol. 53, pp. 3515–3524, Nov 2005.

[10] A. Feresidis, G. Goussetis, S. Wang, and J. Vardaxoglou, "Artificial Magnetic Conductor Surfaces and their Application to Low-Profile High-Gain Planar Antennas," *IEEE Transactions on Antennas and Propagation*, vol. 53, pp. 209–215, Jan 2005.

[11] J. Young, H. Sung, S. Wee, S. Jae, and I. Soon, "Multilayer Spatial Angular Filter with Airgap Tuners to Suppress Grating Lobes of 4x1 Array Antenna," *Electronics Letters*, vol. 39, pp. 15–17, Jan 2003.

[12] N. Guerin, S. Enoch, G. Tayeb, P. Sabouroux, P. Vincent, and H. Legay, “A Metallic Fabry-Perot Directive Antenna,” *IEEE Transactions on Antennas and Propagation*, vol. 54, pp. 220–224, Jan 2006.

[13] A. Neto and N. Llombart, “Wideband Localization of the Dominant Leaky Wave Poles in Dielectric Covered Antennas,” *IEEE Antennas and Wireless Propagation Letters*, vol. 5, pp. 549–551, Dec 2006.

[14] G. Lovat, P. Burghignoli, and D. Jackson, “Fundamental Properties and Optimization of Broadside Radiation from Uniform Leaky-Wave Antennas,” *IEEE Transactions on Antennas and Propagation*, vol. 54, pp. 1442–1452, May 2006.

[15] A. Foroozesh and L. Shafai, “Investigation Into the Effects of the Patch-Type FSS Superstrate on the High-Gain Cavity Resonance Antenna Design,” *IEEE Transactions on Antennas and Propagation*, vol. 58, pp. 258–270, Feb 2010.

[16] A. Polemi and S. Maci, “On the Polarization Properties of a Dielectric Leaky Wave Antenna,” *IEEE Antennas and Wireless Propagation Letters*, vol. 5, pp. 306–310, Dec 2006.

[17] L. Felsen and N. Marcuvitz, *Radiation and Scattering of Waves*. IEEE Press Series on Electromagnetic Wave Theory, Wiley, 1994.

[18] N. Llombart, *Development of Integrated Printed Array Antennas Using EBG Substrates*. PhD thesis, PhD thesis, Universidad Politécnica de Valencia, Spain, 2006.

[19] R. F. Harrington, *Field Computation by Moment Methods*. Wiley-IEEE Press, 1993.

[20] Y. Lee, X. Lu, Y. Hao, S. Yang, J. Evans, and C. Parini, “Low-Profile Directive Millimeter-Wave Antennas Using Free-Formed Three-Dimensional (3-D) Electromagnetic Bandgap Structures,” *IEEE Transactions on Antennas and Propagation*, vol. 57, pp. 2893–2903, Oct 2009.

[21] G. Lovat, P. Burghignoli, F. Capolino, D. Jackson, and D. Wilton, “Analysis of Directive Radiation from a Line Source in a Metamaterial Slab with Low Permittivity,” *IEEE Transactions on Antennas and Propagation*, vol. 54, pp. 1017–1030, Mar 2006.

[22] A. Feresidis and J. Vardaxoglou, “High Gain Planar Antenna Using Optimised Partially Reflective Surfaces,” *IEE Proceedings Microwaves, Antennas and Propagation*, vol. 148, pp. 345–350, Dec 2001.

[23] D. Jackson and A. Oliner, “A Leaky-Wave Analysis of the High-Gain Printed Antenna Configuration,” *IEEE Transactions on Antennas and Propagation*, vol. 36, pp. 905–910, Jul 1988.

[24] N. Llombart, A. Neto, G. Gerini, M. Bonnedal, and P. de Maagt, “Leaky Wave Enhanced Feed Arrays for the Improvement of the Edge of Coverage Gain in Multibeam Reflector Antennas,” *IEEE Transactions on Antennas and Propagation*, vol. 56, pp. 1280–1291, May 2008.

[25] C. Menudier, R. Chantalat, E. Arnaud, M. Thevenot, T. Monediere, and P. Dumon, “EBG Focal Feed Improvements for Ka-Band Multibeam Space Applications,” *IEEE Antennas and Wireless Propagation Letters*, vol. 8, pp. 611–615, 2009.

[26] R. Gardelli, M. Albani, and F. Capolino, “Array Thinning by Using Antennas in a Fabry-Perot Cavity for Gain Enhancement,” *IEEE Transactions on Antennas and Propagation*, vol. 54, pp. 1979–1990, Jul 2006.

[27] N. Llombart, A. Neto, G. Gerini, M. Bonnedal, and P. de Maagt, “Impact of Mutual Coupling in Leaky Wave Enhanced Imaging Arrays,” *IEEE Transactions on Antennas and Propagation*, vol. 56, pp. 1201–1206, Apr 2008.

[28] L. Huang, J.-C. Chiao, and P. De Lisio, “An Electronically Switchable Leaky Wave Antenna,” *IEEE Transactions on Antennas and Propagation*, vol. 48, pp. 1769–1772, Nov 2000.

[29] D. Sievenpiper, J. Schaffner, J. Lee, and S. Livingston, “A Steerable Leaky-Wave Antenna Using a Tunable Impedance Ground Plane,” *IEEE Antennas and Wireless Propagation Letters*, vol. 1, no. 1, pp. 179–182, 2002.

[30] G. Minatti, M. Casaletti, F. Caminita, P. De Vita, and S. Maci, “Planar Antennas Based on Surface-to-Leaky Wave Transformation,” in *Proceedings of the 5th European Conference on Antennas and Propagation EUCAP*, pp. 1915–1918, Apr 2011.

[31] G. Minatti, F. Caminita, M. Casaletti, and S. Maci, “Spiral Leaky-Wave Antennas Based on Modulated Surface Impedance,” *IEEE Transactions on Antennas and Propagation*, vol. 59, pp. 4436–4444, Dec 2011.

[32] H. Sasazawa, Y. Oshima, K. Sakurai, M. Ando, and N. Goto, “Slot Coupling in a Radial Line Slot Antenna for 12-GHz Band Satellite TV Reception,” *IEEE Transactions on Antennas and Propagation*, vol. 36, pp. 1221–1226, Sep 1988.

[33] A. Ourir, S. Burokur, and A. de Lustrac, “Electronically Reconfigurable Metamaterial for Compact Directive Cavity Antennas,” *Electronics Letters*, vol. 43, pp. 698–700, Jun 2007.

[34] A. Weily, T. Bird, and Y. Guo, “A Reconfigurable High-Gain Partially Reflecting Surface Antenna,” *IEEE Transactions on Antennas and Propagation*, vol. 56, pp. 3382–3390, Nov 2008.

[35] R. Guzman, J. Gomez, A. Weily, and Y. Guo, “Electronically Steerable 1-D Fabry-Perot Leaky-Wave Antenna Employing a Tunable High Impedance Surface,” *IEEE Transactions on Antennas and Propagation*, vol. 60, pp. 5046–5055, Nov 2012.

[36] B. Zeb, Y. Ge, K. Esselle, Z. Sun, and M. Tobar, “A Simple Dual-Band Electromagnetic Band Gap Resonator Antenna Based on Inverted Reflection Phase Gradient,” *IEEE Transactions on Antennas and Propagation*, vol. 60, pp. 4522–4529, Oct 2012.

[37] M. Al-Tarifi, D. Anagnostou, A. Amert, and K. Whites, “Dual-Band Resonant Cavity Antenna with a Single Dielectric Superstrate,” in *IEEE Antennas and Propagation Society International Symposium (APSURSI)*, pp. 1–2, Jul 2012.

[38] N. Llombart, A. Neto, G. Gerini, M. Bonnedal, and P. de Maagt, “Impact of Mutual Coupling in Leaky Wave Enhanced Imaging Arrays,” *IEEE Transactions on Antennas and Propagation*, vol. 56, pp. 1201–1206, Apr 2008.

[39] A. Neto, M. Ettorre, G. Gerini, and P. de Maagt, “Leaky Wave Enhanced Feeds for Multibeam Reflectors to be Used for Telecom Satellite Based Links,” *IEEE Transactions on Antennas and Propagation*, vol. 60, pp. 110–120, Jan 2012.

[40] G. Palikaras, A. Feresidis, and J. Vardaxoglou, “Cylindrical Electromagnetic Band Gap Structures for Directive Base Station Antennas,” *IEEE Antennas and Wireless Propagation Letters*, vol. 3, pp. 87–89, Dec 2004.

[41] J. Young, Y. Junho, R. Mittra, and W. S. Park, “Application of Electromagnetic Bandgap (EBG) Superstrates with Controllable Defects for a Class of Patch Antennas as Spatial Angular Filters,” *IEEE Transactions on Antennas and Propagation*, vol. 53, pp. 224–235, Jan 2005.

[42] R. Chantalat, C. Menudier, M. Thevenot, T. Monediere, E. Arnaud, and P. Dumon, “Enhanced EBG Resonator Antenna as Feed of a Reflector Antenna in the Ka Band,” *IEEE Antennas and Wireless Propagation Letters*, vol. 7, pp. 349–353, 2008.

[43] N. Llombart, A. Neto, G. Gerini, M. Bonnedal, and P. de Maagt, “Leaky Wave Enhanced Feed Arrays for the Improvement of the Edge of Coverage Gain in Multibeam Reflector Antennas,” *IEEE Transactions on Antennas and Propagation*, vol. 56, pp. 1280–1291, May 2008.

[44] L. Yoonjae, L. Xuesong, H. Yang, Y. Shoufeng, J. Evans, and C. Parini, “Low-Profile Directive Millimeter-Wave Antennas Using Free-Formed Three-Dimensional (3-D) Electromagnetic Bandgap Structures,” *IEEE Transactions on Antennas and Propagation*, vol. 57, pp. 2893–2903, Oct 2009.

[45] R. Sauleau, P. Coquet, and T. Matsui, “Low-Profile Directive Quasi-Planar Antennas Based on Millimetre Wave Fabry-Perot Cavities,” *IEE Proceedings Microwaves, Antennas and Propagation*, vol. 150, pp. 274–278, Aug 2003.

[46] M. Leutenegger, R. Rao, R. Leitgeb, and T. Lasser, “Fast Focus Field Calculations,” *Opt. Express*, vol. 14, pp. 11277–11291, Nov 2006.

[47] P. Checcacci, V. Russo, and A. Scheggi, “Holographic Antennas,” *Proceedings of the IEEE*, vol. 56, no. 12, pp. 2165–2167, 1968.

[48] P. Hariharan, *Optical Holography*, ch. all. Cambridge University Press, 1996.

[49] D. Sievenpiper, J. Colburn, B. Fong, J. Ottusch, and J. Visher, “Holographic Artificial Impedance Surfaces for Conformal Antennas,” in *IEEE Antennas and Propagation Society International Symposium*, vol. 1B, pp. 256–259, 2005.

[50] B. Fong, J. Colburn, J. Ottusch, J. Visher, and D. Sievenpiper, “Scalar and Tensor Holographic Artificial Impedance Surfaces,” *IEEE Transactions on Antennas and Propagation*, vol. 58, pp. 3212–3221, Oct 2010.

[51] D. Sievenpiper, Z. Lijun, R. Broas, N. Alexopolous, and E. Yablonovitch, “High-Impedance Electromagnetic Surfaces with a Forbidden Frequency Band,” *IEEE Transactions on Microwave Theory and Techniques*, vol. 47, pp. 2059–2074, Nov 1999.

[52] S. Maci, “Metasurfing: Addressing Waves on Metasurfaces for Realizing Antennas and Microwave Devices,” in *IEEE 4th International Symposium on Microwave, Antenna, Propagation and EMC Technologies for Wireless Communications (MAPE)*, pp. K1–K4, Nov 2011.

[53] S. Maci, G. Minatti, M. Casaletti, and M. Bosiljevac, “Metasurfing: Addressing Waves on Impenetrable Metasurfaces,” *IEEE Antennas and Wireless Propagation Letters*, vol. 10, pp. 1499–1502, 2011.

[54] C. Walter, “Surface-Wave Luneberg Lens Antennas,” *IRE Transactions on Antennas and Propagation*, vol. 8, pp. 508–515, Sep 1960.

[55] R. King, D. Thiel, and K. Park, “The Synthesis of Surface Reactance Using an Artificial Dielectric,” *IEEE Transactions on Antennas and Propagation*, vol. 31, pp. 471–476, May 1983.

[56] K. Sato and H. Ujiie, “A Plate Luneberg Lens with the Permittivity Distribution Controlled by Hole Density,” *Electronics and Communications in Japan (Part I: Communications)*, vol. 85, no. 9, pp. 1–12, 2002.

[57] L. Xue and V. Fusco, “Printed Holey Plate Luneburg Lens,” *Microwave and Optical Technology Letters*, vol. 50, no. 2, pp. 378–380, 2008.

[58] C. Holloway, A. Dienstfrey, E. Kuester, J. O’Hara, A. Azad, and A. Taylor, “A Discussion on the Interpretation and Characterization of Metafilms/Metasurfaces: The Two-Dimensional Equivalent of Metamaterials,” *Metamaterials*, vol. 3, no. 2, pp. 100–112, 2009.

[59] M. Nannetti, F. Caminita, and S. Maci, “Leaky-Wave Based Interpretation of the Radiation from Holographic Surfaces,” in *IEEE Antennas and Propagation Society International Symposium*, pp. 5813–5816, Jun 2007.

[60] A. Oliner and A. Hessel, “Guided Waves on Sinusoidally-Modulated Reactance Surfaces,” *IRE Transactions on Antennas and Propagation*, vol. 7, pp. 201–208, Dec 1959.

[61] J. Sherman, “Properties of Focused Apertures in the Fresnel Region,” *IRE Transactions on Antennas and Propagation*, vol. 10, no. 4, pp. 399–408, 1962.

[62] Y. Li and E. Wolf, “Focal Shifts in Diffracted Converging Spherical Waves,” *Optics Communications.*, vol. 39, no. 4, pp. 211–215, 1981.

[63] R. Hansen, “Focal Region Characteristics of Focused Array Antennas,” *IEEE Transactions on Antennas and Propagation*, vol. 33, pp. 1328–1337, Dec 1985.

[64] C. Balanis, *Antenna Theory*, pp. 453–454. Singapore: John Wiley and Sons, 1982.

[65] W. Graham, “Analysis and Synthesis of Axial Field Patterns of Focused Apertures,” *IEEE Transactions on Antennas and Propagation*, vol. 31, pp. 665–668, Jul 1983.

[66] W. Gee, S.-W. L., N. K. Bong, C. Cain, R. Mittra, and R. Magin, “Focused Array Hyperthermia Applicator: Theory and Experiment,” *IEEE Transactions on Biomedical Engineering*, vol. BME-31, no. 1, pp. 38–46, 1984.

[67] M. Bogosanovic and A. Williamson, “Microstrip Antenna Array With a Beam Focused in the Near-Field Zone for Application in Noncontact Microwave Industrial Inspection,” *IEEE Transactions on Instrumentation and Measurement*, vol. 56, no. 6, pp. 2186–2195, 2007.

[68] A. Buffi, A. Serra, P. Nepa, H. Chou, and G. Manara, “A Focused Planar Microstrip Array for 2.4 GHz RFID Readers,” *IEEE Transactions on Antennas and Propagation*, vol. 58, pp. 1536–1544, May 2010.

[69] R. Siragusa, P. Lemaitre-Auger, and S. Tedjini, “Tunable Near-Field Focused Circular Phase-Array Antenna for 5.8-GHz RFID Applications,” *IEEE Antennas and Wireless Propagation Letters*, vol. 10, pp. 33–36, 2011.

[70] H. Chou, H. Hung, N. Wang, H. Chou, C. Tung, and P. Nepa, “Design of a Near-Field Focused Reflectarray Antenna for 2.4 GHz RFID Reader Applications,” *IEEE Transactions on Antennas and Propagation*, vol. 59, pp. 1013–1018, Mar 2011.

[71] A. Oliner and J. R., *Antenna Engineering Handbook*, ch. all. McGraw-Hill, 1993.

[72] I. Ohtera, “Focusing Properties of a Microwave Radiator Utilizing a Slotted Rectangular Waveguide,” *IEEE Transactions on Antennas and Propagation*, vol. 38, pp. 121–124, Jan 1990.

[73] P. Burghignoli, F. Frezza, A. Galli, and G. Schettini, “Synthesis of Broad-Beam Patterns through Leaky-Wave Antennas with Rectilinear Geometry,” *IEEE Antennas and Wireless Propagation Letters*, vol. 2, no. 1, pp. 136–139, 2003.

[74] J. Gomez, F. Quesada, A. Alvarez, G. Goussetis, A. Weily, and Y. Guo, “Frequency Steerable Two Dimensional Focusing Using Rectilinear Leaky-Wave Lenses,” *IEEE Transactions on Antennas and Propagation*, vol. 59, no. 2, pp. 407–415, 2011.

[75] Y. Monnai and H. Shinoda, “Focus-Scanning Leaky-Wave Antenna With Electronically Pattern-Tunable Scatterers,” *IEEE Transactions on Antennas and Propagation*, vol. 59, pp. 2070–2077, Jun 2011.

[76] K. Stephan, J. Mead, D. Pozar, L. Wang, and J. Pearce, “A Near Field Focused Microstrip Array for a Radiometric Temperature Sensor,” *IEEE Transactions on Antennas and Propagation*, vol. 55, no. 4, pp. 1199–1203, 2007.

[77] M. Ettorre and A. Grbic, “Generation of Propagating Bessel Beams Using Leaky-Wave Modes,” *IEEE Transactions on Antennas and Propagation*, vol. 60, pp. 3605–3613, Aug 2012.

[78] M. Ettorre, S. Rudolph, and A. Grbic, “Generation of Propagating Bessel Beams Using Leaky-Wave Modes: Experimental Validation,” *IEEE Transactions on Antennas and Propagation*, vol. 60, pp. 2645–2653, Jun 2012.

[79] A. Patel and A. Grbic, “A Printed Leaky-Wave Antenna Based on a Sinusoidally-Modulated Reactance Surface,” *IEEE Transactions on Antennas and Propagation*, vol. 59, pp. 2087–2096, Jun 2011.

[80] M. Albani, A. Mazzinghi, and A. Freni, “Automatic Design of CP-RLSA Antennas,” *IEEE Transactions on Antennas and Propagation*, vol. 60, pp. 5538–5547, Dec 2012.

[81] A. Ip and D. Jackson, "Radiation from Cylindrical Leaky Waves," *IEEE Transactions on Antennas and Propagation*, vol. 38, pp. 482–488, Apr 1990.

[82] C. Caloz and T. Itoh, "Array Factor Approach of Leaky-Wave Antennas and Application to 1-D/2-D Composite Right/Left-Handed (CRLH) Structures," *IEEE Microwave and Wireless Components Letters*, vol. 14, pp. 274–276, Jun 2004.

[83] S. Lim, C. Caloz, and T. Itoh, "Metamaterial Based Electronically Controlled Transmission Line Structure as a Novel Leaky Wave Antenna with Tunable Radiation Angle and Beamwidth," *IEEE Transactions on Microwave Theory and Techniques*, vol. 53, pp. 161–173, Jan 2005.

[84] M. Hashemi and T. Itoh, "Dispersion Engineered Metamaterial-Based Transmission Line for Conformal Surface Application," in *IEEE MTT-S International Microwave Symposium Digest*, pp. 331–334, Jun 2008.

[85] J. Gomez, F. Quesada, and A. Alvarez, "Analysis and Design of Periodic Leaky-Wave Antennas for the Millimeter Waveband in Hybrid Waveguide-Planar Technology," *IEEE Transactions on Antennas and Propagation*, vol. 53, pp. 2834–2842, Sep 2005.

[86] M. Takahashi, J. Takada, M. Ando, and N. Goto, "A Slot Design for Uniform Aperture Field Distribution in Single-Layered Radial Line Slot Antennas," *IEEE Transactions on Antennas and Propagation*, vol. 39, pp. 954–959, Jul 1991.

[87] P. Burghignoli, G. Lovat, and D. Jackson, "Analysis and Optimization of Leaky-Wave Radiation at Broadside From a Class of 1-D Periodic Structures," *IEEE Transactions on Antennas and Propagation*, vol. 54, pp. 2593–2604, Sep 2006.

[88] N. Llombart, A. Neto, G. Gerini, and P. de Maagt, "Planar Circularly Symmetric EBG Structures for Reducing Surface Waves in Printed Antennas," *IEEE Transactions on Antennas and Propagation*, vol. 53, pp. 3210–3218, Oct 2005.

[89] M. Ettorre, S. Bruni, G. Gerini, A. Neto, N. Llombart, and S. Maci, "Sector PCS-EBG Antenna for Low-Cost High-Directivity Applications," *IEEE Antennas and Wireless Propagation Letters*, vol. 6, pp. 537–539, 2007.

[90] M. Imani and A. Grbic, "Generating Evanescent Bessel Beams Using Near-Field Plates," *IEEE Transactions on Antennas and Propagation*, vol. 60, pp. 3155–3164, Jul 2012.

[91] J. Gomez, "Unusual Tapering of Leaky-Wave Radiators and their Applications," in *Proceedings of the 5th European Conference on Antennas and Propagation EUCAP*, pp. 821–824, Apr 2011.

[92] M. Ando, K. Sakurai, N. Goto, K. Arimura, and Y. Ito, "A Radial Line Slot Antenna for 12 GHz Satellite TV Reception," *IEEE Transactions on Antennas and Propagation*, vol. 33, pp. 1347–1353, Dec 1985.

[93] A. Akiyama, T. Yamamoto, M. Ando, and N. Goto, "Numerical Optimisation of Slot Parameters for a Concentric Array Radial Line Slot Antenna," *IEE Proceedings Microwaves, Antennas and Propagation*, vol. 145, pp. 141–146, Apr 1998.

[94] C. Pfeiffer and A. Grbic, "A Printed, Broadband Luneburg Lens Antenna," *IEEE Transactions on Antennas and Propagation*, vol. 58, pp. 3055–3059, Sep 2010.

[95] "Spatial corp, CST STUDIO SUITE®, release version," 2012.

[96] F. Goebels and K. Kelly, "Arbitrary Polarization from Annular Slot Plannar Antennas," *IRE Transactions on Antennas and Propagation*, vol. 9, no. 4, pp. 342–349, 1961.

[97] A. Oliner and D. Jackson, *Leaky-Wave Antennas in Antenna Engineering Handbook*, ch. 11. 4th ed., J. L. Volakis, Ed. New York: McGraw-Hill, 2007.

[98] J. Gomez, D. Blanco, E. Rajo, and N. Llombart, "Holographic Surface Leaky-Wave Lenses With Circularly-Polarized Focused Near-Fields–Part I: Concept, Design and Analysis Theory," *IEEE Transactions on Antennas and Propagation*, vol. 61, no. 7, pp. 3475–3485, 2013.

[99] M. Pastorino, *Applications of Microwave Imaging*, ch. 10. John Wiley and Sons, Inc., 2010.

[100] S. Karimkashi and A. Kishk, "Focused Microstrip Array Antenna Using a Dolph-Chebyshev Near-Field Design," *IEEE Transactions on Antennas and Propagation*, vol. 57, no. 12, pp. 3813–3820, 2009.

[101] Y. Li and E. Wolf, "Three-Dimensional Intensity Distribution Near the Focus in Systems of Different Fresnel Numbers," *J. Opt. Soc. Am. A*, vol. 1, pp. 801–808, Aug 1984.

[102] J. Gomez, A. Martinez, N. Llombart, D. Blanco, and E. Rajo, "Near-Field Focusing with Holographic Two-Dimensional Tapered Leaky-Wave Slot Antennas," in *6th European Conference on Antennas and Propagation EUCAP*, pp. 234–238, Mar 2012.

[103] M. Ettorre, M. Casaletti, G. Valerio, R. Sauleau, L. Le Coq, S. Pavone, and M. Albani, "On the Near-Field Shaping and Focusing Capability of a Radial Line Slot Array," *IEEE Transactions on Antennas and Propagation*, vol. 62, pp. 1991–1999, Apr 2014.

[104] M. Bray, D. Werner, D. Boeringer, and D. Machuga, "Optimization of Thinned Aperiodic Linear Phased Arrays Using Genetic Algorithms to Reduce Grating Lobes During Scanning," *IEEE Transactions on Antennas and Propagation*, vol. 50, pp. 1732–1742, Dec 2002.

[105] S. Sanzgiri, D. Bostrom, W. Pottenger, and R. Q. Lee, "A Hybrid Tile Approach for Ka Band Subarray Modules," *IEEE Transactions on Antennas and Propagation*, vol. 43, pp. 953–959, Sep 1995.

[106] W. Hao, F. Da-Gang, and Y. Chow, "Grating Lobe Reduction in a Phased Array of Limited Scanning," *IEEE Transactions on Antennas and Propagation*, vol. 56, pp. 1581–1586, Jun 2008.

[107] T. Brockett and Y. Rahmat-Samii, "Subarray Design Diagnostics for the Suppression of Undesirable Grating Lobes," *IEEE Transactions on Antennas and Propagation*, vol. 60, pp. 1373–1380, Mar 2012.

[108] R. Mailloux, L. Zahn, and A. Martinez, "Grating Lobe Control in Limited Scan Arrays," *IEEE Transactions on Antennas and Propagation*, vol. 27, pp. 79–85, Jan 1979.

[109] R. Mailloux, "Synthesis of Spatial Filters with Chebyshev Characteristics," *IEEE Transactions on Antennas and Propagation*, vol. 24, pp. 174–181, Mar 1976.

[110] P. Franchi and R. Mailloux, "Theoretical and Experimental Study of Metal Grid Angular Filters for Sidelobe Suppression," *IEEE Transactions on Antennas and Propagation*, vol. 31, pp. 445–450, May 1983.

[111] T. Zhao, D. Jackson, J. Williams, and A. Oliner, "General Formulas for a 2D Leaky-Wave Antenna," in *IEEE Antennas and Propagation Society International Symposium*, vol. 2, pp. 1134–1137, Jun 2003.

[112] W. Syed and A. Neto, "Front-to-Back Ratio Enhancement of Planar Printed Antennas by Means of Artificial Dielectric Layers," *IEEE Transactions on Antennas and Propagation*, vol. 61, pp. 5408–5416, Nov 2013.

[113] D. Blanco, N. Llombart, and E. Rajo, "On the Use of Leaky Wave Phased Arrays for the Reduction of the Grating Lobe Level," *IEEE Transactions on Antennas and Propagation*, vol. 62, pp. 1789–1795, Apr 2014.

[114] M. Pasian, M. Bozzi, and L. Perregrini, "Design of a Large Bandwidth Planar Antenna using Inductive Frequency Selective Surfaces," in *The Second European Conference on Antennas and Propagation, EuCAP*, pp. 1–5, Nov 2007.

[115] K. Sarabandi and N. Behdad, "A Frequency Selective Surface With Miniaturized Elements," *IEEE Transactions on Antennas and Propagation*, vol. 55, pp. 1239–1245, May 2007.

[116] M. Qiu, G. Eleftheriades, and M. Hickey, "A Reduced Surface-Wave Twin Arc-Slot Antenna Element on Electrically Thick Substrates," in *Antennas and Propagation Society International Symposium, 2001. IEEE*, vol. 3, pp. 268–271 vol.3, July 2001.

[117] D. Jackson, P. Burghignoli, G. Lovat, F. Capolino, J. Chen, D. Wilton, and A. Oliner, "The fundamental physics of directive beaming at microwave and optical frequencies and the role of leaky waves," *Proceedings of the IEEE*, vol. 99, pp. 1780–1805, Oct 2011.

[118] A. Neto, N. Llombart, G. Gerini, D. Bonnedal, and P. de Maagt, "EBG Enhanced Feeds for the Improvement of the Aperture Efficiency of Reflector Antennas," *IEEE Transactions on Antennas and Propagation*, vol. 55, pp. 2185–2193, Aug 2007.

[119] O. Luukkonen, C. Simovski, G. Granet, G. Goussetis, D. Lioubtchenko, A. Raisanen, and S. Tretyakov, "Simple and Accurate Analytical Model of Planar Grids and High-Impedance Surfaces Comprising Metal Strips or Patches," *IEEE Transactions on Antennas and Propagation*, vol. 56, pp. 1624–1632, Jun 2008.

[120] N. Marcuvitz, "Waveguide Handbook," *Volume 10 in the Massachusetts Institute of Technology Radiation Laboratory series*, 1965.

[121] A. Neto, M. Ettorre, G. Gerini, and P. de Maagt, "Leaky Wave Enhanced Feeds for Multibeam Reflectors to be Used for Telecom Satellite Based Links," *IEEE Transactions on Antennas and Propagation*, vol. 60, pp. 110–120, Jan 2012.

[122] A. Polemi and S. Maci, “On the Polarization Properties of a Dielectric Leaky Wave Antenna,” *IEEE Antennas and Wireless Propagation Letters*, vol. 5, pp. 306–310, Dec 2006.

[123] K. Jeon, K. Lee, J. Son, L. T., J. Lee, and W. Lee, “X-band Isoflux Pattern Antenna for SAR Data Transmission,” in *3rd International Asia-Pacific Conference on Synthetic Aperture Radar APSAR*, pp. 1–4, 2011.

[124] R. Ravanelli, C. Iannicelli, N. Baldecchi, and F. Franchini, “Multi-Objective Optimization of an Isoflux Antenna for LEO Satellite Down-Handling Link,” in *18th International Conference on Microwave Radar and Wireless Communications (MIKON)*, pp. 1–4, 2010.

[125] G. Minatti, S. Maci, P. De Vita, A. Freni, and M. Sabbadini, “A Circularly-Polarized Isoflux Antenna Based on Anisotropic Metasurface,” *IEEE Transactions on Antennas and Propagation*, vol. 60, no. 11, pp. 4998–5009, 2012.

[126] S. Tretyakov, “Analytical Modeling in Applied Electromagnetics,” *Norwood, MA: Artech House*, 2003.

List of Related Publications

Journals Contributions

J5 *Directivity Enhancement and Spurious Mode Suppression in Leaky-Wave Antennas using Inductive Metasurfaces*, Darwin Blanco, Nuria Llombart, Eva Rajo Iglesias, Stefano Maci. IEEE Transactions on Antennas and Propagation, (accepted with Minor Revision), Jul 2014.

J4 *Radially Polarized Annular-Slot Leaky-Wave Antenna for Three-Dimensional Near-Field Microwave Focusing*, Darwin Blanco, Jose Luis Gomez-Tornero, Eva Rajo-Iglesias, Nuria Llombart. IEEE Antennas and Wireless Propagation Letters, vol.13, pp.583-586, 2014.

J3 *On the Use of Leaky Wave Phased Arrays for the Reduction of the Grating Lobe Level*, Darwin Blanco, Jose Luis Gomez-Tornero, Nuria Llombart, Eva Rajo-Iglesias. IEEE Transactions on Antennas and Propagation, vol.62, no.4, pp.1789-1795, Apr 2014.

J2 *Holographic Surface Leaky-Wave Lenses with Circularly-Polarized Focused Near-Fields PartI: Concept, Design and Analysis Theory*, Jose Luis Gomez-Tornero, Darwin Blanco, Nuria Llombart, Eva Rajo-Iglesias. IEEE Transactions on Antennas and Propagation, vol.61, no.7, pp.3475-3485, Jul 2013.

J1 *Holographic Surface Leaky-Wave Lenses with Circularly-Polarized Focused Near-Fields.Part II: Experiments and Description of Frequency Steering of Focal Length*, Darwin Blanco, Jose Luis Gomez-Tornero, Nuria Llombart, Eva Rajo-Iglesias. IEEE Transactions on Antennas and Propagation, vol.61, no.7, pp.3486-3494, Jul 2013.

Congress Contributions

- C8 *Evaluation of the Performance of Wearable Directive Antennas Based on Fabry-Perot Type* Aitor Vico-Martinez, Darwin Blanco, Eva Rajo-Iglesias, URSI AP-S International Symposium on Antennas; Memphis, USA. Jul 6-11, 2014.
- C7 *Gain Enhancement in Large Periodicity Arrays Based on Fabry-Perot Leaky Wave Antennas*, Darwin Blanco, Nuria Llombart, Eva Rajo-Iglesias, XXVIII Simposium Nacional de la Union Cientifica Internacional de Radio. Santiago de Compostela, Spain. Sep 2013. (Young Investigator Award Finalist).
- C6 *Thinned Printed Technology Phased Array Enhanced with Frequency Selective Surfaces for Space Applications*, Nuria Llombart, Darwin Blanco, Eva Rajo-Iglesias, Antonio Montesano-Benito, Jennifer Campuzano, URSI AP-S International Symposium on Antennas; Orlando, USA. Jul 7-13, 2013.
- C5 *Phased Array Integrated with Frequency Selective Surfaces for Angular Filtering*, Darwin Blanco, Nuria LLombart-Juan, Eva Rajo Iglesias, Stefano Maci; 7th European Conference on Antennas and Propagation; Gothenburg. Apr 8-12, 2013.
- C4 *Near-Field Focusing with Holographic Two-Dimensional Tapered Leaky-Wave Antennas*, Darwin Blanco, Nuria Llombart, Jose Luis Gomez-Tornero, Eva Rajo-Iglesias, XXVII Simposium Nacional de la Union Cientifica Internacional de Radio. Elche, Spain. Sep 12-14, 2012.
- C3 *Near and Far-Field Focusing with Holographic Two-Dimensional Tapered Leaky-Wave Spiral Antennas*, Darwin Blanco, Nuria LLombart-Juan, Eva Rajo Iglesias, Jose Luis Gomez-Tornero; URSI AP-S International Simposium on Antennas; Chicago, USA. Jul 6-14, 2012.
- C2 *Leaky Wave Enhanced Phased Array for the Reduction of the Grating Lobe Level*, Nuria LLombart-Juan, Darwin Blanco, Eva Rajo Iglesias.; URSI AP-S International Simposium on Antennas; Chicago, USA. Jul 6-14, 2012.
- C1 *Near-Field Focusing with Holographic Two-Dimensional Tapered Leaky-Wave Slot Antennas*, Jose Luis Gomez-tornero, Alejandro J. Martinez-Ros, Nuria LLombart-Juan, Darwin Blanco, Eva Rajo Iglesias. 6th European Conference on Antennas and Propagation; Prague. Mar 26-30, 2012.

Resumen

El objetivo principal de esa tesis es presentar soluciones innovadoras para realizar conformación de haz con antenas tipo *Leaky Wave*. Estas antenas son conocidas por ser de bajo coste, fáciles de diseñar y tener alta ganancia. Los campos de aplicación de este tipo de antenas son muy variados y pueden ir desde aplicaciones en campo cercano (antenas holográficas) hasta campo lejano (aplicaciones para satélites de bajas y altas órbitas). En particular para antenas en campo cercano, esta tesis propone el uso de antenas *Leaky Wave* periódicas para sintetizar diagramas de radiación que focalizan el campo concentrándolo en un punto con una polarización predeterminada. Se investiga el impacto de los distintos tipos de polarización (circular y lineal) en la forma de la región focal, así como la habilidad de este tipo de antenas para desplazar el foco en función de la frecuencia. Ambos fenómenos se estudian a través de varios diseños y con las medidas de dos prototipos construidos. En campo lejano se consideran dos escenarios. En el primero se presenta un estudio para satélites geoestacionarios donde agrupaciones de antenas con grandes periodicidades son útiles para cubrir unos pocos grados. Por el contrario, el segundo escenario se centra en una aplicación de satélite para baja órbita. Aquí es recomendable utilizar una agrupación de antenas con periodicidad menor que λ para poder cubrir grandes ángulos. En estos dos escenarios las antenas *Leaky Wave* uniformes son muy adecuadas ya que permiten que las áreas de los diferentes elementos de la agrupación de antenas se solapen. Todos estos diseños se verifican con software comercial y código propio así como a través de medidas de los prototipos fabricados.

Declaration

I hereby declare that the contents of this PhD dissertation are original and have not been submitted in whole or in part for consideration for any other degree of any other University. This dissertation is the result of my own work, except where specific reference is made to the work of others. This dissertation contains approximately 43,500 words including captions, footnotes, tables, equations, appendices and bibliography, and has 115 figures.

Darwin Blanco
Madrid, 2014

Acknowledgements

En la vida muchos sucesos llamados circunstanciales nos suponen una controversia para hoy estar aquí. Son muchas las personas que indudablemente me han brindado su ayuda para poder culminar este ciclo. Gracias a todos ellos.

Particularmente quiero agradecer primero a la divina providencia por la fortuna de conocer a mis dos tutoras, Eva Rajo Iglesias y Nuria Llombart Juan. Más allá de todos los conocimientos que me han transmitido, me queda un profundo respeto y admiración por el trabajo que hacen. También quiero expresar mi gratitud a Jennifer Campuzano y Antonio Montesano Benito de EADS/CASA por participar en el proyecto del cual se derivaron gran parte de los resultados de esta investigación.

Quiero dar las gracias a mi hermana por su inconmensurable apoyo y a mi padre por el tiempo que les tomé prestados para cumplir este sueño. Con especial cariño, quiero dar gracias a la Familia Román Sandoval, Chris, Maribel, Isis y Juan, por brindarme la calidez de su hogar durante la mayor parte de mi tiempo en España. Por ultimo son tantas personas que han contribuido indirecta o directamente con su apoyo, consejos y ayuda a las que debo mi agradecimiento: Beatriz Helena Vinasco, Sandra Valencia, Zoeny Alvares, Rebeca Gutierrez, Patricia Sevilla, Anna McKechnie, Raphaela Markwirth, Ricardo Fernando Alvear, Jessica Moysen, Sara del Cerro y Megan Davies.

Madrid 2014